Aus der Klinik und Poliklinik für Nuklearmedizin
Klinik der Ludwig-Maximilians-Universität München
Vorstand: Prof. Dr. med. Rudolf A. Werner

Development of antibody-based PET-Radiotracers for detection of Neurodegenerative Pathologies

Dissertation
zum Erwerb des Doktorgrades der Naturwissenschaften
an der Medizinischen Fakultät der
Ludwig-Maximilians-Universität München

vorgelegt von
Monireh Shojaei
aus
Esfahan, Iran

Jahr
2025

Mit Genehmigung der Medizinischen Fakultät
der Ludwig-Maximilians-Universität München

Betreuer:	PD Dr. Simon Lindner
Zweitgutachter:	Prof. Dr. Dominik Paquet
Dekan:	Prof. Dr. med. Thomas Gudermann
Tag der mündlichen Prüfung:	10. Dezember 2025

Affidavit

Eidesstattliche Versicherung

Shojaei, Monireh

Name, Vorname

Ich erkläre hiermit an Eides statt, dass ich die vorliegende Dissertation mit dem Titel:

Development of antibody-based PET-Radiotracers for detection of Neurodegenerative Pathologies

selbständig verfasst, mich außer der angegebenen keiner weiteren Hilfsmittel bedient und alle Erkenntnisse, die aus dem Schrifttum ganz oder annähernd übernommen sind, als solche kenntlich gemacht und nach ihrer Herkunft unter Bezeichnung der Fundstelle einzeln nachgewiesen habe.

Ich erkläre des Weiteren, dass die hier vorgelegte Dissertation nicht in gleicher oder in ähnlicher Form bei einer anderen Stelle zur Erlangung eines akademischen Grades eingereicht wurde.

München, 17.12.2025 Monireh Shojaei

Ort, Datum Unterschrift

Confirmation of Congruency

Erklärung zur Übereinstimmung der gebundenen Ausgabe der Dissertation mit der elektronischen Fassung

Shojaei, Monireh

Name, Vorname

Hiermit erkläre ich, dass die elektronische Version der eingereichten Dissertation mit dem Titel:

Development of antibody-based PET-Radiotracers for detection of Neurodegenerative Pathologies

in Inhalt und Formatierung mit den gedruckten und gebundenen Exemplaren übereinstimmt.

München, 17.12.2025 Monireh Shojaei

Ort, Datum Unterschrift

Inhaltsverzeichnis

List of Abbreviations

Aβ	Amyloid-β
AD	Alzheimer's disease
ALS	Amyotrophic lateral sclerosis
APP	Amyloid precursor protein
A_s	Specific activity [MBq/µg]
BBB	Blood brain barrier
BFC	Bifunctional chelator
CT	Computed tomorgraphy
CNS	Central nervous system
DPR	Dipeptide repeat proteins
DAM	Disease-associated microglia
DOTA	1,4,7,10-tetraazacyclododecane-1,4,7,10-tetraacetic acid
ELISA	Enzyme-linked immunosorbent assay
FTD	Frontotemporal dementia
hTfR	Human transferrin receptor
mAb	Monoclonal antibody
NDD	Neurodegenerative diseases
PET	Positron emission tomography
PSEN1	Presenilin 1
%ID/g	Percentage injected dose per gram tissue
p.i.	Post injection
p-NCS-benzyl-NODA-GA	2,2′-(7-(1-carboxy-4-((4-isothiocyanatobenzyl)amino)-4-oxo-butyl)-1,4,7-triazonane-1,4-diyl)diacetic acid
RMT	Receptor-mediated transcytosis
RT	Room temperature
RCY	Radiochemical yield
SUV	Standard uptake value
SUVR	Standard uptake value ratio
SPM	Statistical parametric mapping
sTREM2	Soluble triggering receptor expressed on myeloid cells 2

TREM2	Triggering receptor expressed on myeloid cells 2
Tg	Transgenic
TETA	1,4,8,11-tetraazacyclotetradecane-1,4,8,11-tetraacetic acid
VOI	Volume of interest
WT	Wild-type

Declaration on AI-Assisted Figure Generation

Most of the figures presented in this dissertation were created using a multi-step, AI-assisted graphical workflow. Individual graphical elements were obtained from various sources, including ChatGPT (2024-2025), as well as standard scientific and graphical software such as ChemDraw and Microsoft PowerPoint.

All graphical components were independently selected, manually edited, recoloured, repositioned, and combined by the author. Additional graphical decisions, including layout, transparency, and compositional adjustments, were made during the figure creation process. The final figures, therefore, represent original, independent graphical work produced by the author.

Where applicable, conceptual ideas were derived from the scientific literature and are cited accordingly. All scientific interpretations and conclusions presented in this dissertation were developed by the author.

Publikationsliste

Shojaei M, Zhou Q, Palumbo G, Schaefer R, Kaskinoro J, Vehmaan-Kreula P, et al. Development and Preclinical Evaluation of a Copper-64-Labeled Antibody Targeting Glycine-Alanine Dipeptides for PET Imaging of C9orf72-Associated Amyotrophic Lateral Sclerosis/Frontotemporal Dementia. ACS Pharmacol. Transl. Sci. 2024; 7: 1404-14**.**
https://pubs.acs.org/doi/full/10.1021/acsptsci.4c00037

Shojaei M, Schaefer R, Schlepckow K, Kunze LH, Struebing FL, Brunner B, Willem M, Bartos LM, Feiten A, Palumbo G, Arzberger T, Bartenstein P, Parico GC, Xia D, Monroe KM, Haass C, Brendel M, Lindner S. PET imaging of microglia in Alzheimer's disease using copper-64 labeled TREM2 antibodies. Theranostics 2024; 14(16):6319-6336. doi:10.7150/thno.97149. https://www.thno.org/v14p6319.htm

Conference abstracts

Shojaei M, Haass C, Edbauer D, Schlepckow K, Bartenstein P, Brendel M, et al. SP-006 - Development of silicon fluoride acceptor (SiFA)-conjugated antibodies targeting TREM2 and Poly-GA repeats as new tracers for PET imaging of neurodegenerative diseases. Nucl Med Biol. 2021; 96-97: S37.
https://doi.org/10.1016/S0969-8051(21)00323-1
eSRS 2021, Virtual Meeting

Shojaei M, Schlepckow K, Brunner B, Monroe KM, Haass C, Bartenstein P, et al. P-099 - Development of novel ^{64}Cu-labelled antibodies for PET-CT imaging of TREM2. Nucl Med Biol. 2022; 108-109: S104
https://doi.org/10.1016/S0969-8051(22)00236-0
iSRS 2022, Nantes, France

Beitrag zu den Veröffentlichungen

1.1 Beitrag zu Paper I

Development and preclinical evaluation of copper-64 labeled antibody targeting glycine-alanine dipeptides for PET imaging of C9orf72 associated amyotrophic lateral sclerosis/ frontotemporal dementia

1.1.1 Contributions Summary

- Method development including the modification and labeling of antibodies, conducting experiments, data analysis, and statistical analysis
- The initial draft of the paper was written by Monireh Shojaei

1.1.2 Detailed Contributions

Section	Responsibility & Contribution	Text
Method Development and Establishment for Antibody Modification and Labeling Methods	[^{64}Cu]Cu-NODAGA-mAb1A12	-
Quality Control	HPLC (UV and Radio), Radio-TLC, *in vitro* stability, SDS-Page, *Ex vivo* radio TLC	Figure 1B, 1C, 1D, 1E, Figure S2A, S2B, S2C, S2D Figure 4D, 4E
***In vitro* experiment**	*In vitro* autoradiography on the brain section of GA$^{\pm}$ Camk2a$^{\pm}$, WT Specificity (Blocking) experiment	Figure 2E, 2F, 2G, 2H
PET/CT	PET/CT imaging (Animal handling/experiment) of two mouse groups (n=24), including GA$^{\pm}$ Camk2a$^{\pm}$ and WT at 2h, 20h, and 40h p.i.	Figure 3A, 3B, 3C, 3D Figure S4
Biodistribution, **Statistical analysis**	Biodistribution (Animal handling/experiment) of two mouse groups (n=24), including GA$^{\pm}$ Camk2a$^{\pm}$ and WT at 2h, 20h, and 40h p.i., along with related data and statistical analysis.	Figure 4A, 4B, 4C Table S2
***Ex vivo* autoradiography,** **Statistical analysis**	*Ex vivo* autoradiography experiment of GA$^{\pm}$ Camk2a$^{\pm}$ and WT, along with related data analysis.	Figure 4F, 4G, 4H

Manuscript writing	Initial draft	-

1.2 Beitrag zu Paper II

PET imaging of microglia in Alzheimer's disease using copper-64 labeled TREM2 antibodies

1.2.1 Contributions Summary

- The project was initiated by Monireh Shojaei
- Method development including the modification and labeling of antibodies, conducting experiments, data analysis, and statistical analysis
- The initial draft of the paper was written by Monireh Shojaei

Rationale for the Division of First Authorship:

- The merger of two projects within a thematic complex, and the temporal offset of both doctoral theses

1.2.2 Detailed Contributions

Section	Responsibility & Contribution	Text
Development and Establishment of Methods for Antibody Modification and Labeling	[^{64}Cu]Cu-NODAGA-ATV:4D9, [^{64}Cu]Cu-NODAGA-4D9, [^{64}Cu]Cu NODAGA-14D3	Table 1 (Cohort 1A, 1B, 2A, 2B) Table 2
Quality Control	HPLC (UV and Radio), Radio-TLC, *in vitro* stability	Figure S2A, S2B, S2C, S2D, S2E, S3A
***In vitro* Autoradiography**	*In vitro* autoradiography on the brain section of 5xFAD;TfR$^{mu/hu}$, WT;TfR$^{mu/hu}$ Specificity (Blocking) experiment	Figure 1A, 1B
Biodistribution, **Statistical analysis**	Biodistribution (Animal handling/experiment) of 4 mouse groups (n=72) including 5xFAD;TfR$^{mu/hu}$, WT;TfR$^{mu/hu}$, 5xFAD, WT at 2h, 20h and 40h p.i., along with related data and statistical analysis.	Figure 2A, 2B, 2C, Figure S5 Table S1, S2

PET/CT, **Statistical analysis**	PET/CT imaging (Animal handling/experiment) of 4 mouse groups (n=72) including 5xFAD;TfR$^{mu/hu}$, WT;TfR$^{mu/hu}$, 5xFAD, WT at 2h, 20h and 40h p.i., along with related data and statistical analysis.	Figure 3A, 3B, 3C, 3D Figure S6 Table S3, S4, S5
SPM, **Statistical analysis**	PET-to-biodistribution correlation, SPM image generation Data analysis	Figure 4A, 4B, 4C Table S8, S9
***Ex vivo* autoradiography,** **Statistical analysis**	*Ex vivo* autoradiography experiment of 4 mouse groups including 5xFAD;TfR$^{mu/hu}$, WT;TfR$^{mu/hu}$, 5xFAD, WT at 2h, 20h, and 40h p.i., along with related data and statistical analysis.	Figure 5A, 5B, 5C
Human anti-TREM2 autoradiography	Autoradiography on the brain section of AD patient	Figure S12C
Manuscript writing	Initial draft	-

2. Summary

Purpose:

Neuroinflammation is a central process in response to brain injuries. As a complex process, neuroinflammation is challenging to assess comprehensively *in vivo*, making its exact role in neurodegenerative diseases (NDDs) unclear. However, some aspects of neuroinflammation such as microglia activation can be assessed *in vivo* using imaging techniques like Positron Emission Tomography (PET). PET imaging of activated microglia serves as a biomarker for neuroinflammation, providing valuable information about this process in living subjects that aids in detecting and diagnosing NDDs at an early stage. PET is a non-invasive imaging technique well-suited for this purpose due to its high sensitivity and spatial resolution. Microglial activation and function are strongly associated with an immune receptor called Triggering Receptor Expressed on Myeloid Cell 2 (TREM2). **In the first part of this study, I developed three PET-radiotracers that bind specifically to mouse and human TREM2. I did investigations to evaluate the tracer *in vitro* and *in vivo.*** TREM2 PET imaging allows observation of how microglial cells behave during disease progression. The physiology and mechanisms of activated microglia can be monitored and measured *in vivo,* which provides valuable data associated with neuroinflammation in various NDDs.

The second part of this study is focused on developing a radioligand that specifically binds to the poly(glycine-alanine) (poly-GA) protein. A comprehensive preclinical evaluation of the tracer was conducted both *in vitro* and *in vivo*. Poly-GA protein results from the unconventional translation of the $(G_4C_2)_n$ repeat expansion in the C9orf72 gene. Poly-GA protein is associated with Amyotrophic Lateral Sclerosis (ALS) and Frontotemporal Dementia (FTD), accumulating in the neuronal cytoplasmic inclusions of FTD/ALS patients. Poly-GA is toxic and can be transmitted between cells, spreading its toxicity to other cells. The development of a tracer that specifically binds to Poly-GA could potentially facilitate the *in vivo* monitoring of Poly-GA protein's accumulation and distribution. This, in turn, may enable the tracking of disease progression in FTD/ALS patients with C9orf72 mutations, offering a new tool for research assessment.

Methods:

Radiotracer development for both TREM2 and Poly-GA targets relies primarily on monoclonal antibodies (mAb), due to their high specificity and affinity. For TREM2, the 4D9 antibody and its variant with an engineered transport vehicle, ATV:4D9, were used. The antibody transport vehicle (ATV) binds to the human transferrin receptor (hTfR) and overcomes the transcytosis limitation of the antibody-based radiotracer across the blood-brain barrier (BBB). The mAb1A12 antibody

was used to develop the poly-GA tracer. **To enable delivery of the radionuclide to the TREM2 and Poly-GA targets, I modified each antibody by conjugating it with the chelator *p*-NCS-benzyl-NODAGA.** The affinity of the modified Poly-GA antibody and the potency of the modified TREM2 antibody were assessed. **Each antibody was radiolabeled with copper-64 using optimized conditions to achieve high radiochemical purity (RCP) and specific activity (A_s) while maintaining the antibody's structural integrity and binding affinity.** The stability of each tracer was investigated *in vitro* (using HPLC) and *ex vivo* (using SDS-PAGE and radio-TLC of gel). *In vitro* autoradiography was conducted on the brain sections of transgenic mice to evaluate the tracer's binding and to predict their suitability for subsequent *in vivo* experiments. **Following the *in vitro* characterization of receptor distribution and density in brain tissues, I conducted *in vivo* evaluation of the tracer using PET imaging.** To find the optimal tracer uptake and high image quality, the scans were done at 2 h, 20 h, and 40 h post-injection (p.i.). In addition to PET, biodistribution was used to characterize tracer enrichment in the brain and other organs. For the *in vivo* characterization of TREM2 tracers, the 5xFAD mouse model was used. This mouse model is genetically engineered to express mutations associated with Alzheimer's disease (AD). In this AD mouse model, amyloid pathology leads to a significant beta-amyloid (Aβ) plaque accumulation in cortical and hippocampal brain regions, associated with microglial activation. Wild-type mice (WT) were used as a negative control. To test the potential of ATV antibody to enhance brain uptake over the BBB, an amyloidogenesis mouse model expressing the genetically engineered hTfR alongside its native murine transferrin receptor (muTfR) (5xFAD; $TfR^{mu/hu}$) was used. Wild-type mice (WT; $TfR^{mu/hu}$) were also included for comparison.

For translating to human imaging, the 14D3 antibody, which specifically binds to human TREM2, was used. The 14D3 antibody, which specifically binds to human TREM2, was conjugated with *p*-NCS-NODAGA chelator and subsequently radiolabeled with copper-64 under optimized conditions. The resulting **[^{64}Cu]Cu-NODAGA-14D3 radiotracer** was then utilized for *in vitro* autoradiography studies on human brain tissue sections to evaluate its binding characteristics and distribution in Alzheimer's disease pathology.

For Poly-GA imaging, I used transgenic mice (Tg) that express GFP-(GA)175 specifically in excitatory neurons under the control of the Camk2a-Cre driver. This mouse model mimics aspects of Poly-GA pathology associated with FTD/ALS diseases. As a control group, I used wild-type (WT) mice that do not express the Poly-GA protein.

Results:

Antibody modification did not impact TREM2 and Poly-GA binding. **The ^{64}Cu-labeled antibodies were obtained with high RCP, radiochemical yield (RCY), and A_s. The binding of ATV:4D9 to TREM2 and mAb1A12 to Poly-GA targets was demonstrated to be specific. The stability of each tracer (copper-chelator complex) was verified *in vitro* and *ex vivo*.**
TREM2-PET imaging revealed higher tracer uptake in the cortex and hippocampus of 5xFAD mice compared to WT. In addition, the brain uptake in mice expressing hTfR was higher than in those lacking hTfR. This result is due to active tracer-based antibody transport via hTfR over the BBB. Imaging at three different time points revealed 20 h p.i. as a robust imaging time point. The findings from PET imaging were further supported by *ex vivo* autoradiography analysis. Elevated TREM2 tracer binding in the cortex of AD patients was demonstrated using human *in vitro* autoradiography.

My initial evaluation of the [^{64}Cu]Cu-NODAGA-mAb1A12, using *in vitro* autoradiography on brain slices from Tg mice, revealed a higher tracer uptake in the neocortex and hippocampus compared to the WT. This result aligns with the highest Poly-GA expression in these brain regions, as measured by an immunoassay experiment. Poly-GA PET scans at three-time points revealed the highest tracer uptake in the cortex of transgenic mice, aligning with the *in vitro* experiment. Furthermore, the most significant difference in tracer uptake between transgenic and WT mice was revealed at 20 h p.i., establishing it as a suitable time point for imaging. Biodistribution studies showed a higher uptake at 20 h p.i. in the brains of Tg mice.

Conclusion:
In this study, several tracers were developed targeting TREM2 and Poly-GA. These novel tracers represent significant advancements in molecular imaging for neurodegenerative diseases, potentially facilitating earlier diagnosis and providing new tools for evaluating therapeutic interventions.
The [^{64}Cu]Cu-NODAGA-ATV:4D9 tracer revealed the potential to image TREM2 for the first time *in vivo*. The ATV engineering for hTfR binding and transcytosis overcomes the BBB restriction for antibody-based PET radiotracers. **Future studies should focus on optimizing these tracers for clinical translation and exploring their applications in a broader range of neurological conditions.**
The [^{64}Cu]Cu-NODAGA-mAb1A12 is introduced as the first developed Poly-GA tracer. It proved to be a favorable tracer for preclinical imaging of C9orf72 ALS/FTD diseases in mouse models. **While this study focuses on antibody-based approaches due to their well-established high**

specificity and affinity, future research could explore these alternative targeting strategies to potentially overcome the limitations of BBB penetration.

3. Zusammenfassung

Zweck:

Neuroinflammation ist ein zentraler Prozess im Gehirn und ein pathologisches Merkmal vieler neurodegenerativer Erkrankungen. Dieser komplexe Prozess kann jedoch nicht umfassend *in vivo* dargestellt werden, sodass seine genaue Rolle unklar bleibt. Mikrogliazellen sind die primären Immunzellen im zentralen Nervensystem. Sie sind die Haupttreiber der Neuroinflammation. In einem gesunden Gehirn befinden sich Mikroglia in einem homöostatischen Zustand. Bei neurodegenerativen Vorgängen, wie der Ablagerung von Amyloid-Plaques, wechseln sie in einen aktivierten Zustand. Die Funktion der Mikroglia ist stark mit einem Immunrezeptor namens Triggering Receptor Expressed on Myeloid Cells 2 (TREM2) verbunden. Der Verlust der TREM2-Funktion beeinflusst direkt die Aktivität der Mikroglia. Die Quantifizierung dysregulierter Mikrogliazellen im Frühstadium ist entscheidend für das Verständnis der Neuroinflammation, was bei der Erkennung und Diagnose von neurodegenerativen Erkrankungen eine wichtige Rolle spielt. Aktivierte Mikroglia können *in vivo* mittels Positronen-Emissions-Tomographie (PET) untersucht werden. PET ist eine nicht-invasive Bildgebungstechnik, die sich aufgrund ihrer hohen Empfindlichkeit und räumlichen Auflösung für diesen Zweck eignet. Im ersten Teil dieser Studie wurde ein PET-Radiotracer entwickelt, der spezifisch an TREM2 bindet. Mit Kleintier-PET können Physiologie und Veränderungen von Mikrogliazellen während des Krankheitsverlaufs *in vivo* überwacht und evaluiert werden.

Der zweite Teil dieser Studie konzentriert sich auf die Entwicklung eines Radioliganden, der spezifisch an das Poly-(Glycin-Alanin)-Protein (Poly-GA) bindet. Poly-GA-Protein entsteht durch die unkonventionelle Translation der $(G_4C_2)_n$ Repeat-Erweiterung im C9orf72-Gen. Poly-GA-Protein ist mit Amyotropher Lateralsklerose und Frontotemporaler Demenz (FTD/ALS) assoziiert und reichert sich in den neuronalen zytoplasmatischen Einschlüssen von FTD/ALS-Patienten an. Poly-GA ist toxisch und kann zwischen Zellen übertragen werden, wodurch es seine Toxizität auf andere Zellen überträgt. Die Entwicklung eines Tracers, der spezifisch an Poly-GA bindet, könnte verwendet werden, um Poly-GA *in vivo* zu detektieren und somit die Verfolgung des Krankheitsverlaufs bei FTD/ALS-Patienten zu ermöglichen.

Methoden:

Die Entwicklung von Radiotracern für sowohl TREM2 als auch Poly-GA basiert hauptsächlich auf monoklonalen Antikörpern (mAb), da diese eine hohe Spezifität und Affinität aufweisen. Für TREM2 wurde der 4D9-Antikörper und seine Variante mit einem Transportvehikel, ATV:4D9,

verwendet. Das Antikörper-Transportvehikel (ATV) bindet an den humanen Transferrin-Rezeptor (hTfR) und überwindet die Blut-Hirn-Schranke (BBB) mittels rezeptor-vermittelter Transzytose. Der mAb1A12-Antikörper wurde zur Entwicklung des Poly-GA-Tracers verwendet. Um Radionuklide an die TREM2- und Poly-GA-Targets zu transportieren, wurde jeder Antikörper kovalent mit einem Chelator, *p*-NCS-benzyl-NODAGA, modifiziert. Die Affinität des modifizierten Poly-GA-Antikörpers und die Funktionalität des modifizierten TREM2-Antikörpers wurden bestätigt. Die Antikörper wurden mit Kupfer-64 markiert. Die Stabilität jedes Tracers wurde sowohl *in vitro* als auch *ex vivo* untersucht. *In-vitro*-Autoradiographie wurde an Hirnschnitten von transgenen Mäusen durchgeführt, um die Bindung und Spezifität der entwickelten ^{64}Cu-markierten Antikörper zu bewerten und ihre Eignung für nachfolgende *in-vivo*-Experimente vorherzusagen. Die Tracer wurden *in vivo* mittels PET-Bildgebung evaluiert.. Um den Zeitpunkt der optimalen Traceraufnahme zu finden, wurde der Scan 2 h, 20 h und 40 h p.i. durchgeführt. Zusätzlich zur PET wurden Biodistributionsexperimente durchgeführt, um die Anreicherung des Tracers im Gehirn und in anderen Organen zu charakterisieren. Für die *in vivo* Charakterisierung der TREM2-Tracer wurde das 5xFAD-Mausmodell, ein Modell der Alzheimer-Krankheit, verwendet. Wildtyp-Mäuse wurden als Negativkontrolle verwendet. Um das Potenzial des ATV-Antikörpers zur Verbesserung der Gehirnaufnahme über die BBB zu testen, wurde ein 5xFAD-Mausmodell verwendet, das den hTfR (5xFAD; TfR$^{mu/hu}$) exprimiert. Entsprechende Wildtyp-Mäuse (WT; TfR$^{mu/hu}$) wurden ebenfalls zum Vergleich einbezogen. Um die Translation zu einer klinischen Anwendung zu adressieren, wurde der 14D3-Antikörper verwendet, der spezifisch an humanes TREM2 bindet. Der 14D3-Antikörper wurde modifiziert und mit Kupfer-64 markiert. Die 14D3-Tracer wurde für die *in-vitro*-Autoradiographie an humanen Hirngewebeschnitten verwendet.

Für die Poly-GA-Bildgebung wurden transgene Mäuse (Tg) verwendet, die GFP-(GA)175 in exzitatorischen Neuronen exprimieren, gesteuert durch Camk2a-Cre. Dieses Mausmodell stellt die typische Poly-GA-Pathologie dar, die mit FTD/ALS-Erkrankungen einhergehen. Als Kontrollgruppe diente ein Wildtyp-Mausmodell, das Poly-GA nicht exprimierte.

Ergebnisse:

Die chemische Modifikation der Antikörper hatte keinen nachteiligen Einfluss auf die Bindung an ihre jeweiligen Targets, TREM2 und Poly-GA. Die Markierung der Antikörper mit Kupfer-64 wurde mit hoher radiochemischer Reinheit, radiochemischer Ausbeute und spezifischer Aktivität erreicht. Die Antikörper ATV:4D9 und mAb1A12 binden spezifisch an TREM2 bzw. Poly-GA. Dies wurde durch ein Blockierungsexperiment mit einem 1000-fachen Überschuss an nicht-radioaktivem Antikörper bestätigt. Die Stabilität jedes Tracers (Kupfer-Chelator-Komplex) wurde *in*

vitro und *ex vivo* bestätigt. Die Anreicherung der Tracer im Gehirn der Mäuse wurde mittels PET-Bildgebung *in vivo* charakterisiert. Eine höhere Traceraufnahme wurde im Kortex und Hippocampus von 5xFAD-Mäusen im Vergleich zu Wildtyp-Mäusen beobachtet. TREM2-PET zeigte, dass die Gehirnaufnahme bei Mäusen, die hTfR exprimieren, höher war als bei denen, die keinen hTfR exprimieren. Dieses Ergebnis ist auf den aktiven Antikörpertransport durch hTfR über die Blut-Hirn-Schranke zurückzuführen. Die Bildgebung zu drei verschiedenen Zeitpunkten zeigte, dass 20 h p.i. ein robuster Bildgebungszeitpunkt ist. Mikroglia-reiche Regionen im Kortex und Hippocampus erklären die erhöhte Radiotraceraufnahme in den Gehirnen von 5xFAD; $TfR^{mu/hu}$-Mäusen, was durch eine voxel-weise Korrelation zwischen der Hirnanreicherung aus Biodistribution und TREM2 PET gezeigt wurde. Die *ex-vivo*-Autoradiographieergebnisse bestätigten die PET-Ergebnisse. Eine erhöhte kortikale TREM2-Tracerbindung auf Gewebeschnitten von Alzheimer-Patienten wurde durch humane *in-vitro*-Autoradiographie nachgewiesen.

Die erste Bewertung des [^{64}Cu]Cu-NODAGA-mAb1A12 mittels *in-vitro*-Autoradiographie an Gehirnschnitten von transgenen Mäusen zeigte eine höhere Traceraufnahme im Neokortex und Hippocampus im Vergleich zu Wildtyp-Mäusen. Dieses Ergebnis stimmt mit der höchsten Poly-GA-Expression in diesen Gehirnregionen überein, was durch einen Immunoassay bestätigt wurde. Poly-GA-PET-Scans zu drei Zeitpunkten zeigten die höchste Traceraufnahme im Kortex von transgenen Mäusen, was mit dem *in-vitro*-Experiment übereinstimmt. Darüber hinaus wurde der signifikanteste Unterschied in der Traceraufnahme zwischen transgenen und WT-Mäusen 20 h p.i. festgestellt, was diesen Zeitpunkt als geeigneten Bildgebungszeitpunkt bestätigt. Die Biodistributionsstudie zeigte eine höhere Traceraufnahme in den Gehirnen von transgenen Mäusen 20 Stunden nach Injektion. Da der Antikörper eine lange biologische Halbwertszeit hat, zirkuliert er lange im Blutkreislauf.

Schlussfolgerung:

In dieser Studie wurden Tracer entwickelt, die auf TREM2 und Poly-GA abzielen. Jeder Tracer wurde mittels nicht-invasiver PET-Bildgebung *in vivo* evaluiert. Der [^{64}Cu]Cu-NODAGA-ATV:4D9-Tracer zeigte das Potenzial, TREM2 *in vivo* zu visualisieren. Die ATV-Technologie erhöhte die Effizienz des Transports antikörperbasierter PET-Radiotracer über die Blut-Hirn-Schranke. TREM2-PET ermöglichte die Detektion und Quantifizierung aktivierter Mikrogliazellen *in vivo* unter Verwendung eines AD-Mausmodells. Dies könnte eine nützliche Methode zur Untersuchung der Neuroinflammation bei weiteren inflammatorischen Erkrankungen sein.

Im zweiten Teil dieser Studie wurde [^{64}Cu]Cu-NODAGA-mAb1A12 als erster Poly-GA-Tracer vorgestellt. Dieser erwies sich als ein geeigneter Tracer für die präklinische Bildgebung von

C9orf72 ALS/FTD-Erkrankungen in Mausmodellen. Trotz eingeschränkter Diffusion über die Blut-Hirn-Schranke wurden hochwertige PET-Bilder generiert. Ein mAb1A12-Antikörper, der sich die rezeptorvermittelte Transzytose zu Nutze macht, könnte jedoch die Gehirnaufnahme des Tracers über die Blut-Hirn-Schranke erheblich verbessern.

4. Introduction

4.1 Neurodegenerative Diseases

Neurodegenerative diseases are a group of disorders characterized by progressive dysfunction and loss of neurons in the central nervous system (CNS). [1] In NDD, nerve cells are lost in an irreversible process, causing cognitive and physical decline in patients. [2-4] While dementia primarily affects adults, it can occasionally impact younger populations and, rarely, even children. [5]

There were more than 55 million people with dementia worldwide in 2019. This statistic, reported by the World Health Organization (WHO), specifically refers to individuals aged 40 and older. There are almost 10 million new cases of dementia every year. [6] In 2021, nearly 1.8 million people in Germany lived with dementia aged 40 and above, and 1.7 million were in the age group of 65 and above. Predictions suggest that the number of affected individuals aged 65 and above could increase to 2.8 million by 2050. [7, 8] The German Center for Neurodegenerative Diseases (DZNE) estimated that the financial impact of dementia in Germany will roughly increase from 83 billion euros in 2020 to nearly 195 billion euros by 2060. [9]

Dementia is a broad term that encompasses various types of cognitive disorders. Alzheimer's disease is the most prevalent form of dementia, accounting for roughly two-thirds (50-60%) of all cases. [6, 10] Another form of dementia is FTD, which affects the behavior and language of patients. [8, 10] FTD occurs between the ages of 45 and 65 years old [11] and is closely related to ALS. [12, 13] ALS is another NDD that affects the motor neurons, causing muscular atrophy and paralysis in patients. [14] Protein accumulation in the CNS is critical in many NDDs. Notably, AD is characterized by intracellular amyloid β plaques and tau protein deposition. [15, 16]

Similarly, tau, TDP-43, and FUS proteins can also be seen in FTD and ALS [17-19] Furthermore, ALS/FTD patients with C9orf72 mutations show dipeptide repeat proteins (DPRs) in their CNS. [13] The protein accumulations can contribute to neuroinflammation, which may worsen neurodegeneration. [20] Lecanemab (recommended by EMA[21] for treatment and FDA-approved) and Aducanumab (FDA-approved) are therapeutic antibodies designed to target Aβ in Alzheimer's disease. [22, 23] Similarly, Riluzole, which gained approval in 1995 as an oral tablet, and edaravone, approved in 2017 as an intravenous infusion, are two medications for ALS that slow the progression of the disease. [24, 25] However, these treatments do not address the main causes of these diseases. Instead, they decelerate disease progression and extend the longevity of patients.

Neuroinflammation has two contradictory functions in the brain: defensive and protective. While the inflammatory responses can be protective against various pathogens, chronic inflammation can be harmful by preventing tissue repair, which leads to neuronal damage. Several factors such as genetic mutation and protein aggregation can cause sustained inflammation. [26, 27] The primary resident macrophages, microglia [28], and astrocytes [20, 29, 30] are the main causes of chronic inflammatory processes. Persistent inflammatory responses may eventually result in NDDs. [26] Therefore, understanding neuroinflammation is essential for detecting and diagnosing NDDs at an early stage.

4.2 Molecular Imaging using Positron Emission Tomography (PET)

PET is an imaging technique widely used as an effective diagnostic tool for various diseases, including NDDs. [31] PET is a commonly used imaging technique in modern nuclear medicine, and its applications span diverse regions of the body. It enables non-invasive measurement and monitoring of disease progression and quantification of biological processes with high sensitivity. [4, 31-33] At the clinical level, this technique is often paired with computed tomography (CT) (PET/CT), offering a comprehensive perspective on both morphological and functional data. [34-36] The process begins with the introduction of a radiotracer into the patient's bloodstream.

A radiotracer is a molecule labeled with radioactive isotopes (radionuclides), specifically designed for particular molecules within the body, referred to as targets. A receptor, protein accumulation, or transporter can serve as a target for specific diseases. Radiotracers have high affinity and specificity toward their intended targets. The distribution of radiotracers within the body is detected using highly sensitive scintillation detectors arranged in a ring configuration around the patient. These detectors capture the annihilation photons resulting from positron emission, enabling the reconstruction of three-dimensional images of radiotracer concentration. [32, 37] A proton in the nucleus transforms into a neutron, which leads to positron (β^+) emission. The positrons emitted from radionuclides annihilate with surrounding electrons in the targeted tissue, releasing two photons (γ) with a defined energy of 511 keV in opposite directions (Figure 1). The PET scanner captures these photon pairs. In parallel, a CT scan employs X-rays to create a detailed image of the body's anatomy. Later the software reconstructs the location of the annihilation event. The fusion of PET and CT images provides valuable *in vivo* information. [38, 39]

Several positron-emitting radionuclides are used for diagnostics, including ^{18}F ($t_{1/2}$ = 110 min), ^{11}C ($t_{1/2}$ = 20 min), ^{64}Cu ($t_{1/2}$ = 12.7 h), ^{68}Ga ($t_{1/2}$ = 67.6 min), and ^{15}O ($t_{1/2}$ = 2 min). [32, 37]

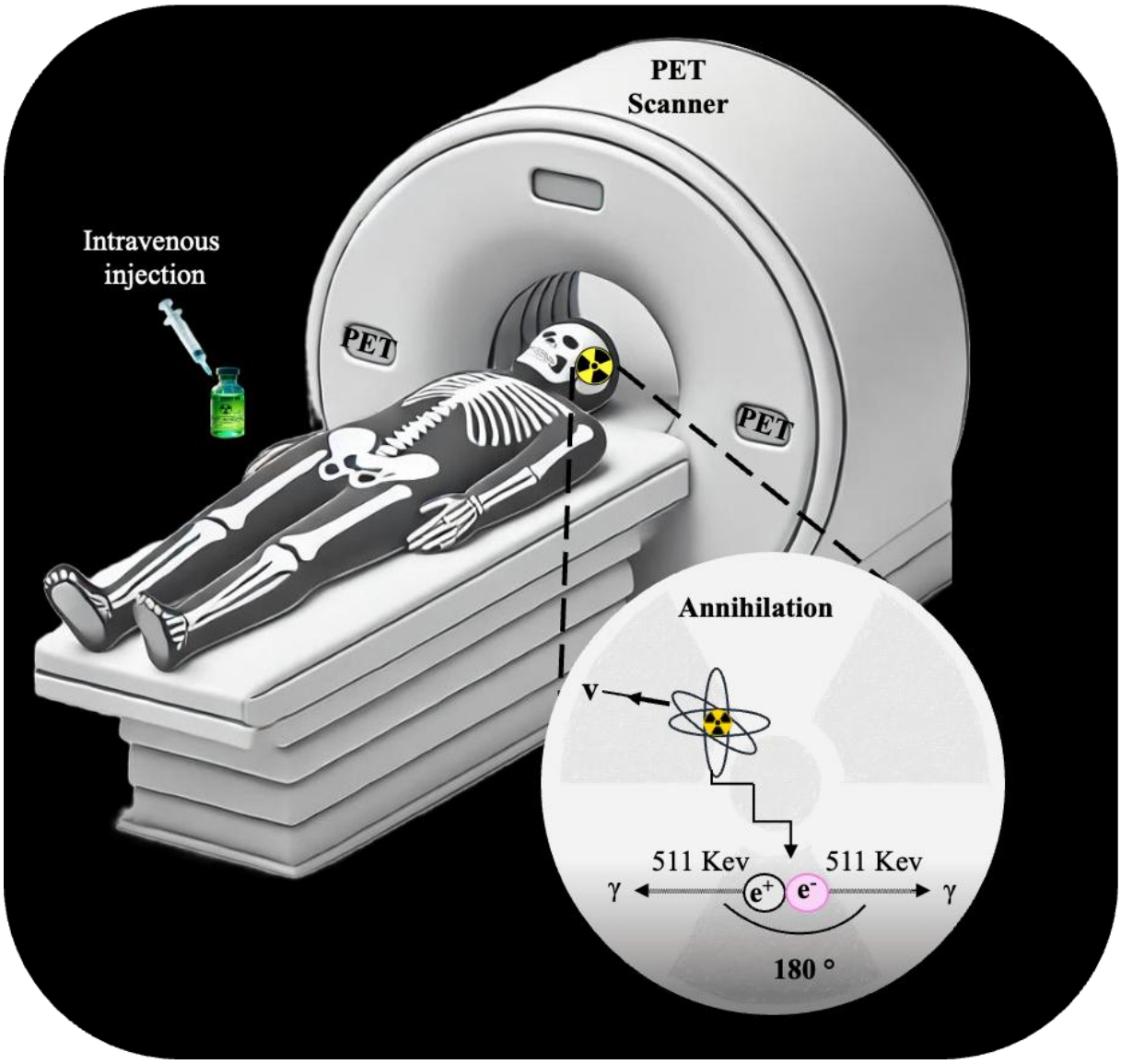

FIGURE 1 The β^+ decay of a nucleus releases a neutrino (ν) and a positron (e^+), which interacts with surrounding electrons, losing kinetic energy through collisions. After slowing down, the positron annihilates with an electron (e^-), producing two photons (γ) with a defined energy of 511 keV and an angle of 180°. *Created using the AI-assisted figure generation workflow described in the "Declaration on AI-Assisted Figure Generation".*

4.3 Radiopharmaceuticals (Radiotracers)

A radiopharmaceutical (or radiotracer) consists of a carrier molecule, radiolabelled with a radionuclide. Depending on the target protein and the application of radiotracer, the carrier molecule can be a small organic molecule or a biomolecule, such as an antibody or peptide. [40, 41]

To develop new radiotracers, it is essential to first identify specific proteins or cell surface receptors (biomarkers) relevant to the pathology or process being investigated. [42-44] Once a suitable biomarker is identified, the next step is to develop or select a targeting molecule with high binding

affinity and selectivity for that biomarker. Antibodies often serve as ideal targeting agents for this purpose due to their high specificity and affinity. Despite their immunogenic potential and large size (about 150 kDa), which limits their ability to pass across the BBB for brain imaging [45], their high specificity to their target makes them optimal carrier molecules for radiotracers. Compared to small molecules, antibodies typically exhibit superior *in vivo* stability, with half-lives ranging from days to weeks. [31] They often demonstrate higher affinity for their targets, with dissociation constants (Kd) frequently in the nanomolar to picomolar range. This makes them essential biological agents for diagnostic and therapeutic purposes. Their high affinity and specificity result in low background noise and high-quality images. [46, 47] The last step of radiotracer development is radiolabeling. It is critical that the radiolabeling does not impair the binding ability and affinity of the binder for its target. Figure 2 provides a schematic representation of radiopharmaceuticals.

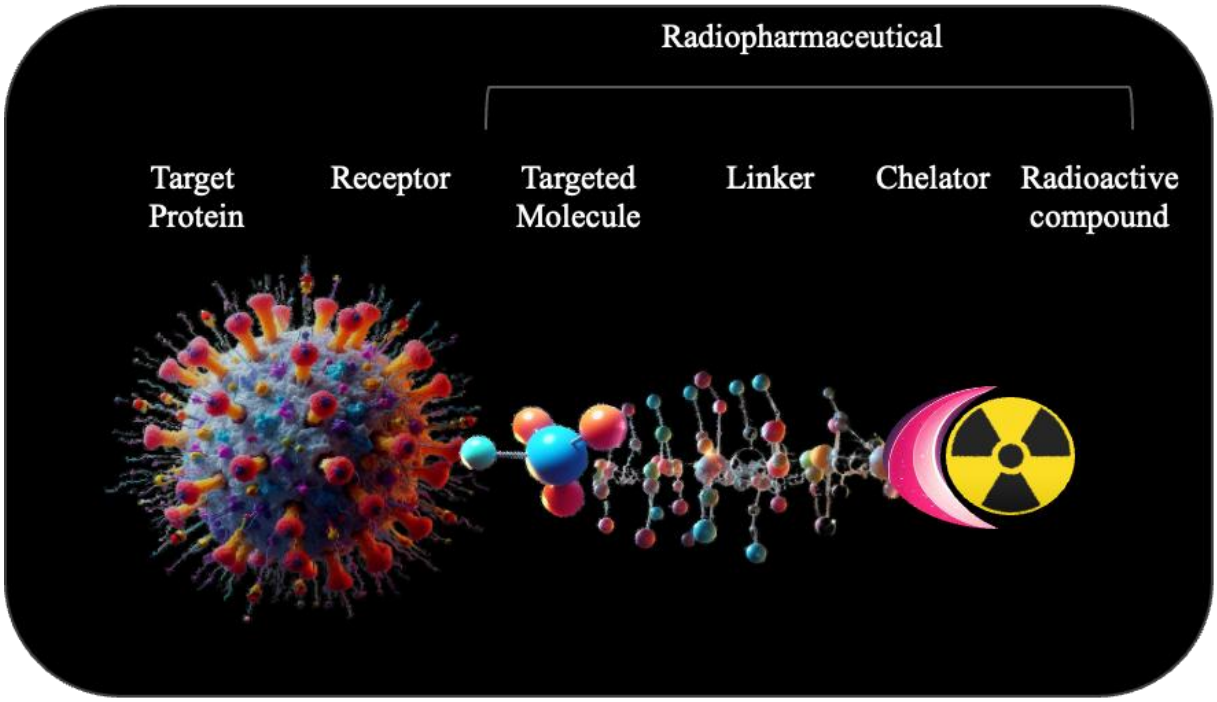

FIGURE 2: Schematic representation of radiopharmaceuticals comprising four main components: 1) radioactive compound, 2) Chelator/Bifunctional chelator (BFC) and radiometal complex: BFC used in peptide-based radiopharmaceuticals, 3) linker: connects the radionuclide to the targeted molecule, and 4) targeted molecule: can be an antibody that specifically binds to the target protein. Adapted from [48] *Created using the AI-assisted figure generation workflow described in the "Declaration on AI-Assisted Figure Generation".*

The selection of an appropriate radionuclide is essential in the development of a new radiotracer, especially those based on antibodies. In the following chapter, the importance of this is discussed in detail.

4.4 Radionuclides

Radionuclides are unstable atomic nuclei that possess an excess amount of energy, neutrons, and protons. In addition to naturally occurring radionuclides, they can be artificially produced. Neutron-rich radionuclides are typically produced in nuclear reactors, while proton-rich radionuclides are generally produced in cyclotrons.

PET uses small amounts of radiotracers to detect biological processes and changes. The choice of radionuclide for the development of radiotracers, particularly when working with antibodies, requires considering several fundamental factors:

1) The physical properties of the radionuclide, such as the radiation dose of the radionuclide in the body, the type of radiation emitted (α, β, γ), radiation energy, and the half-life of the radionuclide.

2) The chemical properties, such as *in vivo* stability, radiochemical purity, and specific activity.

3) The labeling method used for the antibodies, whether covalent binding or chelation. [49]

Antibodies are large molecules having a size of 150 kDa. They have a long biological half-life in the bloodstream, ranging from several days to weeks. This extended duration in the bloodstream requires a radionuclide with a longer physical half-life that allows imaging at later time points to generate high-quality PET images. [49] To achieve optimal imaging, the physical half-life of a radionuclide should ideally match or slightly exceed the biological half-life of an antibody. Additionally, longer half-lives radionuclides are well-suited for investigating the slower kinetics of labeled antibodies with long biological half-lives. [50] This ensures that sufficient radioactivity remains when the antibody reaches its target and optimal biodistribution is achieved. In addition, the signal-to-background ratio is favorable at the time of imaging and unnecessary radiation exposure to the patient is minimized. [49, 50]

^{18}F ($t_{1/2}$ = 109.80 min, β_{max} = 634 KeV) and ^{68}Ga ($t_{1/2}$ = 67.62 min) are two favorable positron-emitting radionuclides widely used for PET imaging. [51] ^{44g}Sc ($t_{1/2}$ = 3.97 h, β and γ emitter) is an interesting radionuclide used for therapy and diagnostics that provides images with higher contrast than ^{68}Ga primarily due to its lower mean positron energy (0.63 MeV vs 0.83 MeV for ^{68}Ga). This results in a shorter positron range, leading to better spatial resolution and image quality. ^{89}Zr ($t_{1/2}$ = 78.40 h, β_{max} = 897 KeV) and ^{64}Cu ($t_{1/2}$ = 12.70 h, β_{max} = 653 KeV) are two preferred radiometals with longer half-lives for antibody labeling and PET imaging at later time points. Both radionuclides, ^{89}Zr and ^{64}Cu, have low positron energy, which leads to better image resolution. [52] ^{89}Zr has some drawbacks, such as high-energy γ emissions and a longer half-life (78.4h) that collectively result in an unfavorable absorbed dose for patients. [53] In contrast, copper-64 with a half-life of

12.7 h, emerges as the preferred radionuclide for labeling antibodies. Both ^{89}Zr and ^{64}Cu allow for imaging at later time points due to their relatively long half-lives, which is beneficial for antibody-based tracers. However, ^{64}Cu offers the advantage of lower radiation exposure to the patient compared to ^{89}Zr, while still providing a sufficient time window for imaging.

4.5 Copper-64

Copper-64 (^{64}Cu), with a half-life of 12.7 h, is the most commonly used isotope among its groups (^{60}Cu, ^{61}Cu, ^{62}Cu, and ^{67}Cu) for medical use (Table 1). The 12.7-hour half-life of copper-64 enables its production at centralized cyclotron facilities and its distribution to other imaging centers. This enhances its accessibility for clinical and research applications. While the production of copper-64 is complex, this radionuclide's 12.7-h half-life allows for imaging at later time points post-injection which is advantageous for antibody-based tracers with slower pharmacokinetics. Copper-64 emits β^- (38 %, max = 0.579 MeV) and β^+ (18 %, max = 0.655 MeV) particles, and undergoes electron capture (EC = 44 %) with an internal conversion to gamma radiation (γ = 0.47 %, 1346 KeV) (Figure 3). [54, 55]

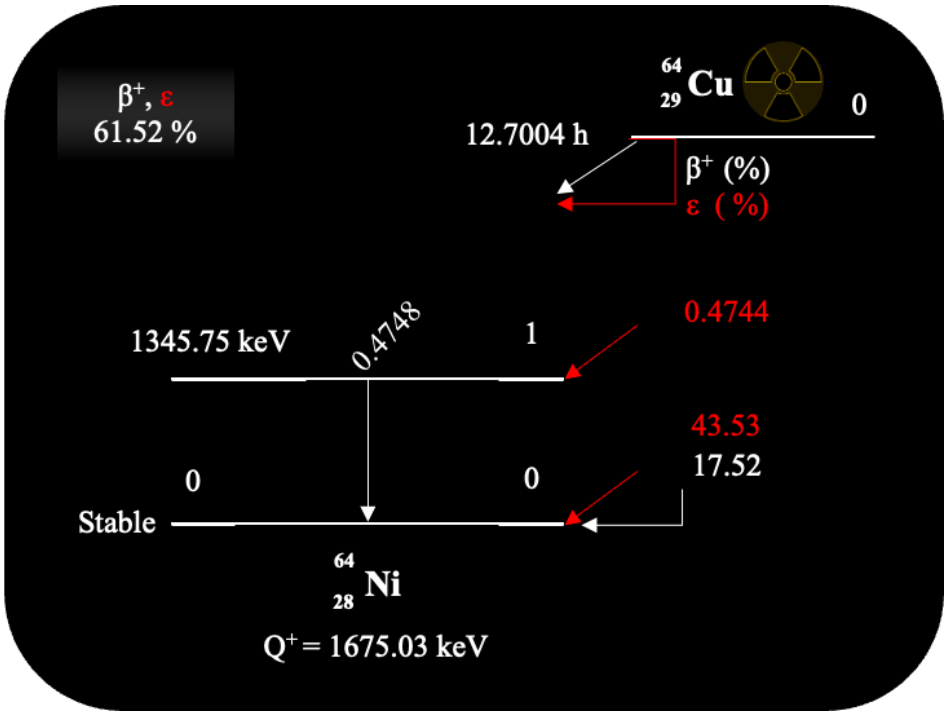

FIGURE 3: Decay scheme and energies of copper-64 (β^-, β^+, and EC). Adapted from [56]

Because of these emission types, copper-64 can be used for diagnostic (β^+) and therapeutic (β^-) purposes. This makes it an interesting radionuclide among all long-lived radionuclides. [57, 58] The therapeutic effect of Copper-64 is mainly due to the high-linear-energy-transfer (LET) of Auger

electrons rather than its beta radiation. These Auger electrons are particularly effective for treating micrometastases because of their short range and high ionizing power when they enter cells. However, there are some limitations for therapeutic use: 1) The therapeutic dose of ^{64}Cu is significantly greater than the diagnostic amount, raising concerns about toxicity. 2) Half-life of ^{64}Cu may be too short for some therapeutic purposes. 3) The average absorbed radiation dose from ^{64}Cu may be insufficient to treat greater tumors adequately.

A list of copper radioisotopes and their respective applications is provided in the table below:

	Half-life	Type of decay	Average energy of β+ emissions (KeV)	Average energy of β- emissions (KeV)	Application
^{60}Cu	23.7 min	β+ = 93% EC = 7%	970	-	Diagnostic
^{61}Cu	3.33 h	β+ = 61% EC = 39%	500	-	Diagnostic
^{62}Cu	9.76 min	β+ = 97% EC = 2%	2910	-	Diagnostic
^{64}Cu	12.7 h	β+ = 17.6% β- = 38.5% EC = 43.9%	278	191	Diagnostic, Therapy
^{67}Cu	61.83 h	β- = 100%	-	141	Therapy

TABLE 1: Copper radioisotopes and their applications in nuclear medicine. Five isotopes (^{60}Cu, ^{61}Cu, ^{62}Cu, ^{64}Cu, and ^{67}Cu) are particularly relevant for medical use. Copper-64 with a 12.7 h half-life, decays via β^+, EC, and β^-, making it potentially suitable for both diagnostic imaging and therapeutic applications, though its therapeutic use remains investigational. Adapted from [58]

Two main methods are routinely used for the production of ^{64}Cu: reactor and cyclotron-based methods. The cyclotron-based method is the most commonly used for utilizing the ^{64}Ni(p,n)^{64}Cu reaction. Copper-64 production can be accomplished through either a fully automated or custom-built system to ensure consistent and efficient synthesis of radioisotope. The production of ^{64}Cu involves a multi-step automated process. Initially, a ^{64}Ni$(SO4)_2$ solution is electroplated onto a shuttle in a closed system (Figure 4A-B). Following the plating step, the nickel target is purified, dried, and transported to the cyclotron for proton irradiation (Figure 4C target). After irradiation, the shuttle returns to the dissolution cell (Figure 4A) where the irradiated target is dissolved. The resulting solution containing ^{64}Cu and other byproducts is transferred to a purification cell. In this cell, ion exchange chromatography is employed to separate ^{64}Cu from other radionuclides (Figure 4B). Short-lived copper isotopes are allowed to decay, while other contaminants (including nickel

isotopes and cobalt-55, -57, and -61) are removed using varying concentrations of HCl (6 M and 4 M) (Figure 4B). The purified ^{64}Cu is then eluted from the column using 0.1 M HCl (Figure 4D), yielding the final [^{64}Cu]$CuCl_2$ product ready for subsequent radiochemical applications. [59]

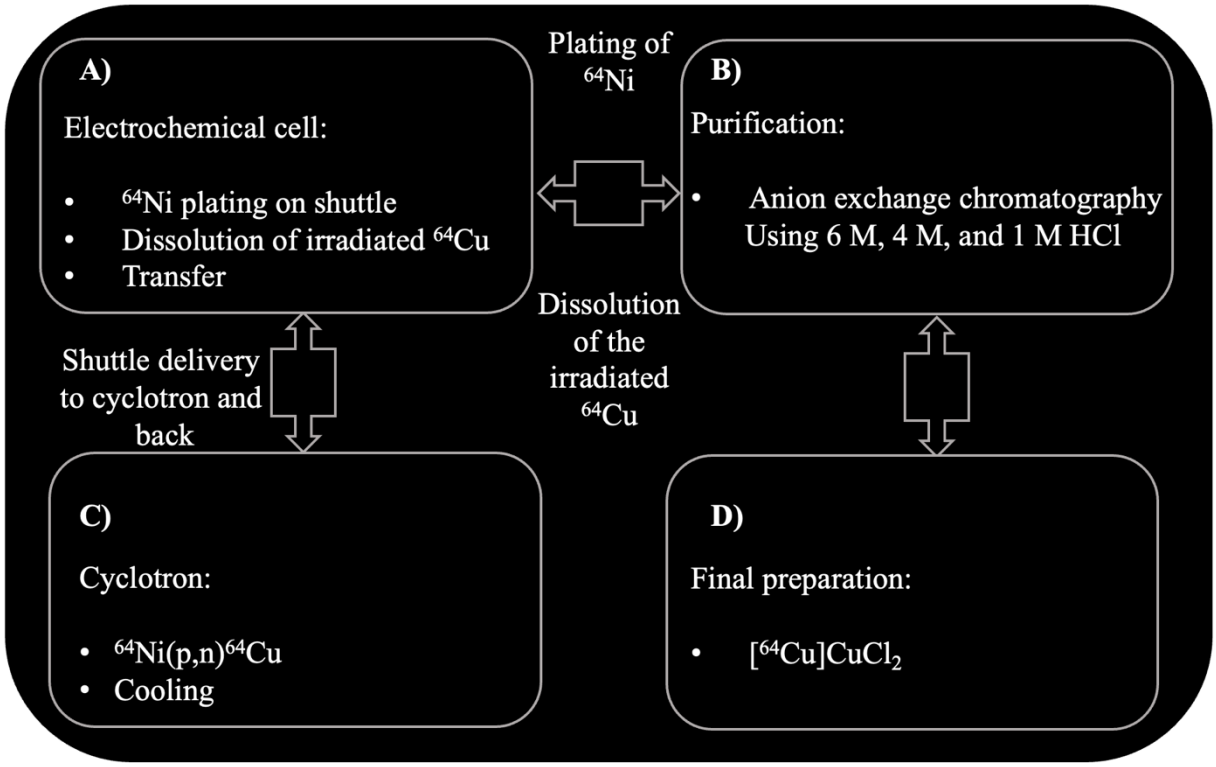

FIGURE 4: Schematic representation of automated copper production. The $^{64}Ni(SO_4)_2$ solution circulates between cells A and B in a closed electrochemical system. The nickel deposited on a shuttle is delivered into a cyclotron for irradiation via a delivery pipe. During the irradiation, the shuttle is cooled from above by helium gas and from below by water. After the irradiation, the shuttle is sent back to cell A to dissolve irradiated copper. After the dissolution, the copper solution is purified from other nuclides in cell B. The [^{64}Cu]$CuCl_2$ is transferred to the cell D for the final preparation. Adapted from [59]

4.6 Radiochemistry

A highly effective and reliable process for developing radiotracers is antibody conjugation. In this method, an antibody is modified using a chelator and then labeled with a radioactive isotope. Chelators are chemical compounds with one or more free electron pairs (electron donors). They form coordination bonds with a central metal ion (cation), creating a cage-like structure. A bifunctional chelator binds covalently to antibodies on one side, chelates a radiometal on the other side and delivers a radiometal to the target molecule. [60] Antibody modification using a chelator serves as a one-step radiolabeling process. This simplifies and accelerates the process and reduces the potential risks of multiple administrations. The selection of chelator and metal-ion is an important step. Choosing a suitable chelating agent depends on the oxidation state and physical properties of the

radiometal ion. [60] In addition, the chelator must be specific for the metal ion. The stability of chelator-metal ions is crucial in preventing transchelation and the release of free metal ions *in vivo*. The kinetic inertness of the complex is another important factor, as the complex demonstrates deligation behavior in the acidic state (pH = 2).

The unique coordination chemistry of copper enables it to be used in PET imaging. Copper-64 forms stable complexes with various chelator systems that can be linked to biologically relevant molecules. [61, 62] Copper has three oxidation states, I, II, and III. Cu(I) and Cu(III) complexes are unstable and difficult to obtain, respectively, which makes them unsuitable for radiopharmaceutical applications. In contrast, Cu(II), which has a d9 configuration and coordination numbers of 4 to 6, can form stable complexes with amines, imines, and bidentate ligands. Tetraazamacrocyclic ligands are the most commonly used chelators for reacting with ^{64}Cu, such as DOTA, and TETA. [61] Due to the geometrical features of macrocyclic ligands, they enhance the kinetic and thermodynamic stability of ^{64}Cu complexes. *p*-NCS-benzyl-NODA-GA is another macrocyclic ligand used for chelating ^{64}Cu, exhibiting high stability *in vivo*. [53, 63] The structure of three macrocyclic ligands suitable for ^{64}Cu complexing is provided in Figure 5.

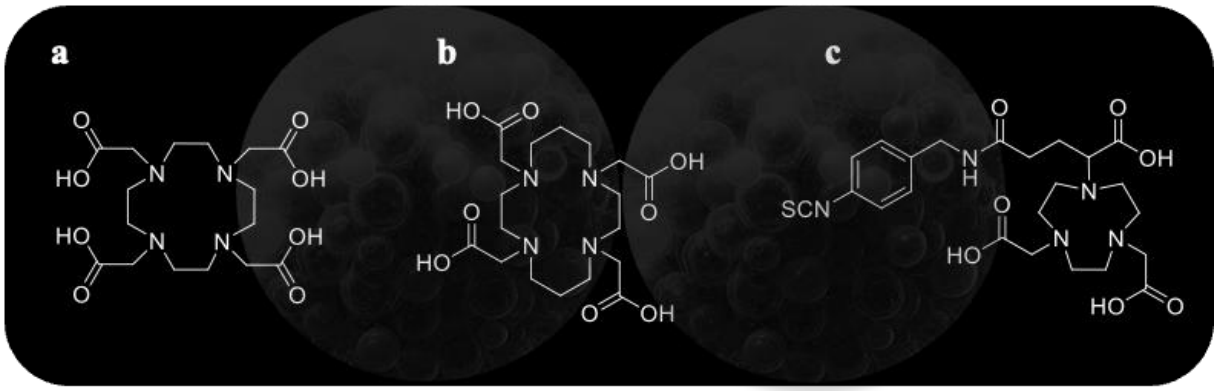

FIGURE 5 Structure of certain macrocyclic chelators that form complexes with copper: a) DOTA, b) TETA, c) *p*-NCS-NODA-GA.
Created using the AI-assisted figure generation workflow described in the "Declaration on AI-Assisted Figure Generation".

The pre-targeting method is an alternative approach for attaching a radioisotope to an antibody (Figure 6). [64] A bivalent antibody is injected into the body to interact with its target, initially before introducing a small radiotracer. The small radiotracer specifically binds to the bivalent antibody and enables PET imaging of the target *in vivo*. [64]

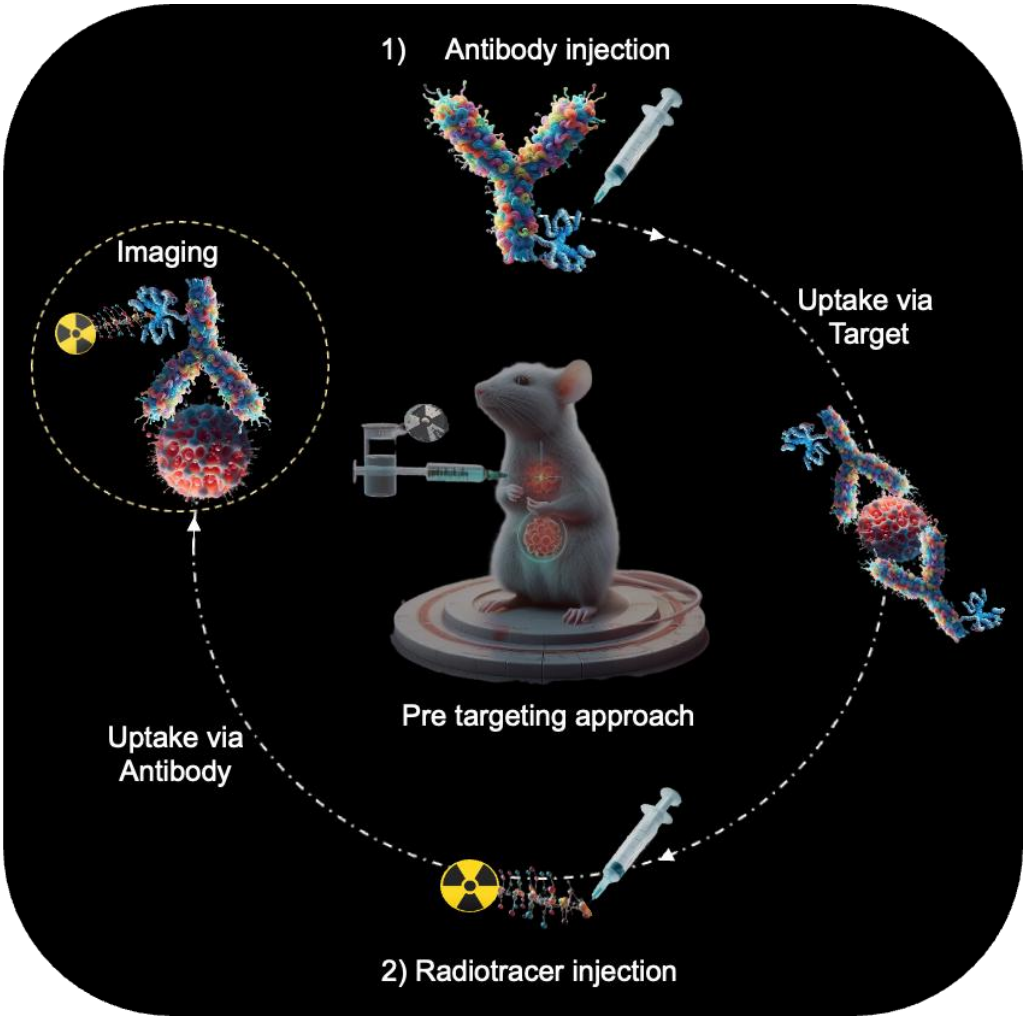

FIGURE 6: Schematic representation of a two-step pre-targeting strategy. In the first step, a bivalent antibody is injected into the body and allowed to interact with its target, which can take several days to accumulate in the target. After the clearance of non-bound antibodies from the blood, a small radiotracer is injected into the body. *Created using the AI-assisted figure generation workflow described in the "Declaration on AI-Assisted Figure Generation".*

Several methods such as the antibody-hapten (streptavidin-biotin) [65], antibody-oligonucleotide conjugation [65], and bioorthogonal Diels-Alder click chemistry [66] are developed for the pre-targeting approach. However, these strategies face complexities and cost challenges that restrict their widespread application. [66] One significant drawback of this approach is the time-consuming nature of each step. In addition, the effectiveness of this method is highly dependent on the precise dosage of the antibody. Using either excessive or extremely low dosages can significantly impact outcomes. [67] Given these limitations, this thesis focuses on developing radiotracers for PET imaging of activated microglia and Poly-GA protein by directly modifying antibodies with the *p*-NCS-NODAGA chelator.

4.7 PET Imaging of Activated Microglia Targeting TREM2

Neuroinflammation is a significant feature in many NDDs. [68, 69] Microglia cells are the resident macrophages in the brain and are considered the main drivers of neuroinflammation. Microglia have their exclusive origins in erythromyeloid progenitors located in the yolk sac (YS). [70, 71]

In a homeostatic state, microglia maintain normal brain function and surveil the brain environment for abnormalities. [70, 72, 73] In response to neuronal injuries, microglia act as the primary defense mechanism. [28, 68] They shift from a homeostatic state to an activated phenotype known as disease-associated microglia (DAM). [74-77] In chronic pathological conditions, microglia can persist in an activated state, leading to sustained activation and perpetuation of chronic inflammatory processes in the central nervous system. [4, 77, 78] Microglial morphology is not limited to two distinct states. They exist in various intermediate states between the homeostatic and activated forms [79, 80] (Figure 7), allowing them to display a wide range of functions depending on the specific environment in which they are situated.[70, 81] Microglia transform from their resting morphology, characterized by long branches, to a rounded and formless shape termed amoeboid. [70, 82, 83] When microglia are in their activated phenotype, they play an important role in responding to injuries in the brain. This response triggers the secretion of various substances, including proinflammatory cytokines such as tumor necrosis factor-α (TNF-α) and interleukins (IL-1β, and IL-6), chemokines and other mediators such as reactive oxygen and nitrogen species (ROS and RNS), as well as the expression of nitric oxide synthase (iNOS) and cyclooxygenase-2 (COX-2). These substances contribute to the inflammatory response and may modulate the progression of neuroinflammation. [70, 81]

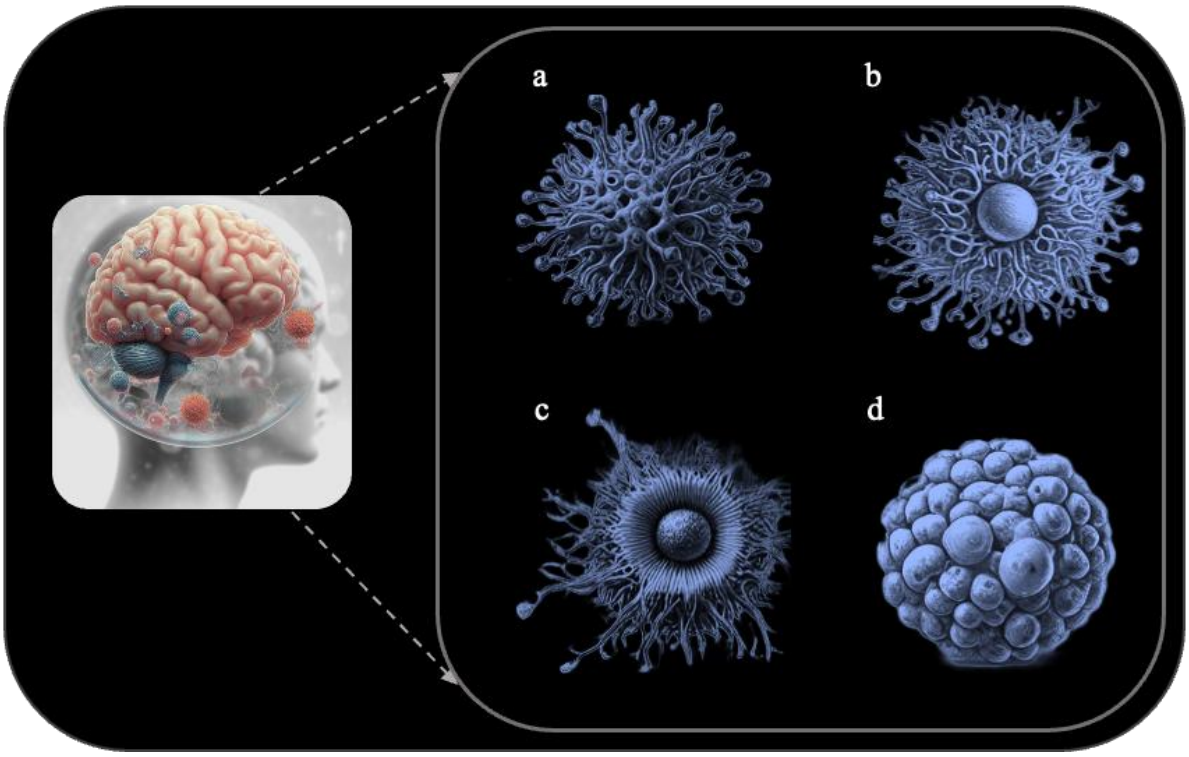

FIGURE 7: Different types of Morphological states of microglia in the human brain: a) Ramified or resting microglia: characterized by small cell bodies and long, branched processes b) Mildly activated hyper-ramified microglia have increased branching and lengthening of processes, along with proinflammatory cytokine secretion. c) Bushy morphology represents intermediate activation, with swollen processes and enlarged cell bodies. d) Amoeboid or phagocytic microglia have round macrophage-like shapes, few processes, and are linked to high proinflammatory activation, oxidative radicals, and microglial apoptosis. [72, 73, 84, 85]
Created using the AI-assisted figure generation workflow described in the "Declaration on AI-Assisted Figure Generation".

Dysregulation of immune responses in the CNS occurs in the early stages of NDDs and may play a significant role in disease progression even before the manifestation of NDD pathology. [68, 69, 86] This highlights the importance of imaging activated microglia, a hallmark of neuroinflammation, for the early diagnosis of NDDs and consequently the application of a broader range of therapy options for patients. [86]

The most commonly used biomarker for imaging neuroinflammation is the 18 kDa translocator protein (TSPO). [87] TSPO is expressed in the mitochondrial membrane and its overexpression is observed in brain injury and neuroinflammation. [88-90] Therefore, TSPO can be detected using a radiotracer. The first generation of the TSPO-PET tracer, ^{11}[C]-(R)-PK11195, revealed some limitations, including a short half-life of ^{11}C, low signal-to-background ratio, and challenging radiochemistry. [91, 92] [^{18}F]GE180 tracer, targeting TSPO as the third-generation tracer, revealed significant brain uptake with a longer half-life as well as more affinity for the TSPO. [93] It is important to mention that TSPO PET has certain limitations for imaging cerebral neuroinflammation. TSPO

PET cannot distinguish between different microglial phenotypes; therefore, cannot provide specific information on the function of activated microglia. TSPO is also expressed on various kinds of cells, notably astrocytes and other neuronal cells, decreasing the specificity of activated microglia imaging. [87, 94] Furthermore, the existence of allelic variations within human populations exhibiting lower TSPO binding levels limits the application of TSPO PET in diagnostics. [95] Given these limitations of TSPO PET, there is an urgent need to identify and develop alternative PET biomarkers that offer more specificity for activated microglia. Such biomarkers would not only enhance the accuracy of neuroinflammation imaging but also provide additional information about microglial activation levels in various neurodegenerative conditions.

Microglia function and activation are strongly associated with a type-1 transmembrane protein known as the TREM2. [96-98] TREM2, which is an immune receptor, can be found on microglia in the brain. Bone osteoclasts, dendritic cells, and other macrophages also express TREM2. [99-102] TREM2 is composed of two main parts which are an extracellular immunoglobulin (Ig)-like domain (V-type) and a short cytoplasmic tail. [103] The full-length TREM2 is associated with a DNAX-activating protein (DAP12) that regulates various microglial activities,[104] such as microglia migration, [105] proliferation, [75] lipid processing, [106] and phagocytosis of Aβ plaque. [105, 107] Moreover, TREM2 regulates the state of microglial cells within the brain and their transition from homeostasis to DAM. [75, 96, 108, 109] Microglial cells play a crucial role in the development of NDDs. While numerous genetic factors influence microglial activation, mutations within the TREM2 gene's coding sequence have gained significant attention as key risk factors. These TREM2 variants stand out among the various genetic components associated with microglial function in NDDs.[110, 111] Homozygous variants of TREM2 are associated with Nasu Hakola[112], while heterozygous TREM2 variants are linked to various NDDs such as AD, frontotemporal Lobe dementia (FTD-L), or ALS. [110, 111, 113-117] TREM2 polymorphism is associated with late-onset Alzheimer's disease (LOAD). [110, 111, 118] Full TREM2 can be cleaved by proteins called ADAM10/17 into soluble TREM2 (sTREM2), which can be detected in CSF and blood plasma. Both TREM2 mutations within the IgG domain (p.T66M and p.Y33C) [107, 119], and within the stalk region (p.H157Y) [107] affect the levels of sTREM2 in the CNS and result in a loss of TREM2 function. [120, 121] Loss of TREM2 function maintains microglia in a homeostatic state which prevents them from transforming into DAM. This results in reduced phagocytic activity of microglia cells.[74, 105] Consequently, microglia cannot effectively combat amyloid pathology leading to increased Aβ plaque accumulation. [122] Various studies have demonstrated a range of agonistic anti-TREM2 antibodies that target both mouse and human TREM2. [123] The agonistic AL002 antibody is a monoclonal antibody against

human TREM2 (hTREM2) and has shown a reduction of Aβ plaque aggregation. [124] In another study, the agonistic DNL919 antibody which targets hTREM2 is currently undergoing a phase 1 clinical trial with healthy adults. The trial aims to evaluate the safety, tolerability, and pharmacokinetics of the DNL919 antibody.

TREM2 as an important player for various NDDs may be a promising biomarker for imaging of activated microglia. Monitoring of microglia *in vivo* over time is achievable by development of a tracer targeting TREM2. Microglia imaging provides crucial information on activation levels of microglia and NDD progression. This is essential for an early diagnosis, timely interventions and prompt treatment for patients. Table 2 provides a summary of developed tracers targeting TREM2 in NDD, cancer, and atherosclerosis.

Tracer	Target
^{68}Ga-NOTA-COG1410 [125]	Mouse TREM2 on TAMs
^{124}I-labelled antibody fragments [126]	hTREM2 in gastric carcinoma
[^{124}I]mAb1729-scFv8D3CL [69]	Mouse TREM2 for Neuroimaging
[^{64}Cu]Cu-NODAGA-4D9 tracer (this work) [127]	Mouse TREM2
[^{64}Cu]Cu-NODAGA-ATV:4D9 tracer (this work) [127]	Mouse TREM2
[^{64}Cu]Cu-NODAGA-14D3 tracer (this work)[127]	hTREM2

TABLE 2: Development of Tracers Targeting TREM2 in Various Diseases.

Despite a few attempts to develop radiotracers targeting TREM2 in neuroscience, no successful *in vivo* imaging has been achieved. *Meier et al.* developed [^{124}I]mAb1729-scFv8D3$_{CL}$ tracer for TREM2 imaging. This tracer consists of ^{124}I-labeled mAb1729 for TREM2 binding and scFv8D3 for TfR-mediated transcytosis. [69] The tracer revealed a low affinity for TREM2, high blood retention and potential for rapid elimination from the target site. Consequently, the tracer was ineffective for *in vivo* imaging of TREM2 and could only detect it *ex vivo*. [69]

Many questions remain open regarding the contribution of microglia to neuroinflammation and disease progression. Therefore, development of new tracers targeting TREM2 may provide an understanding of microglia's functional role at different stages of neuroinflammation.

The 4D9 monoclonal antibody used in this work is an agonistic anti-mouse TREM2 antibody. The 4D9 promotes TREM2 signaling and significantly reduces Aβ plaques in a mouse model. [123] *In vitro* investigations have revealed that the 4D9 antibody binds with high affinity to the stalk region of full-length TREM2 on the cell surface. 4D9 antibody stabilizes TREM2 on the cell surface and activates SYK signaling that results in improved phagocytic activity of microglia. [46, 97, 128] To enhance the penetration of the agonistic 4D9 antibody across the BBB, a transferrin binding site, ATV, was engineered for the 4D9 antibody. [129] The bispecific ATV:4D9 antibody binds at the ATV site to the hTfR on the endothelial cells, enabling an active transport over BBB. [129, 130]

4.8 Poly-GA

In the second part of this study, I developed and evaluated the first tracer targeting poly-GA protein, selected as a biomarker for PET imaging of C9orf72-related frontotemporal dementia (FTD) and amyotrophic lateral sclerosis (ALS). ALS and FTD were historically viewed as separate neurodegenerative disorders, but recent genetic discoveries, particularly mutations in the C9orf72 gene, have revealed significant overlap between the two conditions (Figure 8). ALS-FTD combination is a case in which patients exhibit both diseases. [12, 13] Research indicates that almost 50% of ALS patients have symptoms like those observed in cases with FTD.[22] Moreover, at the time of ALS diagnosis, roughly 15% of patients fulfill the diagnostic criteria for FTD. [131] Conversely, a similar percentage of FTD cases display motor function abnormalities characteristic of ALS. This overlap underscores the complex relationship between these two neurodegenerative disorders. [132]

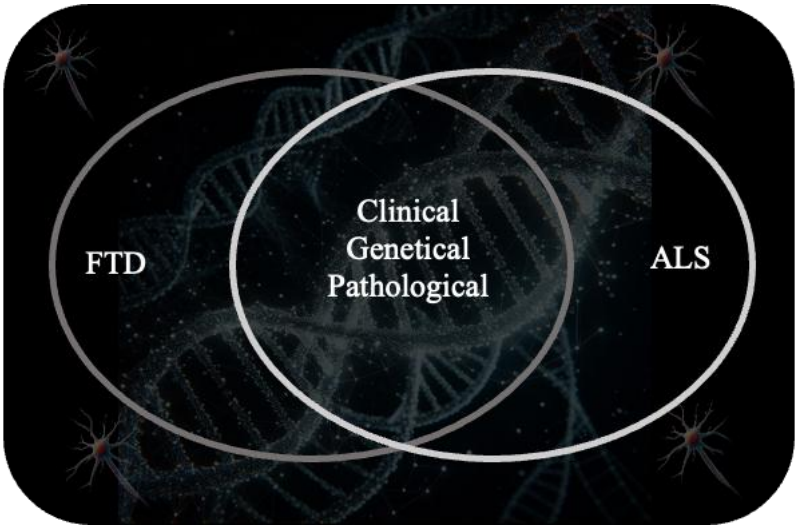

FIGURE 8: FTD and ALS are two forms of NDD that reveal clinical, genetic, and pathological similarities. *Created using the AI-assisted figure generation workflow described in the "Declaration on AI-Assisted Figure Generation".*

The most prevalent symptoms of motor neuron loss in ALS are muscle weakness and progressive paralysis. [12-14] The loss of upper and lower motor neurons in FTD leads to progressive difficulty with speaking, changes in personality, and behavioral changes. [133-135] A significant number of genetic factors are associated with the development of ALS and FTD. The most common among these is the hexanucleotide repeat expansion $(G_4C_2)_n$ in the C9orf72 gene, found in 5 to 10% of all affected patients. [12, 13, 17, 133, 136] The expansion of the C9orf72 repeat is associated with multiple pathological processes, including the aggregation of harmful dipeptide repeat proteins. In healthy individuals, the repeat ranges from 2 to up to 23 hexanucleotides. [137, 138] However, in patients with

C9orf72-mediated ALS/FTD, the expansion repeats are more than 30, often hundreds to thousands. The toxic DPR proteins are highly likely to accumulate in neuronal cytoplasmic and nuclear inclusion of affected patients. [139] Five different dipeptide repeat proteins result from this abnormal translation of G_4C_2 including Poly-GA, Poly-GP, Poly-PA, Poly-GR, and Poly-PR. [135, 139, 140]
Poly-GA inclusions are more commonly observed in the brains of ALS/FTD patients compared to other types of dipeptide repeat (DPR) proteins [139, 141] Poly-GA transmission between cells, which occurs in both cell culture and animal models, is seen as the cause of the progress of neurodegenerative diseases. [142-144] Poly-GA accumulates mainly in neuronal inclusion that are predominantly located in the cerebellum, hippocampus, and neocortex in cases of FTD with TDP-43 pathology and motor neuron disease with TDP-43 pathology. [145] The detection of toxic poly-GA aggregates associated with the C9orf72 gene is an effective method for identifying poly-GA pathology. A study demonstrated the presence of toxic DPR pathology in human brain tissue linked to hexanucleotide repeat expansions in the C9orf72 gene using poly-GA immunohistochemistry on postmortem samples. [146] However, to date, there are no reports that have successfully detected poly-GA *in vivo*.
Zhou et al 2020 demonstrated that the developed mAb1A12 antibody [147] binds specifically to Poly-GA protein and results in reducing cell-to-cell transmission and aggregation of Poly-GA. [142] Treating the cells using anti-GA antibodies showed blocking seeding activity *in vitro*. Therefore, Poly-GA can be considered as a biomarker and its imaging using mAb1A12 antibody [148] provides us useful information about C9orf72 pathology.

5. Study

5.1 General Part and Chemistry

I developed antibody-based radiotracers to image TREM2 and Poly-GA. Antibodies were employed as carrier molecules in the development of radiotracers because of their high specificity and affinity (Table 3).

Antibody	Target
4D9 [76]	Mouse TREM2
ATV:4D9 [129]	Mouse TREM2
14D3 [76]	Human TREM2
1A12	Mouse Poly-GA protein

TABLE 3: The 4D9 antibody and its human transferrin-engineered version bind to the stalk region of mouse TREM2, while the 14D3 antibody binds to the human TREM2. The mAb1A12 antibody binds to the Poly-GA protein in mice and reduces cell-to-cell transmission of Poly-GA.

The 4D9, ATV:4D9, 14D3, and mAb1A12 antibodies were modified using *p*-NCS-NODAGA. A high number of chelators can lead to changes in biodistribution and potentially induce immunoreactivity. Therefore, the number of chelators per antibody must be carefully optimized to maintain the antibody's immunoreactivity and desired biodistribution properties. Using the arsenazo assay, the number of chelators per antibody was determined to be low.

Specifically, 1-2 chelators were bound to 4D9 and ATV:4D9 antibodies, and 1-3 were bound to the mAb1A12 antibody (Table 4). When an antibody undergoes modification, various changes may influence its binding affinity to its receptor. Therefore, the affinity of NODAGA-1A12 to Poly-GA and the potency of NODAGA-4D9 and NODAGA-ATV:4D9 to trigger TREM2 downstream effects were investigated using ELISA and AlphaLISA, respectively. Results demonstrated that the structural changes to the antibodies did not affect their binding to their targets *in vitro*. The radiolabeling process with copper-64 was performed under optimized conditions (42°C, 400 rpm, 30-45 minutes), yielding products with high radiochemical purity (RCP). The reaction parameters were carefully selected to balance efficient labeling with preservation of antibody integrity (Figure 9).

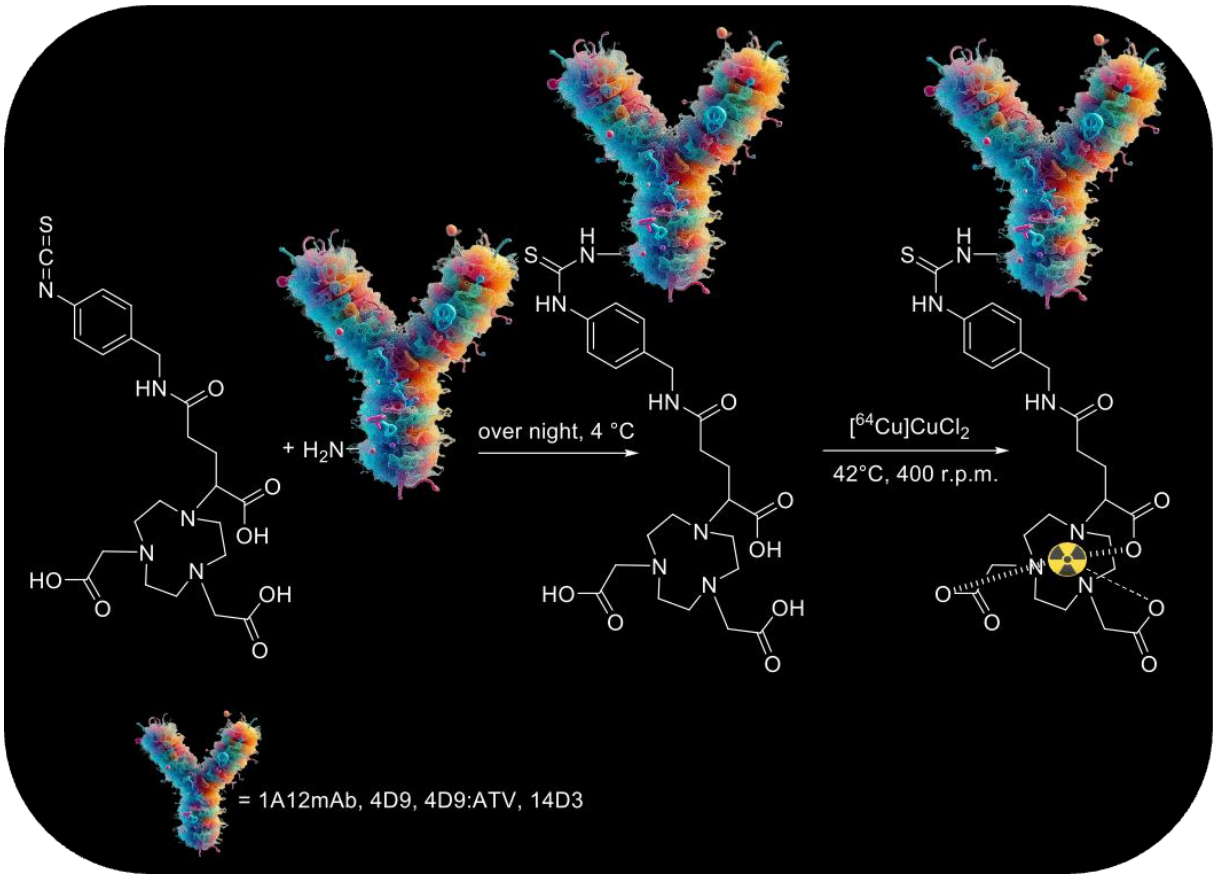

FIGURE 9: The chemical conjugation of the lysine residues on the antibody to the *p*-NCS-NODAGA chelator was followed by the labeling of the modified antibody using copper-64. *Created using the AI-assisted figure generation workflow described in the "Declaration on AI-Assisted Figure Generation".*

The stability of each tracer was then investigated *in vitro* (HPLC) and *ex vivo* (SDS-PAGE and radio-TLC of gel) (Table 4). The radiotarcers' stability is an important factor for delivering the radionuclide to the corresponding receptor *in vivo*. Detached radiometal *in vivo* can accumulate in the liver due to its interaction with certain enzymes such as ceruloplasmin [63]. The *in vitro* and *ex vivo* experiments revealed no free [^{64}Cu]$CuCl_2$ or [^{64}Cu]Cu-NODAGA, confirming the stability of the radiometal-NODAGA complex and tracer stability.

Antibody	**Chelators per Antibody**	***In Vitro* Stability**	***Ex Vivo* Stability**
		HPLC	
ATV:4D9	1-2	Stable over 48 h	• No free copper-64

			• Intact radioracer
4D9	1-2	Not tested	• No free copper-64 • Intact radioracer
1A12	1-3	Stable over 24 h	• No free copper-64 • Intact radioracer

TABLE 4: The number of chelators per antibody was determined using a spectrometric assay. The potency of [^{64}Cu]Cu-NODAGA-ATV:4D9 and the affinity of [^{64}Cu]Cu-NODAGA-mAb1A12 for their respective targets were confirmed by AlphaLISA and ELISA experiments. The *in vitro* stability of each tracer was initially examined in murine plasma. Both [^{64}Cu]Cu-NODAGA-ATV:4D9 and [^{64}Cu]Cu-NODAGA-mAb1A12 demonstrated stability over 48 h and 24 h, respectively. Additionally, *ex vivo* stability analysis was performed using SDS-PAGE and radio-TLC of plasma samples from each tracer injected into WT mice. The intact radiotracers were revealed using SDS page. Furthermore, no other proteins were observed that might have been radiolabeled via trans-chelation. The absence of free copper-64 was subsequently verified through radio-TLC.

The tracers' specificity and distribution were evaluated using mouse brain sections *in vitro*. The specificity of the tracers in the presence of native antibodies was conducted with brain sections from transgenic mice using a blocking experiment (Table 5). Each tracer demonstrated specificity for its target.

Tracer	***In Vitro* Autoradiography**	**Specificity**
TREM2 tracer	Increased tracer uptake in the frontal cortex	• Complete block of targets • Specific binding
Poly-GA tracer	Tracer accumulation in the cortex and hippocampus	• Complete block of targets • Specific binding

TABLE 5: A summary of the results of *in vitro* experiments**.** Tracer-receptor binding was initially investigated using *in vitro* autoradiography on the brain section of 5xFAD;TfR$^{mu/hu}$ mice vs. WT for the TREM2 tracer and GA±CamK2a±

mice vs. controls for the Poly-GA tracer. In the presence of a 1000-fold excess of cold antibody, a complete block of targets was observed in the brains of transgenic, demonstrating the specificity of each tracer to its target.

In the next step, each tracer was characterized *in vivo*. The evaluation of tracers in living organisms is crucial to investigate tracer-target binding, their penetration across the BBB in the CNS, their biodistribution in the brain, and distribution in organs over time. Furthermore, the pharmacokinetics, metabolism, and washout of each tracer can be assessed in a living organism. In this context, non-invasive PET/CT imaging of small animals is an effective tool to investigate the regional uptake of tracers over time. PET imaging enables longitudinal imaging with low radiation exposure. In the presented study 10-minute CT scans were conducted, followed by 30-minute static PET scans at 2, 20, and 40 h p.i.. PET/CT imaging at 20 h p.i. showed the strongest difference between Tg mice and controls for each tracer. Due to the slow kinetics of the antibody and the half-life of copper-64, the time points at 2 h and 40 h post-injection were not suitable for imaging.

Ex vivo analyses were performed following *in vivo* PET/CT imaging to evaluate the biodistribution and pharmacokinetics of the radiotracer. The *ex vivo* biodistribution study complements the *in vivo* imaging data, offering a more detailed understanding of tracer behavior at the organ and tissue level. In addition, it potentially elucidates any off-target accumulation or unexpected pharmacokinetic properties. For this purpose, the brain and various peripheral organs were collected and measured by a gamma counter post-mortem. This quantitative approach enabled precise determination of tracer accumulation in each organ. The resulting data were processed and expressed as either Standardized Uptake Values (SUV) or percentage of injected dose per gram of tissue (%ID/g). (Table 6) These metrics provide normalized measures of tracer uptake, making it easier to compare across different experimental conditions and between subjects.

Target	Definition
Poly-GA imaging	$\text{SUV} = \left(\frac{\frac{tissue\ activity}{(Bq)}}{\frac{tissue\ weight}{(g)}}\right) * \left(\frac{\frac{body\ weight}{(g)}}{\frac{injected\ dosis}{(Bq)}}\right)$
TREM2 imaging	$\%\text{ID} = \left(\frac{\frac{tissue\ activity}{(Bq)}}{\frac{tissue\ weight}{(g)}}\right)\left(\frac{1}{\frac{injected\ dosis}{(Bq)}}\right)$

TABLE 6: After performing *in vivo* and *ex vivo* experiments, the data were analyzed and presented as SUV for the Poly-GA and %ID/g for the TREM2 target.

5.2 TREM2

The crucial role of TREM2 in regulating microglia signature and its association with AD was the reason for selecting TREM2 as the biomarker for the first part of the study. The development of a new radiotracer targeting TREM2 enables the monitoring of microglia activation and may also provide an understanding of microglia's functional role at different stages of neuroinflammation.

The agonistic 4D9 antibody [76] was developed based on the discovery of TREM2 shedding at p.H157 by ADAM 10/17. [123] The 4D9 antibody binds to the TREM2 epitope near the cleavage site, inhibiting TREM2 shedding and therapeutically simulating the protective TREM2 signaling. To improve the BBB permeability of 4D9, the ATV shuttle was engineered to 4D9. This is an hTfR binding site and enables active transport of bispecific ATV:4D9 into the brain. [129] Using the TfR to enhance the active transport of therapeutic antibodies is an effective technique for increasing antibody accumulation in the CNS. [46] For TREM2 imaging, an Alzheimer's mouse model (5xFAD) carrying five mutations related to amyloid precursor protein (APP) and presenilin (PSEN1) was used: APP V717I (London), APP KM670/671NL (Swedish), APP I716V (Florida), and PSEN1. The 5xFAD mice exhibit early beta-amyloid (Aβ-42) plaque accumulation in the cortex and hippocampus at the age of 2 months, which is associated with microglial activation. TREM2 is expressed at higher levels in the white matter and hippocampus regions of the CNS in this mouse model compared to other regions. It has been demonstrated that the expression of TREM2 increases with age. [149, 150] At 6-7 months of age, the mice show the highest APP expression and related high microglial activation, which may elevate tracer uptake and consequently maximize TREM2 PET imaging. Therefore, performing PET imaging at this age in the mouse model may reveal the highest tracer uptake in the brain. In addition to evaluating the TREM2 binding ability of the 4D9 tracer in 5xFAD and its corresponding wild-type C57BL/6 model, the ATV: 4D9 tracer (hTfR-modified bispecific antibody) was evaluated in a mouse model crossed with a human transferrin receptor knock-in (5xFAD; $TfR^{mu/hu}$). This allows the active transport of the tracer into the CNS (Figure 10). Thus, it is possible to compare tracer uptake in mice lacking the hTfR, where transport occurs through passive diffusion, with uptake facilitated by an active receptor-mediated mechanism across the BBB. As a control group, wild-type hTfR knock-in mice (WT; $TfR^{mu/hu}$) were shown to be suitable for this purpose.

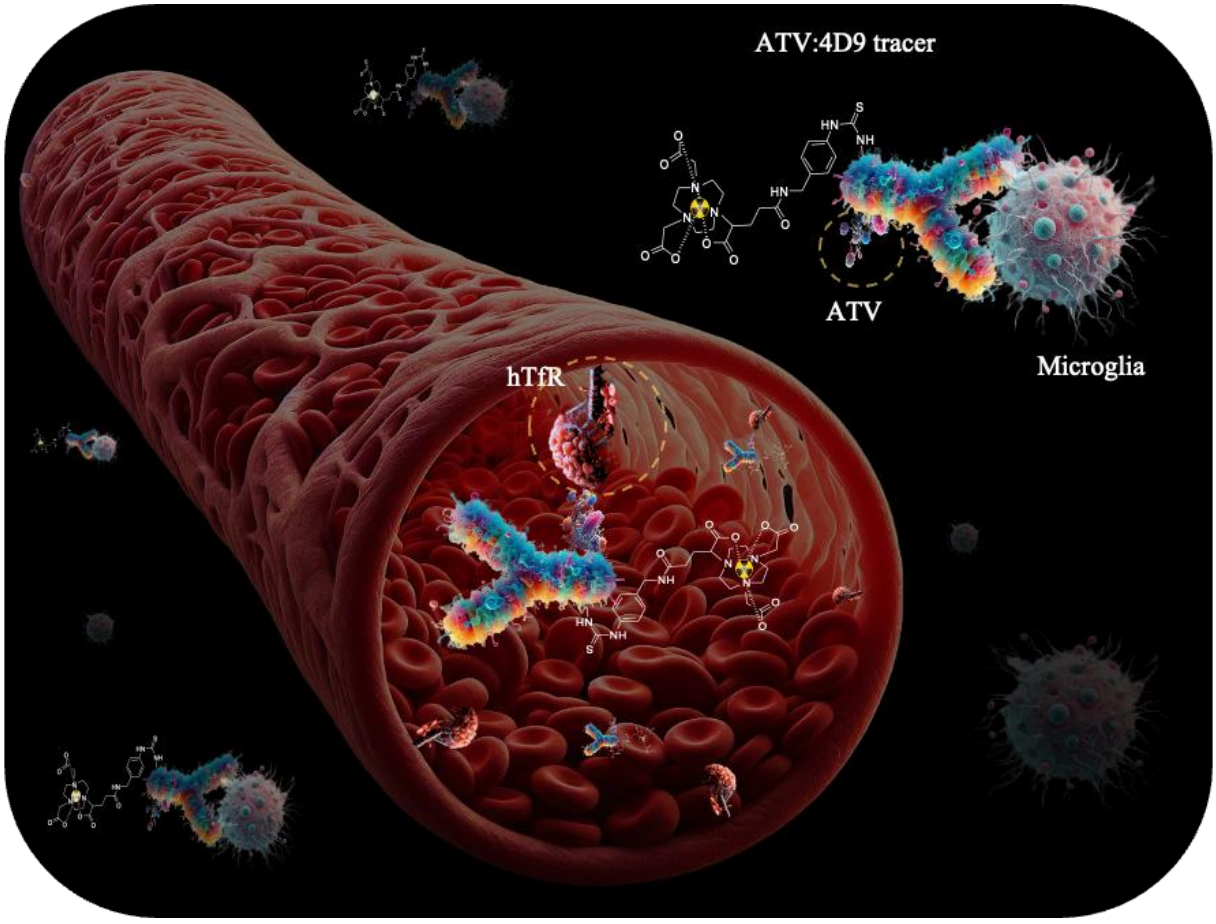

FIGURE 10: Schematic representation of active transport via the transferrin receptor (TfR). The ATV:4D9 tracer binds to the human transferrin receptor (hTfR) via its ATV binding site, allowing it to penetrate the BBB. Additionally, the tracer interacts with TREM2 on microglial cells through its antibody component. *Created using the AI-assisted figure generation workflow described in the "Declaration on AI-Assisted Figure Generation".*

The *App*^{SAA}; TfR$^{mu/hu}$ mouse model represents another independent AD mouse model that was used in scRadiotracing experiments to prove cellular selectivity for microglia. Table 7 lists the tracers targeting mouse and human TREM2 and the respective mouse models in which they were tested.

Tracer	Mouse line
[^{64}Cu]Cu-NODAGA-4D9	5xFAD
[^{64}Cu]Cu-NODAGA-4D9	WT
[^{64}Cu]Cu-NODAGA-ATV:4D9	5xFAD; TfR$^{mu/hu}$

[^{64}Cu]Cu-NODAGA-ATV:4D9	WT; TfR$^{mu/hu}$
[^{64}Cu]Cu-NODAGA-ATV:4D9	*App*^{SAA}; TfR$^{mu/hu}$
[^{64}Cu]Cu-NODAGA-14D3	Human brain tissue with AD

TABLE 7: A list of mouse lines used for *in vivo* experiments: Each tracer was intravenously injected into the tail of the corresponding mouse group. The PET/CT scan was performed in a time series of 2, 20, and 40 h p.i..

TREM2-specific tracers revealed high specificity for their corresponding target. Increased tracer uptake was observed in frontal cortex of Tg mice compared to their corresponding WT group. The brain uptake of the [^{64}Cu]Cu-NODAGA-ATV:4D9 tracer in the brain of the hTfR knock-in mouse model was significantly higher than in those without the hTfR knock-in. This can be explained by improved BBB penetrance of the [^{64}Cu]Cu-NODAGA-ATV:4D9 tracer by utilizing the ATV technology. Specifically, the [^{64}Cu]Cu-NODAGA-ATV:4D9 uptake in the brain of 5xFAD; TfR$^{mu/hu}$ mice was 4-fold higher than in 5xFAD mice, and there was 4.6-fold higher uptake in the brain of WT; TfR$^{mu/hu}$ mice compared to WT. The schematic representation of the [^{64}Cu]Cu-NODAGA-ATV:4D9 binding to TREM2 is shown in Figure 11.

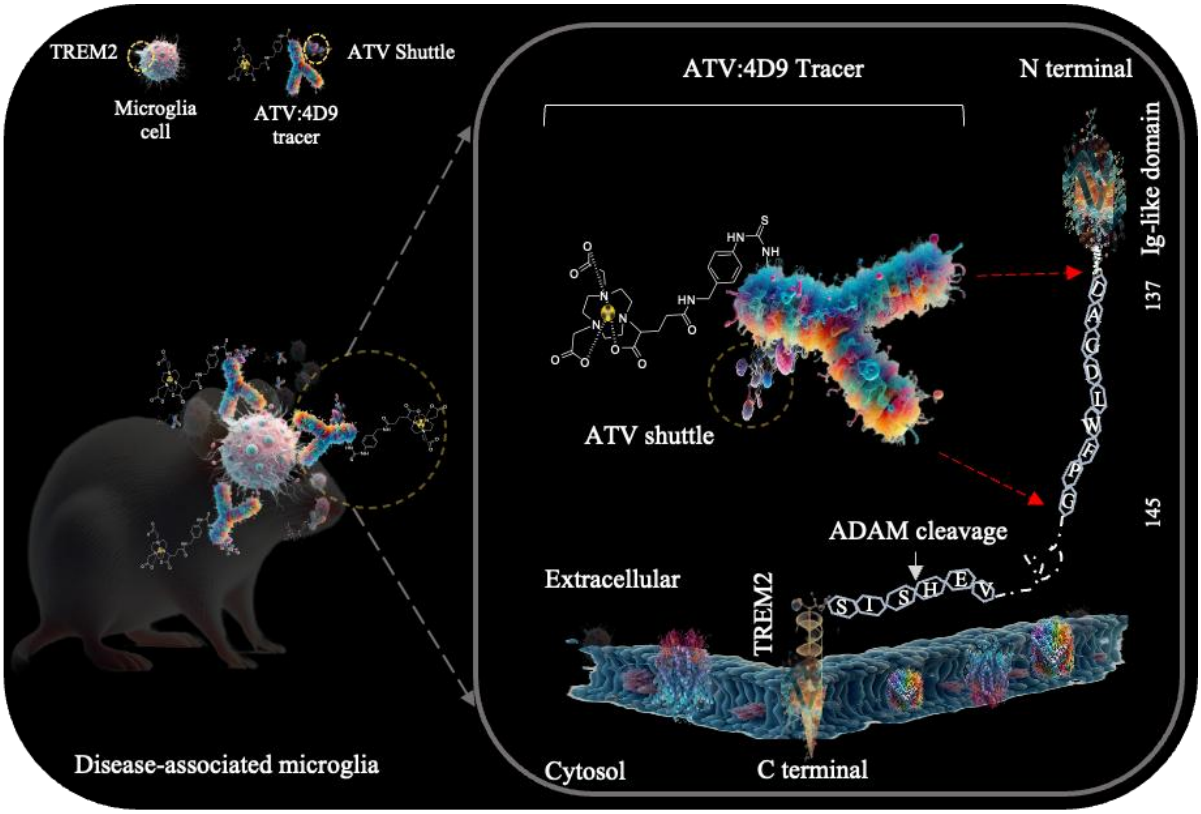

FIGURE 11: The copper-64 radiolabeled bispecific ATV:4D9 antibody binds to the stalk region of TREM2 and inhibits the ADAM10/17 mediated shedding of TREM2 on the activated microglial cells. Adapted from [123] *Created using the AI-assisted figure generation workflow described in the "Declaration on AI-Assisted Figure Generation".*

Biodistribution analysis corroborated the PET results, demonstrating enhanced cerebral uptake attributable to hTfR-mediated binding. Additionally, elevated bone uptake was observed, which can be attributed to the tracer's affinity for TREM2 and TfR in the bone marrow. This is consistent with the abundant expression of TREM2 in bone osteoclasts, dendritic cells, and other myeloid cells [99-101, 151], and TfR1 receptor expression in bone marrow, in addition to its expression in brain endothelial cells. Furthermore, the TREM2 PET findings were cross-validated using magnetic cell sorting. The *ex vivo* autoradiography analysis of brain sections from hTfR-expressing mice confirmed the *in vivo* TREM2 PET imaging patterns. Immunohistochemistry and *in vitro* autoradiography on human brain samples from Alzheimer's disease patients, utilizing the anti-human TREM2 14D3 antibody, demonstrated the potential translational applicability of the 14D3 tracer for clinical TREM2 imaging.

5.3 Poly-GA

The accumulation of the toxic Poly-GA repeat protein within neuronal cytoplasmic inclusions in C9orf72 patients highlights Poly-GA as a potential biomarker for imaging in ALS/FTD diseases. A novel radiotracer targeting Poly-GA could facilitate the monitoring of disease progression in ALS/FTD patients, thereby providing valuable information on the pathogenesis of C9orf72 associated ALS/FTD.

Developing a tracer for less abundant proteins is challenging. Although TDP-43 is one of the most pathological characteristics of FTD/ALS, its low abundance makes it unsuitable as a biomarker for this purpose. Poly-GA aggregates can be transmitted between cells. This toxic protein is significantly found in the neuronal cytoplasmic and nuclear inclusions of affected patients. [139] This makes it a suitable candidate biomarker for ALS/FTD imaging.

Several anti-GA antibodies targeting Poly-GA aggregates have been developed, including IgG2a, IgG2c, and IgG1 isotypes. A pharmacokinetic study by Orion Pharma in C57BL/6JOLaHsd mice showed that the IgG2a antibody had higher exposure levels in the CNS compared to the other two isotypes. Therefore, the IgG2a antibody was chosen as the carrier molecule for developing the tracer targeting Poly-GA. The developed 1A12 therapeutic antibody (IgG2a isotype) revealed the ability to inhibit intracellular Poly-GA aggregation and block the seeding activity of *C9orf72* brain extracts. Thus, Poly-GA-directed immunotherapy may reduce DPR aggregation and slow disease progression in *C9orf72* ALS/FTD. [148]

For Poly-GA PET imaging, ROSA26 GFP-(GA)175 $^{+/-}$, Camk2a-Cre$^{+/-}$ mice were chosen. The Camk2a-Cre mouse line expresses Poly-GA specifically in excitatory neurons. The highest expression occurs at 4-7 months, making this age range a favorable time for Poly-GA imaging. In contrast, the GA$^{+/-}$ Camk2a-Cre $^{-/-}$ mice do not express Poly-GA and were selected as the control group. Using an immunoassay, Poly-GA expression was quantified in the brain regions and organs of GA-Camk2a mice. In the brain, the cortex and hippocampus revealed the highest expression, while the cerebellum showed the lowest Poly-GA expression compared to other brain regions and was selected as the reference region for the data analysis. Table 8 presents the Poly-GA tracer and mouse models used for *in vivo* tracer evaluation.

Tracer	Mouse line
[^{64}Cu]Cu-NODAGA-mAb1A12	GA$^{+/-}$ Camk2a-Cre $^{+/-}$

[^{64}Cu]Cu-NODAGA-mAb1A12	GA$^{+/-}$ Camk2a-Cre $^{-/-}$

TABLE 8: The transgenic and control mouse lines used for *in vivo* experiments: the tracer was intravenously injected into the tail of the mouse. The PET/CT scan was performed in a time series of 2, 20, and 40 h p.i..

Poly-GA imaging at three-time points revealed that the antibody entered the brain despite the BBB restriction. The highest tracer uptake differences were observed between Tg and controls at 20 h p.i. although overall tracer uptake in the brain was low. Poly-GA imaging at 20 h p.i. was a favorable time point for image acquisition. The schematic representation of the binding of the [^{64}Cu]Cu-NODAGA-mAb1A12 to Poly-GA protein is illustrated in Figure 12. Regional GA-pathology was detected by *in vitro* autoradiography as expressed by a higher $SUVR_{CTX/CBL}$ ratio in Tg mice compared to controls. Organ biodistribution results were in alignment with PET images, confirming higher Poly-GA tracer in the brain of Tg mice than in controls. PET results were verified by *ex vivo* autoradiography on mouse brain sections.

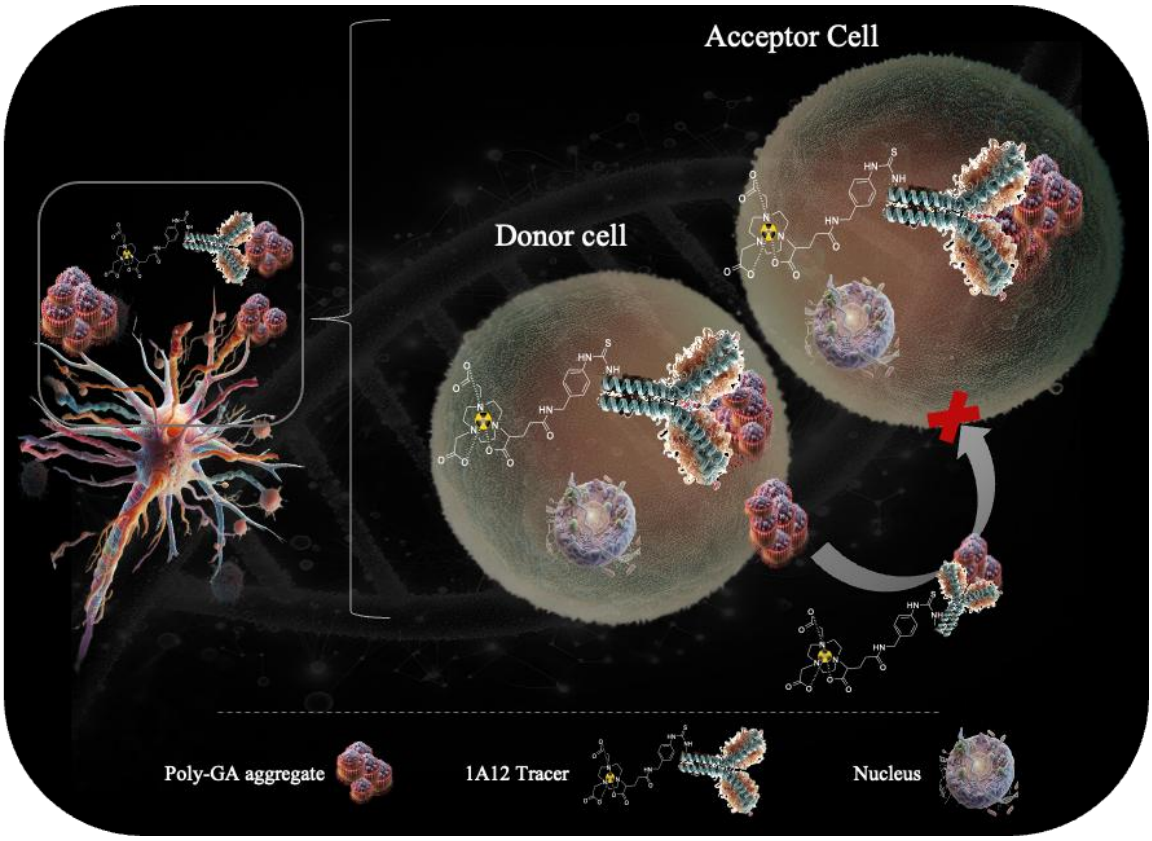

FIGURE 12: Schematic representation of the binding of [^{64}Cu]Cu-NODAGA-mAb1A12 to Poly-GA protein. Toxic Poly-GA proteins can be transmitted to other cells. The [^{64}Cu]Cu-NODAGA-mAb1A12 binds to both cytoplasmic and extracellular Poly-GA aggregates, allowing for the monitoring of Poly-GA levels. Adapted from [142] *Created using the AI-assisted figure generation workflow described in the "Declaration on AI-Assisted Figure Generation".*

6. Conclusion and Outlook

This study aimed to develop novel radioligands targeting TREM2 and Poly-GA. *In vitro* and *in vivo* evaluations were conducted to assess the functionality and specificity of the developed tracers to their respective targets.

The first part of this research presents a significant step towards developing more effective PET imaging agents for visualizing microglial activation in Alzheimer's disease through TREM2 targeting. The previously developed [^{124}I]mAb1729-scFv8D3CL tracer by *Meier et al.* was ineffective for *in vivo* imaging of TREM2 and could only detect it *ex vivo.* The developed [^{64}Cu]Cu-NODAGA-ATV:4D9 presented in this work is the first tracer that enables image TREM2 *in vivo*. [^{64}Cu]Cu-NODAGA-ATV:4D9 showed remarkably higher brain uptake than its non-BBB penetrant counterpart which is attributed to ATV technology. The superior BBB penetration of [^{64}Cu]Cu-NODAGA-ATV:4D9 comparing other studies potentially offers more sensitive and accurate imaging of TREM2.

However, the tracer could not distinguish between TREM2 in CNS and sTREM2. Further investigation is necessary to optimize the TREM2 tracer and address current limitations. The application of TREM2 PET imaging could extend to other NDDs involving microglial activation. In addition, based on these preclinical findings, TREM2 PET imaging shows potential for translation to human research.

The second part of this study introduced a new radiotracer called [^{64}Cu]Cu-NODAGA-mAb1A12 which is specifically designed to target poly-GA protein associated with C9orf72 gen. This study demonstrated that the antibody successfully enters the brain in accordance with previous pharmacokinetics studies.

Despite its limited ability to cross the BBB, the tracer produced high-quality images in preclinical studies. Future research should focus on improving the brain uptake of this tracer across the BBB. Two suggested strategies to overcome this limitation include exploring alternative targeting approaches or engineering antibodies that bind to TfR1. Developing a tracer based on small molecules that bind to the Poly-GA protein could be an alternative approach. The transferrin receptor binding fragment (scFv8D3) is a single-chain variable that binds specifically to mouse TfR1. By attaching the scFv8D3 fragment to the 1A12 antibody, the antibody may overcome the BBB limitation. Although PET/CT imaging allows for regional monitoring of tracer uptake, it cannot differentiate between cytoplasmic and extracellular Poly-GA uptake. Developing a tracer with higher specificity and affinity for cytoplasmic Poly-GA can be achieved by engineering the tracer to target

epitopes unique to cytoplasmic Poly-GA. For example, Cell-penetrating Peptides (CPPs) can facilitate the delivery of tracers directly into the cytoplasm, thereby enhancing specificity for cytoplasmic Poly-GA.

7. References

(1) Rohrer, J. D.; Nicholas, J. M.; Cash, D. M.; van Swieten, J.; Dopper, E.; Jiskoot, L.; van Minkelen, R.; Rombouts, S. A.; Cardoso, M. J.; Clegg, S.; et al. Presymptomatic cognitive and neuroanatomical changes in genetic frontotemporal dementia in the Genetic Frontotemporal dementia Initiative (GENFI) study: a cross-sectional analysis. *Lancet. Neurol.* **2015**, *14* (3), 253-262. DOI: https://doi.org/10.1016/s1474-4422(14)70324-2.

(2) Herholz, K.; Heiss, W. D. Positron emission tomography in clinical neurology. *Mol. Imaging Biol.* **2004**, *6* (4), 239-269. DOI: https://doi.org/10.1016/j.mibio.2004.05.002.

(3) Amor, S.; Peferoen, L. A. N.; Vogel, D. Y. S.; Breur, M.; van der Valk, P.; Baker, D.; van Noort, J. M. Inflammation in neurodegenerative diseases – an update. *Immunology* **2014**, *142* (2), 151-166. DOI: https://doi.org/10.1111/imm.12233 (acccessed 2023/02/13).

(4) Calsolaro, V.; Edison, P. Neuroinflammation in Alzheimer's disease: Current evidence and future directions. *Alzheimer's Dementia* **2016**, *12* (6), 719-732. DOI: https://doi.org/10.1016/j.jalz.2016.02.010.

(5) (DZNE), G. C. f. N. D. *Faktenzentrale: Demenz*. https://www.dzne.de/aktuelles/hintergrund/faktenzentrale/ (accessed October 2024).

(6) (WHO), W. H. O. *Dementia*. March 15, 2023. https://www.who.int/news-room/fact-sheets/detail/dementia (accessed April 2024).

(7) Thyrian, J. R.; Boekholt, M.; Hoffmann, W.; Leiz, M.; Monsees, J.; Schmachtenberg, T.; Schumacher-Schönert, F.; Stentzel, U. The prevalence of people with dementia in Germany-A nationwide analysis at the district level. *Nervenarzt* **2020**, *91* (11), 1058-1061. DOI: https://doi.org/10.1007/s00115-020-00923-y.

(8) Die Häufigkeit von Demenzerkrankungen. https://www.deutsche-alzheimer.de/fileadmin/Alz/pdf/factsheets/infoblatt1_haeufigkeit_demenzerkrankungen_dalzg.pdf (accessed September 2024).

(9) Michalowsky, B.; Kaczynski, A.; Hoffmann, W. Ökonomische und gesellschaftliche Herausforderungen der Demenz in Deutschland – Eine Metaanalyse. *Bundesgesundheitsblatt - Gesundheitsforschung - Gesundheitsschutz* **2019**, *62* (8), 981-992. DOI: https://doi.org/10.1007/s00103-019-02985-z.

(10) (AZ), A. s. D. I. *What is Dementia?* https://www.alzint.org/about/ (accessed April 2024).

(11) Bang, J.; Spina, S.; Miller, B. L. Frontotemporal dementia. *Lancet (London, England)* **2015**, *386* (10004), 1672-1682. DOI: https://doi.org/10.1016/s0140-6736(15)00461-4.

(12) McCauley, M. E., Baloh, R. H. Inflammation in ALS/FTD pathogenesis. *Acta Neuropathol.* **2019**, *137* (5), 715-730. DOI: https://doi.org/10.1007/s00401-018-1933-9.

(13) Edbauer, D.; Haass, C. An amyloid-like cascade hypothesis for C9orf72 ALS/FTD. *Curr. Opin. Neurobiol.* **2016**, *36*, 99-106. DOI: https://doi.org/10.1016/j.conb.2015.10.009.

(14) Neumann, M.; Sampathu, D. M.; Kwong, L. K.; Truax, A. C.; Micsenyi, M. C.; Chou, T. T.; Bruce, J.; Schuck, T.; Grossman, M.; Clark, C. M.; et al. Ubiquitinated TDP-43 in Frontotemporal Lobar Degeneration and Amyotrophic Lateral Sclerosis. *AAAS Sel. Symp.* **2006**, *314* (5796), 130-133. DOI: https://doi.org/10.1126/science.1134108 .

(15) Braak, H.; Del Tredici, K. The pathological process underlying Alzheimer's disease in individuals under thirty. *Acta Neuropathol.* **2011**, *121* (2), 171-181. DOI: https://doi.org/10.1007/s00401-010-0789-4.

(16) Jucker, M.; Walker, L. C. Propagation and spread of pathogenic protein assemblies in neurodegenerative diseases. *Nat. Neurosci.* **2018**, *21* (10), 1341-1349. DOI: https://doi.org/10.1038/s41593-018-0238-6.

(17) Dormann, D.; Haass, C. TDP-43 and FUS: a nuclear affair. *Trends Neurosci.* **2011**, *34* (7), 339-348. DOI: https://doi.org/10.1016/j.tins.2011.05.002.

(18) Arai, T.; Hasegawa, M.; Akiyama, H.; Ikeda, K.; Nonaka, T.; Mori, H.; Mann, D.; Tsuchiya, K.; Yoshida, M.; Hashizume, Y.; et al. TDP-43 is a component of ubiquitin-positive tau-negative inclusions in frontotemporal lobar degeneration and amyotrophic lateral sclerosis. *Biochem. Biophys. Res. Commun.* **2006**, *351* (3), 602-611. DOI: https://doi.org/10.1016/j.bbrc.2006.10.093.

(19) Neumann, M.; Rademakers, R.; Roeber, S.; Baker, M.; Kretzschmar, H. A.; Mackenzie, I. R. A new subtype of frontotemporal lobar degeneration with FUS pathology. *Brain* **2009**, *132* (Pt 11), 2922-2931. DOI: https://doi.org/10.1093/brain/awp214.

(20) Zhang, W.; Xiao, D.; Mao, Q.; Xia, H. Role of neuroinflammation in neurodegeneration development. *Signal Transduct Target Ther.* **2023**, *8* (1), 267. DOI: https://doi.org/10.1038/s41392-023-01486-5.

(21) (EMA), E. M. A. *Leqembi recommended for treatment of early Alzheimer's disease*. 2024. https://www.ema.europa.eu/en/news/leqembi-recommended-treatment-early-alzheimers-disease (accessed December 2024).

(22) Khosravi, B.; LaClair, K. D.; Riemenschneider, H.; Zhou, Q.; Frottin, F.; Mareljic, N.; Czuppa, M.; Farny, D.; Hartmann, H.; Michaelsen, M.; et al. Cell-to-cell transmission of C9orf72 poly-(Gly-Ala) triggers key features of ALS/FTD. *EMBO J.* **2020**, *39* (8), e102811. DOI: https://doi.org/10.15252/embj.2019102811.

(23) Sengupta, U.; Kayed, R. Amyloid β, Tau, and α-Synuclein aggregates in the pathogenesis, prognosis, and therapeutics for neurodegenerative diseases. *Prog. Neurobiol.* **2022**, *214*, 102270. DOI: https://doi.org/10.1016/j.pneurobio.2022.102270.

(24) Jaiswal, M. K. Riluzole and edaravone: A tale of two amyotrophic lateral sclerosis drugs. *Med. Res. Rev.* **2019**, *39* (2), 733-748. DOI: https://doi.org/10.1002/med.21528.

(25) Lamptey, R. N. L.; Chaulagain, B.; Trivedi, R.; Gothwal, A.; Layek, B.; Singh, J. A Review of the Common Neurodegenerative Disorders: Current Therapeutic Approaches and the Potential Role of Nanotherapeutics. *Int. J. Mol. Sci.* **2022**, *23* (3). DOI: https://doi.org/10.3390/ijms23031851.

(26) Kwon, H. S.; Koh, S.-H. Neuroinflammation in neurodegenerative disorders: the roles of microglia and astrocytes. *Transl. Neurodegener.* **2020**, *9* (1), 42. DOI: https://doi.org/10.1186/s40035-020-00221-2.

(27) Giri, P. M.; Banerjee, A.; Ghosal, A.; Layek, B. Neuroinflammation in Neurodegenerative Disorders: Current Knowledge and Therapeutic Implications. *Int. J. Mol. Sci.* **2024**, *25* (7). DOI: https://doi.org/10.3390/ijms25073995.

(28) Butovsky, O.; Weiner, H. L. Microglial signatures and their role in health and disease. *Nat. Rev. Neurosci.* **2018**, *19* (10), 622-635. DOI: https://doi.org/10.1038/s41583-018-0057-5.

(29) Heneka, M. T.; Carson, M. J.; El Khoury, J.; Landreth, G. E.; Brosseron, F.; Feinstein, D. L.; Jacobs, A. H.; Wyss-Coray, T.; Vitorica, J.; Ransohoff, R. M.; et al. Neuroinflammation in Alzheimer's disease. *Lancet Neurol.* **2015**, *14* (4), 388-405. DOI: https://doi.org/10.1016/s1474-4422(15)70016-5.

(30) Lee, H. G.; Lee, J. H.; Flausino, L. E.; Quintana, F. J. Neuroinflammation: An astrocyte perspective. *Sci. Transl. Med.* **2023**, *15* (721), eadi7828. DOI: https://doi.org/10.1126/scitranslmed.adi7828.

(31) Reischl, G. Special Issue "Targets, Tracers and Translation Novel Radiopharmaceuticals Boost Nuclear Medicine". In *Pharmaceuticals*, 2019; Vol. 12, p DOI: https://doi.org/10.3390/ph12030111.

(32) Tai, Y. F.; Piccini, P. Applications of positron emission tomography (PET) in neurology. *J. Neurol. Neurosurg. Psychiatry.* **2004**, *75* (5), 669. DOI: https://doi.org/10.1136/jnnp.2003.028175.

(33) Politis, M.; Piccini, P. Positron emission tomography imaging in neurological disorders. *J. Neurol.* **2012**, *259* (9), 1769-1780. DOI: https://doi.org/10.1007/s00415-012-6428-3.

(34) Alqahtani, F. F. SPECT/CT and PET/CT, related radiopharmaceuticals, and areas of application and comparison. *Saudi Pharm. J.* **2023**, *31* (2), 312-328. DOI: https://doi.org/10.1016/j.jsps.2022.12.013.

(35) Crișan, G.; Moldovean-Cioroianu, N. S.; Timaru, D. G.; Andrieș, G.; Căinap, C.; Chiș, V. Radiopharmaceuticals for PET and SPECT Imaging: A Literature Review over the Last Decade. *Int. J. Mol. Sci.* **2022**, *23* (9). DOI: https://doi.org/10.3390/ijms23095023.

(36) (NIBIB), N. I. o. B. I. a. B. , Nuclear Medicine, July 2016. https://www.nibib.nih.gov/science-education/science-topics/nuclear-medicine (accessed January 2024).

(37) Qaim, S. M.; Bisinger, T.; Hilgers, K.; Nayak, D.; Coenen, H. H. Positron emission intensities in the decay of ^{64}Cu, ^{76}Br and ^{124}I. *Radiochim. Acta.* **2007**, *95*, 67 - 73. DOI: https://doi.org/10.1524/ract.2007.95.2.67.

(38) Karst, U. Nicholas Long and Wing-Tak Wong: The chemistry of molecular imaging. *Anal. Bioanal. Chem.* **2016**, *408* (1), 11-12. DOI: https://doi.org/10.1007/s00216-015-9106-3.

(39) Basu, S.; Kwee, T. C.; Surti, S.; Akin, E. A.; Yoo, D.; Alavi, A. Fundamentals of PET and PET/CT imaging. *Ann. N. Y. Acad. Sci.* **2011**, *1228*, 1-18. DOI: https://doi.org/10.1111/j.1749-6632.2011.06077.x.

(40) Mankoff, D. A.; O'Sullivan, F.; Barlow, W. E.; Krohn, K. A. Molecular imaging research in the outcomes era: measuring outcomes for individualized cancer therapy. *Acad. Radiol.* **2007**, *14* (4), 398-405. DOI: https://doi.org/10.1016/j.acra.2007.01.005.

(41) Sgouros, G. Radiopharmaceutical Therapy. *Health. Phys.* **2019**, *116* (2), 175-178. DOI: https://doi.org/10.1097/hp.0000000000001000.

(42) (INCHEM), I. P. o. C. S. *Biomarkers in Risk Assessment: Validity and Validation.* 2001. https://www.inchem.org/documents/ehc/ehc/ehc222.htm#1.0 (accessed 15 January 2024).

(43) Strimbu, K.; Tavel, J. A. What are biomarkers? *Curr. Opin. HIV AIDS.* **2010**, *5* (6), 463-466. DOI: https://doi.org/10.1097/COH.0b013e32833ed177.

(44) A. J. Atkinson, W. A. C., V. G. DeGruttola, D. L. DeMets, G. J. Downing, D. F. Hoth, J. A. Oates, C. C. Peck, R. T. Schooley, B. A. Spilker, J. Woodcock, S. L. Zeger. Biomarkers and

surrogate endpoints: preferred definitions and conceptual framework. *Clin. Pharmacol. Ther.* **2001**, *69* (3), 89-95. DOI: https://doi.org/10.1067/mcp.2001.113989.

(45) Sehlin, D.; Syvänen, S. Engineered antibodies: new possibilities for brain PET? *EJNMMI.* **2019**, *46* (13), 2848-2858. DOI: https://doi.org/10.1007/s00259-019-04426-0.

(46) Sehlin, D.; Syvänen, S.; Ballanger, B.; Barthel, H.; Bischof, G. N.; Boche, D.; Boecker, H.; Bohn, K. P.; Borghammer, P.; Cross, D.; et al. Engineered antibodies: new possibilities for brain PET? *EJNMMI.* **2019**, *46* (13), 2848-2858. DOI: https://doi.org/10.1007/s00259-019-04426-0.

(47) Hermanson, G. *Bioconjugate Techniques: Third Edition*; 2013. DOI: https://doi.org/10.1016/B978-0-12-382239-0.00005-4.

(48) Fani, M.; Maecke, H. R. Radiopharmaceutical development of radiolabelled peptides. *EJNMMI.* **2012**, *39 Suppl 1*, S11-30. DOI: https://doi.org/10.1007/s00259-011-2001-z.

(49) Wolf, W.; Shani, J. Criteria for the selection of the most desirable radionuclide for radiolabeling monoclonal antibodies. *International Journal of Radiation Applications and Instrumentation. Part B. Nucl. Med. Biol.* **1986**, *13* (4), 319-324. DOI: https://doi.org/10.1016/0883-2897(86)90004-8.

(50) Dash, A.; Chakravarty, R. Radionuclide generators: the prospect of availing PET radiotracers to meet current clinical needs and future research demands. *Am. J. Nucl. Med. Mol. Imaging.* **2019**, *9* (1), 30-66. https://pubmed.ncbi.nlm.nih.gov/30911436/.

(51) Ferguson, S.; Jans, H.-S.; Wuest, M.; Riauka, T.; Wuest, F. Comparison of scandium-44 g with other PET radionuclides in pre-clinical PET phantom imaging. *EJNMMI. Physics* **2019**, *6* (1), 23. DOI: https://doi.org/10.1186/s40658-019-0260-0.

(52) Serdons, K.; Verbruggen, A.; Bormans, G. M. Developing new molecular imaging probes for PET. *Methods* **2009**, *48* (2), 104-111. DOI: https://doi.org/10.1016/j.ymeth.2009.03.010.

(53) Price, T. W.; Greenman, J.; Stasiuk, G. J. Current advances in ligand design for inorganic positron emission tomography tracers ^{68}Ga, ^{64}Cu, ^{89}Zr and ^{44}Sc. *Dalton Trans.* **2016**, *45* (40), 15702-15724. DOI: https://doi.org/10.1039/C5DT04706D.

(54) van der Meulen, N. P.; Hasler, R.; Blanc, A.; Farkas, R.; Benešová, M.; Talip, Z.; Müller, C.; Schibli, R. Implementation of a new separation method to produce qualitatively improved ^{64}Cu. *J. Labelled Compd. Radiopharm.* **2019**, *62* (8), 460-470. DOI: https://doi.org/10.1002/jlcr.3730.

(55) Zhou, Y.; Li, J.; Xu, X.; Zhao, M.; Zhang, B.; Deng, S.; Wu, Y. ^{64}Cu-based Radiopharmaceuticals in Molecular Imaging. *Technol. Cancer. Res. Treat.* **2019**, *18*. DOI: https://doi.org/10.1177/1533033819830758.

(56) (LnHB), L. N. H. B. *Données atomiques et nucléaires*. http://www.lnhb.fr/accueil/donnees-nucleaires/module-lara/ (accessed October 2024).

(57) Carlsson, J.; Stigbrand, T.; Adams, G. P. *Introduction to Radionuclide Therapy*; Springer Netherlands, 2008. DOI: https://doi.org/10.1007/978-1-4020-8696-0_1.

(58) Sharma, S.; Pandey, M. K. Radiometals in Imaging and Therapy: Highlighting Two Decades of Research. *Pharm. (Basel, Switzerland)* **2023**, *16* (10). DOI: https://doi.org/10.3390/ph16101460.

(59) Fiedler, L.; Kellner, M.; Oos, R.; Böning, G.; Ziegler, S.; Bartenstein, P.; Zeidler, R.; Gildehaus, F. J.; Lindner, S. Fully Automated Production and Characterization of ^{64}Cu and Proof-of-Principle Small-Animal PET Imaging Using ^{64}Cu-Labelled CA XII Targeting 6A10 Fab. *Chem. Med. Chem.* **2018**, *13* (12), 1230-1237. DOI: https://doi.org/10.1002/cmdc.201800130.

(60) Gupta, S.; Batra, S.; Jain, M. Antibody labeling with radioiodine and radiometals. *Methods. Mol. Biol.* **2014**, *1141*, 147-157. DOI: https://doi.org/10.1007/978-1-4939-0363-4_9.

(61) Shokeen, M.; Anderson, C. J. Molecular imaging of cancer with copper-64 radiopharmaceuticals and positron emission tomography (PET). *Acc. Chem. Res.* **2009**, *42* (7), 832-841. DOI: https://doi.org/10.1021/ar800255q.

(62) Anderson, C. J.; Ferdani, R. Copper-64 radiopharmaceuticals for PET imaging of cancer: advances in preclinical and clinical research. *Cancer. Biother. Radiopharm.* **2009**, *24* (4), 379-393. DOI: https://doi.org/10.1089/cbr.2009.0674.

(63) Price, E. W.; Orvig, C. Matching chelators to radiometals for radiopharmaceuticals. *Chem. Soc. Rev.* **2014**, *43* (1), 260-290. DOI: https://doi.org/10.1039/C3CS60304K.

(64) Schlein, E.; Rokka, J.; Odell, L. R.; van den Broek, S. L.; Herth, M. M.; Battisti, U. M.; Syvänen, S.; Sehlin, D.; Eriksson, J. Synthesis and evaluation of fluorine-18 labelled tetrazines as pre-targeting imaging agents for PET. *EJNMMI. Radiopharmacy and Chemistry* **2024**, *9* (1), 21. DOI: https://doi.org/10.1186/s41181-024-00250-6.

(65) Kuijpers, W. H. A.; Kaspersen, F. M.; Veeneman, G. H.; Van Boeckel, C. A. A.; Bos, E. S. Specific recognition of antibody-oligonucleotide conjugates by radiolabeled antisense nucleotides: a novel approach for two-step radioimmunotherapy of cancer. *Bioconjugate Chem.* **1993**, *4* (1), 94-102. DOI: https://doi.org/10.1021/bc00019a013.

(66) Zeglis, B. M.; Sevak, K. K.; Reiner, T.; Mohindra, P.; Carlin, S. D.; Zanzonico, P.; Weissleder, R.; Lewis, J. S. A pretargeted PET imaging strategy based on bioorthogonal Diels-Alder click chemistry. *J. Nucl. Med.* **2013**, *54* (8), 1389-1396. DOI: https://doi.org/10.2967/jnumed.112.115840.

(67) Liu, G. A Revisit to the Pretargeting Concept-A Target Conversion. *Front. Pharmacol.* **2018**, *9*, 1476. DOI: https://doi.org/10.3389/fphar.2018.01476.

(68) Blume, T.; Focke, C.; Peters, F.; Deussing, M.; Albert, N. L.; Lindner, S.; Gildehaus, F.-J.; von Ungern-Sternberg, B.; Ozmen, L.; Baumann, K.; et al. Microglial response to increasing amyloid load saturates with aging: a longitudinal dual tracer *in vivo* μPET-study. *J. Neuroinflammation* **2018**, *15* (1), 307. DOI: https://doi.org/10.1186/s12974-018-1347-6.

(69) Meier, S. R.; Sehlin, D.; Hultqvist, G.; Syvänen, S. Pinpointing Brain TREM2 Levels in Two Mouse Models of Alzheimer's Disease. *Mol. Imaging Biol.* **2021**, *23* (5), 665-675. DOI: https://doi.org/10.1007/s11307-021-01591-3.

(70) Wendimu, M. Y.; Hooks, S. B. Microglia Phenotypes in Aging and Neurodegenerative Diseases. *Cells* **2022**, *11* (13). DOI: https://doi.org/10.3390/cells11132091.

(71) Ginhoux, F.; Greter, M.; Leboeuf, M.; Nandi, S.; See, P.; Gokhan, S.; Mehler, M. F.; Conway, S. J.; Ng, L. G.; Stanley, E. R.; et al. Fate mapping analysis reveals that adult microglia derive from primitive macrophages. *AAAS Sel. Symp.* **2010**, *330* (6005), 841-845. DOI: https://doi.org/10.1126/science.1194637.

(72) Beynon, S. B.; Walker, F. R. Microglial activation in the injured and healthy brain: what are we really talking about? Practical and theoretical issues associated with the measurement of changes in microglial morphology. *Neuroscience* **2012**, *225*, 162-171. DOI: https://doi.org/10.1016/j.neuroscience.2012.07.029.

(73) Crews, F.; Newsom, H.; Gerber, M.; Sumners, C.; Chandler, L.; Freund, G. *Molecular Mechanisms of Alcohol Neurotoxicity*; 1993. DOI: https://doi.org/10.1007/978-1-4615-2470-0_11.

(74) Krasemann, S.; Madore, C.; Cialic, R.; Baufeld, C.; Calcagno, N.; El Fatimy, R.; Beckers, L.; O'Loughlin, E.; Xu, Y.; Fanek, Z.; et al. The TREM2-APOE Pathway Drives the Transcriptional Phenotype of Dysfunctional Microglia in Neurodegenerative Diseases. *Immunity* **2017**, *47* (3), 566-581.e569. DOI: https://doi.org/10.1016/j.immuni.2017.08.008.

(75) Keren-Shaul, H.; Spinrad, A.; Weiner, A.; Matcovitch-Natan, O.; Dvir-Szternfeld, R.; Ulland, T. K.; David, E.; Baruch, K.; Lara-Astaiso, D.; Toth, B.; et al. A Unique Microglia Type Associated with Restricting Development of Alzheimer's Disease. *Cell* **2017**, *169* (7), 1276-1290.e1217. DOI: https://doi.org/10.1016/j.cell.2017.05.018.

(76) Schlepckow, K.; Monroe, K. M.; Kleinberger, G.; Cantuti-Castelvetri, L.; Parhizkar, S.; Xia, D.; Willem, M.; Werner, G.; Pettkus, N.; Brunner, B.; et al. Enhancing protective microglial activities with a dual function TREM2 antibody to the stalk region. *EMBO Mol. Med.* **2020**, *12* (4), e11227. DOI: https://doi.org/10.15252/emmm.201911227.

(77) Chiu, I. M.; Morimoto, E. T.; Goodarzi, H.; Liao, J. T.; O'Keeffe, S.; Phatnani, H. P.; Muratet, M.; Carroll, M. C.; Levy, S.; Tavazoie, S.; et al. A neurodegeneration-specific gene-expression signature of acutely isolated microglia from an amyotrophic lateral sclerosis mouse model. *Cell Rep.* **2013**, *4* (2), 385-401. DOI: https://doi.org/10.1016/j.celrep.2013.06.018.

(78) Kulkarni, B.; Kumar, D.; Cruz-Martins, N.; Sellamuthu, S. Role of TREM2 in Alzheimer's Disease: A Long Road Ahead. *Mol. Neurobiol.* **2021**, *58* (10), 5239-5252. DOI: https://doi.org/10.1007/s12035-021-02477-9.

(79) Sierra, A.; de Castro, F.; Del Río-Hortega, J.; Rafael Iglesias-Rozas, J.; Garrosa, M.; Kettenmann, H. The "Big-Bang" for modern glial biology: Translation and comments on Pío del Río-Hortega 1919 series of papers on microglia. *Glia* **2016**, *64* (11), 1801-1840. DOI: https://doi.org/10.1002/glia.23046.

(80) Savage, J. C.; Picard, K.; González-Ibáñez, F.; Tremblay, M. A Brief History of Microglial Ultrastructure: Distinctive Features, Phenotypes, and Functions Discovered Over the Past 60 Years by Electron Microscopy. *Front. Immunol.* **2018**, *9*, 803. DOI: https://doi.org/10.3389/fimmu.2018.00803.

(81) Antignano, I.; Liu, Y.; Offermann, N.; Capasso, M. Aging microglia. *Cell. Mol. Life. Sci.* **2023**, *80* (5), 126. DOI: https://doi.org/10.1007/s00018-023-04775-y.

(82) Nimmerjahn, A.; Kirchhoff, F.; Helmchen, F. Resting microglial cells are highly dynamic surveillants of brain parenchyma *in vivo*. *AAAS Sel. Symp.* **2005**, *308* (5726), 1314-1318. DOI: https://doi.org/10.1126/science.1110647.

(83) Kaur, C.; Ling, E. A.; Wong, W. C. Transformation of amoeboid microglial cells into microglia in the corpus callosum of the postnatal rat brain. An electron microscopical study. *Arch. Histol. Jpn.* **1985**, *48* (1), 17-25. DOI: https://doi.org/10.1679/aohc.48.17.

(84) Kreutzberg, G. W. Microglia: a sensor for pathological events in the CNS. *Trends. Neurosci.* **1996**, *19* (8), 312-318. DOI: https://doi.org/10.1016/0166-2236(96)10049-7.

(85) Raivich, G.; Bohatschek, M.; Kloss, C. U.; Werner, A.; Jones, L. L.; Kreutzberg, G. W. Neuroglial activation repertoire in the injured brain: graded response, molecular mechanisms and cues to physiological function. *Brain. Res. Rev.* **1999**, *30* (1), 77-105. DOI: https://doi.org/10.1016/s0165-0173(99)00007-7.

(86) Morenas-Rodríguez, E.; Li, Y.; Nuscher, B.; Franzmeier, N.; Xiong, C.; Suárez-Calvet, M.; Fagan, A. M.; Schultz, S.; Gordon, B. A.; Benzinger, T. L. S.; et al. Soluble TREM2 in CSF and its association with other biomarkers and cognition in autosomal-dominant Alzheimer's disease: a

longitudinal observational study. *Lancet. Neurol.* **2022**, *21* (4), 329-341. DOI: https://doi.org/10.1016/s1474-4422(22)00027-8.

(87) Werry, E. L.; Bright, F. M.; Piguet, O.; Ittner, L. M.; Halliday, G. M.; Hodges, J. R.; Kiernan, M. C.; Loy, C. T.; Kril, J. J.; Kassiou, M. Recent Developments in TSPO PET Imaging as A Biomarker of Neuroinflammation in Neurodegenerative Disorders. *Int. J. Mol. Sci.* **2019**, *20* (13), 3161. DOI: https://doi.org/doi:10.3390/ijms20133161.

(88) Brendel, M.; Probst, F.; Jaworska, A.; Overhoff, F.; Korzhova, V.; Albert, N. L.; Beck, R.; Lindner, S.; Gildehaus, F.-J.; Baumann, K.; et al. Glial Activation and Glucose Metabolism in a Transgenic Amyloid Mouse Model: A Triple-Tracer PET Study. *J. Nucl. Med.* **2016**, *57* (6), 954-960. DOI: https://doi.org/10.2967/jnumed.115.167858.

(89) Chen, M. K.; Guilarte, T. R. Translocator protein 18 kDa (TSPO): molecular sensor of brain injury and repair. *Pharmacol. Ther.* **2008**, *118* (1), 1-17. DOI: https://doi.org/10.1016/j.pharmthera.2007.12.004.

(90) Benavides, J.; Fage, D.; Carter, C.; Scatton, B. Peripheral type benzodiazepine binding sites are a sensitive indirect index of neuronal damage. *Brain. Res. Rev.* **1987**, *421* (1-2), 167-172. DOI: https://doi.org/10.1016/0006-8993(87)91287-x.

(91) Chauveau, F.; Boutin, H.; Van Camp, N.; Dollé, F.; Tavitian, B. Nuclear imaging of neuroinflammation: a comprehensive review of [^{11}C]PK11195 challengers. *EJNMMI.* **2008**, *35* (12), 2304-2319. DOI: https://doi.org/10.1007/s00259-008-0908-9.

(92) Boutin, H.; Murray, K.; Pradillo, J.; Maroy, R.; Smigova, A.; Gerhard, A.; Jones, P. A.; Trigg, W. [^{18}F]GE-180: a novel TSPO radiotracer compared to [^{11}C]-R-PK11195 in a preclinical model of stroke. *EJNMMI.* **2015**, *42* (3), 503-511. DOI: https://doi.org/10.1007/s00259-014-2939-8.

(93) Wadsworth, H.; Jones, P. A.; Chau, W.-F.; Durrant, C.; Fouladi, N.; Passmore, J.; O'Shea, D.; Wynn, D.; Morisson-Iveson, V.; Ewan, A.; et al. [^{18}F]GE-180: A novel fluorine-18 labelled PET tracer for imaging Translocator protein 18kDa (TSPO). *Bioorg. Med. Chem. Lett.* **2012**, *22* (3), 1308-1313. DOI: https://doi.org/10.1016/j.bmcl.2011.12.084.

(94) Lee, J. W.; Nam, H.; Yu, S. W. Systematic Analysis of Translocator Protein 18kDa (TSPO) Ligands on Toll-like Receptors-mediated Pro-inflammatory Responses in Microglia and Astrocytes. *Exp. Neurobiol.* **2016**, *25* (5), 262-268. DOI: https://doi.org/10.5607/en.2016.25.5.262.

(95) Rojas, C.; Stathis, M.; Coughlin, J. M.; Pomper, M.; Slusher, B. S. The Low-Affinity Binding of Second Generation Radiotracers Targeting TSPO is Associated with a Unique Allosteric Binding Site. J. Neuroimmune. Pharmacol. **2018**, *13* (1), 1-5. DOI: https://doi.org/10.1007/s11481-017-9765-2.

(96) Parhizkar, S.; Arzberger, T.; Brendel, M.; Kleinberger, G.; Deussing, M.; Focke, C.; Nuscher, B.; Xiong, M.; Ghasemigharagoz, A.; Katzmarski, N.; et al. Loss of TREM2 function increases amyloid seeding but reduces plaque-associated ApoE. *Nat. Neurosci.* **2019**, *22* (2), 191-204. DOI: https://doi.org/10.1038/s41593-018-0296-9.

(97) Schlepckow, K.; Kleinberger, G.; Fukumori, A.; Feederle, R.; Lichtenthaler, S. F.; Steiner, H.; Haass, C. An Alzheimer-associated TREM2 variant occurs at the ADAM cleavage site and affects shedding and phagocytic function. *EMBO Mol. Med.* **2017**, *9* (10), 1356-1365. DOI: https://doi.org/10.15252/emmm.201707672.

(98) Poliani, P. L.; Wang, Y.; Fontana, E.; Robinette, M. L.; Yamanishi, Y.; Gilfillan, S.; Colonna, M. TREM2 sustains microglial expansion during aging and response to demyelination. *J. Clin. Invest.* **2015**, *125*, Report. DOI: https://doi.org/10.1172/JCI77983.

(99) Bouchon, A.; Hernández-Munain, C.; Cella, M.; Colonna, M. A Dap12-Mediated Pathway Regulates Expression of Cc Chemokine Receptor 7 and Maturation of Human Dendritic Cells. *J. Exp. Med.* **2001**, *194* (8), 1111-1122. DOI: https://doi.org/10.1084/jem.194.8.1111.

(100) Cella , M.; Buonsanti , C.; Strader , C.; Kondo , T.; Salmaggi , A.; Colonna , M. Impaired Differentiation of Osteoclasts in TREM-2–deficient Individuals. *J. Exp. Med.* **2003**, *198* (4), 645-651. DOI: https://doi.org/10.1084/jem.20022220.

(101) Paloneva , J.; Mandelin , J.; Kiialainen , A.; Böhling , T.; Prudlo , J.; Hakola , P.; Haltia , M.; Konttinen , Y. T.; Peltonen , L. DAP12/TREM2 Deficiency Results in Impaired Osteoclast Differentiation and Osteoporotic Features. *J. Exp. Med.* **2003**, *198* (4), 669-675. DOI: https://doi.org/10.1084/jem.20030027.

(102) Colonna, M.; Wang, Y. TREM2 variants: new keys to decipher Alzheimer disease pathogenesis. *Nat. Rev. Neurosci.* **2016**, *17* (4), 201-207. DOI: https://doi.org/10.1038/nrn.2016.7.

(103) Bouchon, A.; Dietrich, J.; Colonna, M. Cutting edge: inflammatory responses can be triggered by TREM-1, a novel receptor expressed on neutrophils and monocytes. *J. Immunol.* **2000**, *164* (10), 4991-4995. DOI: https://doi.org/10.4049/jimmunol.164.10.4991.

(104) Ulrich, J. D.; Ulland, T. K.; Colonna, M.; Holtzman, D. M. Elucidating the Role of TREM2 in Alzheimer's Disease. *Neuron* **2017**, *94* (2), 237-248. DOI: https://doi.org/10.1016/j.neuron.2017.02.042.

(105) Mazaheri, F.; Snaidero, N.; Kleinberger, G.; Madore, C.; Daria, A.; Werner, G.; Krasemann, S.; Capell, A.; Trümbach, D.; Wurst, W.; et al. TREM2 deficiency impairs chemotaxis and microglial responses to neuronal injury. *EMBO Rep.* **2017**, *18* (7), 1186-1198. DOI: https://doi.org/10.15252/embr.201743922.

(106) Nugent, A. A.; Lin, K.; van Lengerich, B.; Lianoglou, S.; Przybyla, L.; Davis, S. S.; Llapashtica, C.; Wang, J.; Kim, D. J.; Xia, D.; et al. TREM2 Regulates Microglial Cholesterol Metabolism upon Chronic Phagocytic Challenge. *Neuron* **2020**, *105* (5), 837-854.e839. DOI: https://doi.org/10.1016/j.neuron.2019.12.007.

(107) Kleinberger, G.; Yamanishi, Y.; Suárez-Calvet, M.; Czirr, E.; Lohmann, E.; Cuyvers, E.; Struyfs, H.; Pettkus, N.; Wenninger-Weinzierl, A.; Mazaheri, F.; et al. TREM2 mutations implicated in neurodegeneration impair cell surface transport and phagocytosis. *Sci. Transl. Med.* **2014**, *6* (243), 243ra286. DOI: https://doi.org/10.1126/scitranslmed.3009093.

(108) Meyer-Luehmann, M.; Spires-Jones, T. L.; Prada, C.; Garcia-Alloza, M.; de Calignon, A.; Rozkalne, A.; Koenigsknecht-Talboo, J.; Holtzman, D. M.; Bacskai, B. J.; Hyman, B. T. Rapid appearance and local toxicity of amyloid-beta plaques in a mouse model of Alzheimer's disease. *Nature* **2008**, *451* (7179), 720-724. DOI: https://doi.org/10.1038/nature06616.

(109) Serrano-Pozo, A.; Muzikansky, A.; Gómez-Isla, T.; Growdon, J. H.; Betensky, R. A.; Frosch, M. P.; Hyman, B. T. Differential relationships of reactive astrocytes and microglia to fibrillar amyloid deposits in Alzheimer disease. *J. Neuropathol. Exp. Neurol.* **2013**, *72* (6), 462-471. DOI: https://doi.org/10.1097/NEN.0b013e3182933788.

(110) Guerreiro, R.; Wojtas, A.; Bras, J.; Carrasquillo, M.; Rogaeva, E.; Majounie, E.; Cruchaga, C.; Sassi, C.; Kauwe, J. S. K.; Younkin, S.; et al. TREM2 Variants in Alzheimer's Disease. *N. Engl. J. Med.* **2012**, *368* (2), 117-127. DOI: https://doi.org/10.1056/NEJMoa1211851.

(111) Jonsson, T.; Stefansson, H.; Steinberg, S.; Jonsdottir, I.; Jonsson, P. V.; Snaedal, J.; Bjornsson, S.; Huttenlocher, J.; Levey, A. I.; Lah, J. J.; et al. Variant of TREM2 Associated with the Risk of Alzheimer's Disease. *N. Engl. J. Med.* **2012**, *368* (2), 107-116. DOI: https://doi.org/10.1056/NEJMoa1211103.

(112) Klünemann, H. H.; Ridha, B. H.; Magy, L.; Wherrett, J. R.; Hemelsoet, D. M.; Keen, R. W.; De Bleecker, J. L.; Rossor, M. N.; Marienhagen, J.; Klein, H. E.; et al. The genetic causes of basal ganglia calcification, dementia, and bone cysts: DAP12 and TREM2. *Morphol. Biochem. Correl. Neural Act.* **2005**, *64* (9), 1502-1507. DOI: https://doi.org/10.1212/01.Wnl.0000160304.00003.Ca.

(113) Guerreiro, R. J.; Lohmann, E.; Brás, J. M.; Gibbs, J. R.; Rohrer, J. D.; Gurunlian, N.; Dursun, B.; Bilgic, B.; Hanagasi, H.; Gurvit, H.; et al. Using exome sequencing to reveal mutations in TREM2 presenting as a frontotemporal dementia-like syndrome without bone involvement. *JAMA Neurol.* **2013**, *70* (1), 78-84. DOI: https://doi.org/10.1001/jamaneurol.2013.579.

(114) Borroni, B.; Ferrari, F.; Galimberti, D.; Nacmias, B.; Barone, C.; Bagnoli, S.; Fenoglio, C.; Piaceri, I.; Archetti, S.; Bonvicini, C.; et al. Heterozygous TREM2 mutations in frontotemporal dementia. *Neurobiol. Aging* **2014**, *35* (4), 934.e937-910. DOI: https://doi.org/10.1016/j.neurobiolaging.2013.09.017.

(115) Cady, J.; Koval, E. D.; Benitez, B. A.; Zaidman, C.; Jockel-Balsarotti, J.; Allred, P.; Baloh, R. H.; Ravits, J.; Simpson, E.; Appel, S. H.; et al. TREM2 variant p.R47H as a risk factor for sporadic amyotrophic lateral sclerosis. *JAMA Neurol.* **2014**, *71* (4), 449-453. DOI: https://doi.org/10.1001/jamaneurol.2013.6237.

(116) Cuyvers, E.; Bettens, K.; Philtjens, S.; Van Langenhove, T.; Gijselinck, I.; van der Zee, J.; Engelborghs, S.; Vandenbulcke, M.; Van Dongen, J.; Geerts, N.; et al. Investigating the role of rare heterozygous TREM2 variants in Alzheimer's disease and frontotemporal dementia. *Neurobiol. Aging* **2014**, *35* (3), 726.e711-729. DOI: https://doi.org/10.1016/j.neurobiolaging.2013.09.009.

(117) Rayaprolu, S.; Mullen, B.; Baker, M.; Lynch, T.; Finger, E.; Seeley, W. W.; Hatanpaa, K. J.; Lomen-Hoerth, C.; Kertesz, A.; Bigio, E. H.; et al. TREM2 in neurodegeneration: evidence for association of the p.R47H variant with frontotemporal dementia and Parkinson's disease. *Mol. Neurodegener.* **2013**, *8*, 19. DOI: https://doi.org/10.1186/1750-1326-8-19.

(118) Brendel, M.; Kleinberger, G.; Probst, F.; Jaworska, A.; Overhoff, F.; Blume, T.; Albert, N. L.; Carlsen, J.; Lindner, S.; Gildehaus, F. J.; et al. Increase of TREM2 during Aging of an Alzheimer's Disease Mouse Model Is Paralleled by Microglial Activation and Amyloidosis. *Frontiers in aging neuroscience* **2017**, *9*, 8. DOI: https://doi.org/10.3389/fnagi.2017.00008.

(119) Park, J. S.; Ji, I. J.; An, H. J.; Kang, M. J.; Kang, S. W.; Kim, D. H.; Yoon, S. Y. Disease-Associated Mutations of TREM2 Alter the Processing of N-Linked Oligosaccharides in the Golgi Apparatus. *Traffic* **2015**, *16* (5), 510-518. DOI: https://doi.org/10.1111/tra.12264.

(120) Jin, S. C.; Benitez, B. A.; Karch, C. M.; Cooper, B.; Skorupa, T.; Carrell, D.; Norton, J. B.; Hsu, S.; Harari, O.; Cai, Y.; et al. Coding variants in TREM2 increase risk for Alzheimer's disease. *Hum. Mol. Genet.* **2014**, *23* (21), 5838-5846. DOI: https://doi.org/10.1093/hmg/ddu277.

(121) Jin, S. C.; Carrasquillo, M. M.; Benitez, B. A.; Skorupa, T.; Carrell, D.; Patel, D.; Lincoln, S.; Krishnan, S.; Kachadoorian, M.; Reitz, C.; et al. TREM2 is associated with increased risk for Alzheimer's disease in African Americans. *Mol. Neurodegener.* **2015**, *10*, 19. DOI: https://doi.org/10.1186/s13024-015-0016-9.

(122) Wang, Y.; Cella, M.; Mallinson, K.; Ulrich, J. D.; Young, K. L.; Robinette, M. L.; Gilfillan, S.; Krishnan, G. M.; Sudhakar, S.; Zinselmeyer, B. H.; et al. TREM2 lipid sensing sustains the microglial response in an Alzheimer's disease model. *Cell* **2015**, *160* (6), 1061-1071. DOI: https://doi.org/10.1016/j.cell.2015.01.049.

(123) Schlepckow, K.; Morenas-Rodríguez, E.; Hong, S.; Haass, C. Stimulation of TREM2 with agonistic antibodies-an emerging therapeutic option for Alzheimer's disease. *Lancet. Neurol.* **2023**, *22* (11), 1048-1060. DOI: https://doi.org/10.1016/s1474-4422(23)00247-8.

(124) Price, B. R.; Sudduth, T. L.; Weekman, E. M.; Johnson, S.; Hawthorne, D.; Woolums, A.; Wilcock, D. M. Therapeutic Trem2 activation ameliorates amyloid-beta deposition and improves cognition in the 5XFAD model of amyloid deposition. *J. Neuroinflammation* **2020**, *17* (1), 238. DOI: https://doi.org/10.1186/s12974-020-01915-0.

(125) Shi, D.; Si, Z.; Xu, Z.; Cheng, Y.; Lin, Q.; Fu, Z.; Fu, W.; Yang, T.; Shi, H.; Cheng, D. Synthesis and Evaluation of ^{68}Ga-NOTA-COG1410 Targeting to TREM2 of TAMs as a Specific PET Probe for Digestive Tumor Diagnosis. *Anal. Chem.* **2022**, *94* (9), 3819-3830. DOI: https://doi.org/10.1021/acs.analchem.1c04701.

(126) Shi, D.; Xu, Z.; Cheng, Y.; Lin, Q.; Si, Z.; Fu, W.; Yang, T.; Shi, H.; Cheng, D. ^{124}I-Labeled Immuno-PET Targeting hTREM2 for the Diagnosis of Gastric Carcinoma. *Mol. Pharmaceutics* **2023**, *20* (4), 2235-2244. DOI: https://doi.org/10.1021/acs.molpharmaceut.3c00041.

(127) Shojaei, M.; Schaefer, R.; Schlepckow, K.; Kunze, L. H.; Struebing, F. L.; Brunner, B.; Willem, M.; Bartos, L. M.; Feiten, A.; Palumbo, G.; et al. PET imaging of microglia in Alzheimer's disease using copper-64 labeled TREM2 antibodies. *Theranostics* **2024**, *14* (16), 6319-6336. DOI: https://doi.org/10.7150/thno.97149.

(128) Varnum, M. M.; Ikezu, T. The Classification of Microglial Activation Phenotypes on Neurodegeneration and Regeneration in Alzheimer's Disease Brain. *Arch. Immunol. Ther. Exp.* **2012**, *60* (4), 251-266. DOI: https://doi.org/10.1007/s00005-012-0181-2.

(129) van Lengerich, B.; Zhan, L.; Xia, D.; Chan, D.; Joy, D.; Park, J. I.; Tatarakis, D.; Calvert, M.; Hummel, S.; Lianoglou, S.; et al. A TREM2-activating antibody with a blood–brain barrier transport vehicle enhances microglial metabolism in Alzheimer's disease models. *Nat. Neurosci.* **2023**. DOI: https://doi.org/10.1038/s41593-022-01240-0.

(130) Kariolis, M. S.; Wells, R. C.; Getz, J. A.; Kwan, W.; Mahon, C. S.; Tong, R.; Kim, D. J.; Srivastava, A.; Bedard, C.; Henne, K. R.; et al. Brain delivery of therapeutic proteins using an Fc fragment blood-brain barrier transport vehicle in mice and monkeys. *Sci. Transl. Med.* **2020**, *12* (545). DOI: https://doi.org/10.1126/scitranslmed.aay1359.

(131) Ringholz, G. M.; Appel, S. H.; Bradshaw, M.; Cooke, N. A.; Mosnik, D. M.; Schulz, P. E. Prevalence and patterns of cognitive impairment in sporadic ALS. *Morphol. Biochem. Correl. Neural Act.* **2005**, *65* (4), 586-590. DOI: https://doi.org/10.1212/01.wnl.0000172911.39167.b6.

(132) Ling, S. C.; Polymenidou, M.; Cleveland, D. W. Converging mechanisms in ALS and FTD: disrupted RNA and protein homeostasis. *Neuron* **2013**, *79* (3), 416-438. DOI: https://doi.org/10.1016/j.neuron.2013.07.033.

(133) Puppala, G.; Gorthi, S.; Chandran, V.; Gundabolu, G. Frontotemporal Dementia - Current Concepts. *Neurol. India* **2021**, *69*, 1144, Disease/Disorder overview. DOI: https://doi.org/10.4103/0028-3886.329593.

(134) Rohrer, J. D.; Nicholas, J. M.; Cash, D. M.; van Swieten, J.; Dopper, E.; Jiskoot, L.; van Minkelen, R.; Rombouts, S. A.; Cardoso, M. J.; Clegg, S.; et al. Presymptomatic cognitive and

neuroanatomical changes in genetic frontotemporal dementia in the Genetic Frontotemporal dementia Initiative (GENFI) study: a cross-sectional analysis. *Lancet. Neurol.* **2015**, *14* (3), 253-262. DOI: https://doi.org/10.1016/S1474-4422(14)70324-2.

(135) Mori, K.; Arzberger, T.; Grässer, F. A.; Gijselinck, I.; May, S.; Rentzsch, K.; Weng, S.-M.; Schludi, M. H.; van der Zee, J.; Cruts, M.; et al. Bidirectional transcripts of the expanded C9orf72 hexanucleotide repeat are translated into aggregating dipeptide repeat proteins. *Acta Neuropathol.* **2013**, *126* (6), 881-893. DOI: https://doi.org/10.1007/s00401-013-1189-3.

(136) Lomen-Hoerth, C.; Anderson, T.; Miller, B. The overlap of amyotrophic lateral sclerosis and frontotemporal dementia. *Morphol. Biochem. Correl. Neural Act.* **2002**, *59* (7), 1077. DOI: https://doi.org/10.1212/WNL.59.7.1077.

(137) DeJesus-Hernandez, M.; Mackenzie, I. R.; Boeve, B. F.; Boxer, A. L.; Baker, M.; Rutherford, N. J.; Nicholson, A. M.; Finch, N. A.; Flynn, H.; Adamson, J.; et al. Expanded GGGGCC hexanucleotide repeat in noncoding region of C9ORF72 causes chromosome 9p-linked FTD and ALS. *Neuron* **2011**, *72* (2), 245-256. DOI: https://doi.org/10.1016/j.neuron.2011.09.011.

(138) Renton, A. E.; Majounie, E.; Waite, A.; Simón-Sánchez, J.; Rollinson, S.; Gibbs, J. R.; Schymick, J. C.; Laaksovirta, H.; van Swieten, J. C.; Myllykangas, L.; et al. A hexanucleotide repeat expansion in C9ORF72 is the cause of chromosome 9p21-linked ALS-FTD. *Neuron* **2011**, *72* (2), 257-268. DOI: https://doi.org/10.1016/j.neuron.2011.09.010.

(139) Lee, Y.-B.; Baskaran, P.; Gomez-Deza, J.; Chen, H.-J.; Nishimura, A. L.; Smith, B. N.; Troakes, C.; Adachi, Y.; Stepto, A.; Petrucelli, L.; et al. C9orf72 poly GA RAN-translated protein plays a key role in amyotrophic lateral sclerosis via aggregation and toxicity. *Hum. Mol. Genet.* **2017**, *26* (24), 4765-4777. DOI: https://doi.org/10.1093/hmg/ddx350.

(140) Ash, Peter E. A.; Bieniek, Kevin F.; Gendron, Tania F.; Caulfield, T.; Lin, W.-L.; DeJesus-Hernandez, M.; van Blitterswijk, Marka M.; Jansen-West, K.; Paul, Joseph W.; Rademakers, R.; et al. Unconventional Translation of C9ORF72 GGGGCC Expansion Generates Insoluble Polypeptides Specific to c9FTD/ALS. *Neuron* **2013**, *77* (4), 639-646. DOI: https://doi.org/10.1016/j.neuron.2013.02.004.

(141) Khosravi, B.; Hartmann, H.; May, S.; Möhl, C.; Ederle, H.; Michaelsen, M.; Schludi, M. H.; Dormann, D.; Edbauer, D. Cytoplasmic poly-GA aggregates impair nuclear import of TDP-43 in C9orf72 ALS/FTLD. *Hum. Mol. Genet.* **2017**, *26* (4), 790-800. DOI: https://doi.org/10.1093/hmg/ddw432.

(142) Zhou, Q.; Lehmer, C.; Michaelsen, M.; Mori, K.; Alterauge, D.; Baumjohann, D.; Schludi, M. H.; Greiling, J.; Farny, D.; Flatley, A.; et al. Antibodies inhibit transmission and aggregation of C9orf72 poly-GA dipeptide repeat proteins. *EMBO Mol. Med.* **2017**, *9* (5), 687-702. DOI: https://doi.org/10.15252/emmm.201607054.

(143) Westergard, T.; Jensen, Brigid K.; Wen, X.; Cai, J.; Kropf, E.; Iacovitti, L.; Pasinelli, P.; Trotti, D. Cell-to-Cell Transmission of Dipeptide Repeat Proteins Linked to C9orf72-ALS/FTD. *Cell Rep.* **2016**, *17* (3), 645-652. DOI: https://doi.org/10.1016/j.celrep.2016.09.032.

(144) Nonaka, T.; Masuda-Suzukake, M.; Hosokawa, M.; Shimozawa, A.; Hirai, S.; Okado, H.; Hasegawa, M. C9ORF72 dipeptide repeat poly-GA inclusions promote intracellular aggregation of phosphorylated TDP-43. *Hum. Mol. Genet.* **2018**, *27* (15), 2658-2670. DOI: https://doi.org/10.1093/hmg/ddy174.

(145) Mann, D. M.; Rollinson, S.; Robinson, A.; Bennion Callister, J.; Thompson, J. C.; Snowden, J. S.; Gendron, T.; Petrucelli, L.; Masuda-Suzukake, M.; Hasegawa, M.; et al. Dipeptide repeat

proteins are present in the p62 positive inclusions in patients with frontotemporal lobar degeneration and motor neurone disease associated with expansions in C9ORF72. *Acta Neuropathol. Commun.* **2013**, *1*, 68. DOI: https://doi.org/10.1186/2051-5960-1-68.

(146) Carroll, J.; McCann, H.; Halliday, G. M.; Kwok, J. B.; Dobson-Stone, C.; Shepherd, C. E. Poly-GA immunohistochemistry is a reliable tool for detecting C9orf72 hexanucleotide repeat expansions. *Brain Pathol.* **2024**, *34* (5), e13216. DOI: https://doi.org/10.1111/bpa.13216.

(147) Mackenzie, I. R.; Arzberger, T.; Kremmer, E.; Troost, D.; Lorenzl, S.; Mori, K.; Weng, S.-M.; Haass, C.; Kretzschmar, H. A.; Edbauer, D.; et al. Dipeptide repeat protein pathology in C9ORF72 mutation cases: clinico-pathological correlations. *Acta Neuropathol.* **2013**, *126* (6), 859-879. DOI: https://doi.org/10.1007/s00401-013-1181-y.

(148) Zhou, Q.; Mareljic, N.; Michaelsen, M.; Parhizkar, S.; Heindl, S.; Nuscher, B.; Farny, D.; Czuppa, M.; Schludi, C.; Graf, A.; et al. Active poly-GA vaccination prevents microglia activation and motor deficits in a C9orf72 mouse model. *EMBO Mol. Med.* **2020**, *12* (2), e10919. DOI: https://doi.org/10.15252/emmm.201910919.

(149) Chertoff, M.; Shrivastava, K.; Gonzalez, B.; Acarin, L.; Giménez-Llort, L. Differential modulation of TREM2 protein during postnatal brain development in mice. *PloS one* **2013**, *8* (8), e72083. DOI: https://doi.org/10.1371/journal.pone.0072083.

(150) Forabosco, P.; Ramasamy, A.; Trabzuni, D.; Walker, R.; Smith, C.; Bras, J.; Levine, A. P.; Hardy, J.; Pocock, J. M.; Guerreiro, R.; et al. Insights into TREM2 biology by network analysis of human brain gene expression data. *Neurobiol. Aging* **2013**, *34* (12), 2699-2714. DOI: https://doi.org/10.1016/j.neurobiolaging.2013.05.001.

(151) Cantoni, C.; Bollman, B.; Licastro, D.; Xie, M.; Mikesell, R.; Schmidt, R.; Yuede, C. M.; Galimberti, D.; Olivecrona, G.; Klein, R. S.; et al. TREM2 regulates microglial cell activation in response to demyelination *in vivo*. *Acta Neuropathol.* **2015**, *129* (3), 429-447. DOI: https://doi.org/10.1007/s00401-015-1388-1.

8. Publication I

ACS Pharmacology & Translational Science

pubs.acs.org/ptsci

Article

Development and Preclinical Evaluation of a Copper-64-Labeled Antibody Targeting Glycine-Alanine Dipeptides for PET Imaging of C9orf72-Associated Amyotrophic Lateral Sclerosis/Frontotemporal Dementia

Monireh Shojaei, Qihui Zhou, Giovanna Palumbo, Rebecca Schaefer, Janne Kaskinoro, Pirjo Vehmaan-Kreula, Peter Bartenstein, Matthias Brendel, Dieter Edbauer, and Simon Lindner*

Cite This: https://doi.org/10.1021/acsptsci.4c00037

Read Online

ACCESS | Metrics & More | Article Recommendations | Supporting Information

ABSTRACT: Aggregating poly(glycine-alanine) (poly-GA) is derived from the unconventional translation of the pathogenic intronic hexanucleotide repeat expansion in the *C9orf72* gene, which is the most common genetic cause of frontotemporal dementia (FTD) and amyotrophic lateral sclerosis (ALS). Poly-GA accumulates predominantly in neuronal cytoplasmic inclusions unique to *C9orf72* ALS/FTD patients. Poly-GA is, therefore, a promising target for PET/CT imaging of FTD/ALS to monitor disease progression and therapeutic interventions. A novel ^{64}Cu-labeled anti-GA antibody (mAb1A12) targeting the poly-GA protein was developed and evaluated in a transgenic mouse model. It was obtained with high radiochemical purity (RCP), radiochemical yield (RCY), and specific activity, and showed high stability *in vitro* and *ex vivo* and specifically bound to poly-GA. The affinity of NODAGA-mAb1A12 for poly-GA was not affected by this modification. [^{64}Cu]Cu-NODAGA-mAb1A12 was injected into transgenic mice expressing GFP-$(GA)_{175}$ in excitatory neurons driven by Camk2a-Cre and in control littermates. PET/CT imaging was performed at 2, 20, and 40 h post-injection (p.i.) and revealed a higher accumulation in the cortex in transgenic mice than in wild-type mice, as reflected by higher standardized uptake value ratios (SUVR) using the cerebellum as the reference region. The organs were isolated for biodistribution and *ex vivo* autoradiography. Autoradiography revealed a higher cortex-to-cerebellum ratio in the transgenic mice than in the controls. Results from autoradiography were validated by immunohistochemistry and poly-GA immunoassays. Moreover, we confirmed antibody uptake in the CNS in a pharmacokinetic study of the perfused tissues. In summary, [^{64}Cu]Cu-NODAGA-mAb1A12 demonstrated favorable *in vitro* characteristics and an increased relative binding in poly-GA transgenic mice compared to wild-type mice *in vivo*. Our results with this first-in-class radiotracer suggested that targeting poly-GA is a promising approach for PET/CT imaging in FTD/ALS.

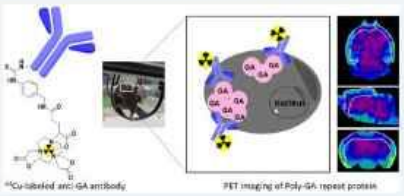

KEYWORDS: *Copper-64, mAb1A12, PET/CT, poly-GA, FTD/ALS*

Frontotemporal dementia (FTD) is a clinical syndrome[1] caused by the degeneration of frontal and temporal lobes.[2] Depending on the affected regions, the main symptoms are changes in behavior and personality or speech and language deficits.[1,3,4] Amyotrophic lateral sclerosis (ALS) is a related neurodegenerative disorder,[5] characterized by loss of cortical and spinal motor neurons, which leads to progressive paralysis and ultimately respiratory failure.[2,5−7] Both neurodegenerative diseases show genetic, clinical, and pathological overlap, e.g., ALS patients develop mild FTD-like symptoms and vice versa.[2,6] A $(G_4C_2)_n$ hexanucleotide repeat expansion upstream of the *C9orf72* (chromosome 9 open reading frame 72) coding region[1] is the most common known genetic cause of ALS and FTD in the western world and is found in 5−10% of all patients.[2,6,8,9] Unconventional translation of bidirectional repeat transcripts[6,10−12] results in five different dipeptide repeat proteins (DPR): poly-GA, poly-GP, poly-PA,[4,13] poly-GR, and poly-PR.[14] Selective expression of poly-GA, -GR, and -PR causes toxicity in various cell and animal models. The DPR proteins accumulate in neuronal inclusions, predominantly in the cytoplasm and less commonly in the nucleus.[14] Poly-GA inclusions are by far the most abundant and the other DPR proteins co-aggregate less commonly.[14−16] Poly-GA can be transmitted from cell to cell and is a key driver of disease development.[17−19] Poly-GA protein expression could contribute to cytoplasmic mislocalization and accumulation of

Received: January 23, 2024
Revised: April 4, 2024
Accepted: April 9, 2024

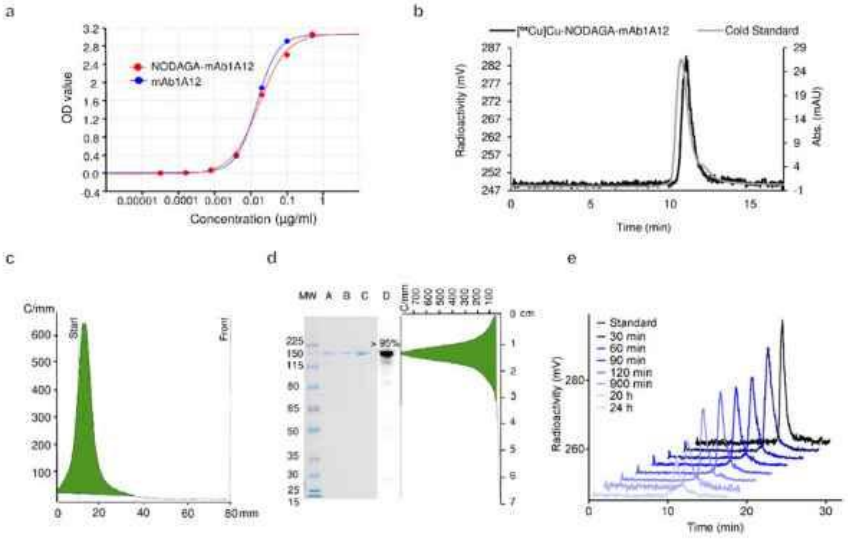

Figure 1. Characterization of NODAGA-mAb1A12 *in vitro*. (a) Determination of EC_{50} values for NODAGA-mAb1A12 (0.017 µg/mL) and mAb1A12 (0.015 µg/mL) by ELISA. (b) Representative HPLC chromatograms of cold standard (NODAGA-mAb1A12) in PBS, R_t = 10.8 min at 280 nm (UV channel) and [^{64}Cu]Cu-NODAGA-mAb1A12, R_t = 11.0 min (radioactivity channel). (c) Radio-TLC of [^{64}Cu]Cu-NODAGA-mAb1A12 on ITLC-SG chromatography paper, R_f (tracer) = 0.0−0.1; R_f (^{64}Cu) = 0.9−1.0. (d) SDS-PAGE of [^{64}Cu]Cu-NODAGA-mAb1A12 (A), NODAGA-mAb1A12 (B), and mAb1A12 (C) with autoradiography (D) and a radio-TLC scan of the SDS-PAGE gel. (e) Stability of [^{64}Cu]Cu-NODAGA-mAb1A12 in murine plasma over 24 h, as measured by SEC-HPLC (radioactivity channel).

phosphorylated TDP-43 in both patients and transgenic mice.[7,15,16,20] The anti-GA antibody 1A12[21] binds specifically to poly-GA proteins and thereby decreases cell-to-cell transmission and aggregation of poly-GA and subsequent TDP-43 mislocalization in cell culture.[7,17] Antibody therapy and active vaccination targeting poly-GA are promising therapeutic strategies.[15,22] Interestingly, poly-GA inclusions are already present prior to disease onset[23] and may contribute to the long prodromal disease phase with atrophy detectable 20 years prior to clinical onset, but correlate poorly with the degree of neurodegeneration in symptomatic cases.[3,21,24]

Based on these data, visualizing poly-GA aggregates in living patients could improve our understanding of *C9orf72* pathogenesis by allowing longitudinal studies from prodromal to end-stage diseases. Moreover, PET imaging of poly-GA pathology would be an attractive pharmacodynamic biomarker for future clinical trials. In this work, we developed a new radiotracer based on mouse monoclonal anti-GA antibody 1A12 for positron emission tomography. The tracer is able to visualize regional poly-GA pathology in a conditional mouse model expressing poly-GA in the neocortex and hippocampus.

■ RESULTS AND DISCUSSION

Radiolabeling Did Not Impair the Affinity or Stability of mAb1A12. To enable ^{64}Cu-labeling, we chemically conjugated the chelator *p*-NCS-benzyl-NODAGA to lysine residues of the mAb1A12 IgG2a antibody, resulting in the formation of a stable thiourea bond. The number of chelators per antibody was determined to be 1−3 using an arsenazo assay[25] (Supporting Figure S1).

The functionality of the unmodified and modified antibodies (0.5 µg/mL) was verified by enzyme-linked immunosorbent assay (ELISA) using a dilution series of GST-$(GA)_{15}$ antigen (Figure 1a). The EC_{50} values of NODAGA-mAb1A12 and mAb1A12 were comparable (0.017 vs 0.015 µg/mL). These results confirmed that antibody modification using NODAGA did not impair the binding affinity of mAb1A12.

Next, NODAGA-mAb1A12 was radiolabeled with [^{64}Cu]-$CuCl_2$ (Figure 1b,1c). The [^{64}Cu]Cu-NODAGA-mAb1A12 was obtained in high radiochemical purity (RCP) of 97.9 ± 1.9% (n = 5) and specific activity (A_s) of 1.0 ± 0.3 MBq/µg (n = 8). No [^{64}Cu]Cu-NODAGA complex or no free [^{64}Cu]-$CuCl_2$ was observed in the final product (Supporting Figure S2). In addition, SDS-PAGE, subsequent autoradiography, and a radio-TLC scan of the SDS-PAGE gel confirmed the high purity of the modified and radiolabeled antibodies (Figure 1d). To assess tracer stability, [^{64}Cu]Cu-NODAGA-mAb1A12 was incubated in mouse plasma, and stability was investigated by SEC-HPLC in a time series from 0.5 to 24 h. The tracer remained intact in the mouse plasma for at least 24 h (Figure 1e).

[^{64}Cu]Cu-NODAGA-mAb1A12 Detects Regional Poly-GA Pathology Using *In Vitro* Autoradiography. To confirm that the labeled antibody specifically targets cellular poly-GA inclusions, we used *in vitro* autoradiography combined with immunohistochemistry, taking advantage of a transgenic mouse model expressing high levels of GFP-$(GA)_{175}$.

CNS-wide expression of the GFP-$(GA)_{175}$ transgene using the Nestin-Cre driver[26] results in weight loss and weakness requiring termination at 6−7 weeks of age. To allow

https://doi.org/10.1021/acsptsci.4c00037
ACS Pharmacol. Transl. Sci. XXXX, XXX, XXX−XXX

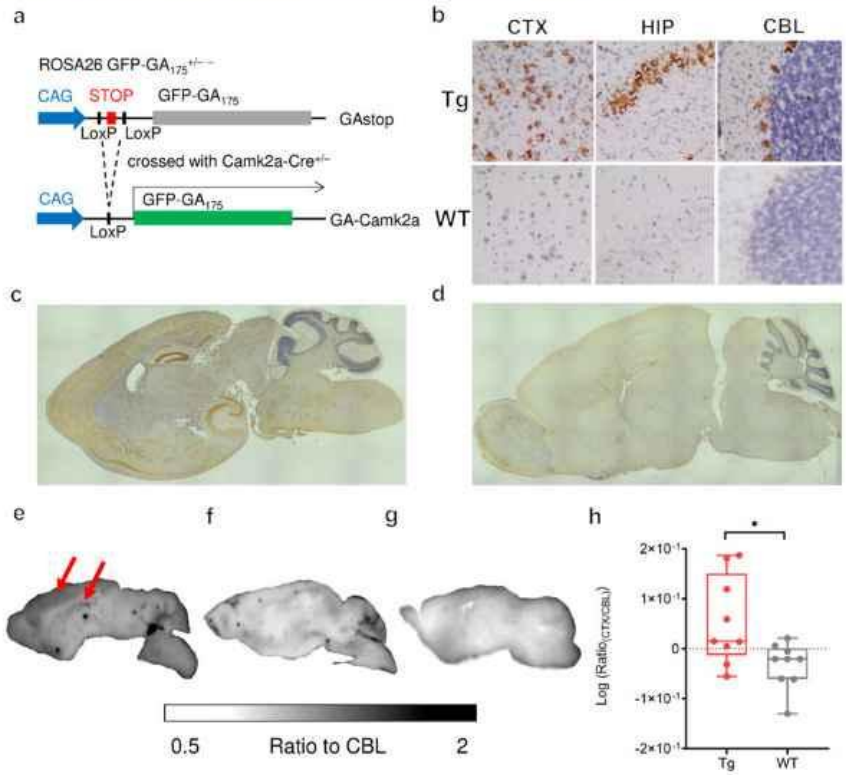

Figure 2. [^{64}Cu]Cu-NODAGA-mAb1A12 specifically detects poly-GA pathology using autoradiography. (a) Schematic depiction of the generation of the GA$^{\pm}$Camk2a$^{\pm}$ Tg mouse model. (b) IHC analysis of the cortex, hippocampus, and cerebellum in Tg and WT mice with 20× magnification. IHC overviews of brain sections from (c) transgenic and (d) wild-type mice. *In vitro* autoradiography of sagittal brain sections of (e) GA$^{\pm}$Camk2a$^{\pm}$ Tg and (f) wild-type mice. Intense signals are observed in the neocortex and hippocampus of the Tg mice (arrows). (g) *In vitro* autoradiography of the brain sections of the transgenic mice treated with tracer and a 1000-fold excess of native antibody shows a complete block of the signal. (h) The brain sections of transgenic mice revealed a higher cortex-to-cerebellum ratio than wild-type mice (mean ± SD, unpaired *t*-test, $p \leq 0.05$).

experiments in adult mice and comparison of poly-GA-expressing and -nonexpressing regions within each animal, we used Camk2a-Cre to drive poly-GA expression specifically in excitatory neurons[27] (Figure 2a). Immunohistochemistry (IHC) with mAb1A12 confirmed regional expression in the neocortex, striatum, and hippocampus with minimal staining in the cerebellum, consistent with the known expression pattern of Camk2a-Cre[26] (Figure 2b–d). In addition, we quantified poly-GA levels in the brains of transgenic (Tg) mice using a poly-GA immunoassay (Supporting Figure S3 and Table S1). The highest poly-GA concentration was observed in the cortex and hippocampus, the lower levels in the midbrain and brainstem, and the lowest in the cerebellum. Control (WT) mice only showed negligible background staining.

We incubated sagittal brain sections from Tg and WT mice with [^{64}Cu]Cu-NODAGA-mAb1A12. *In vitro* autoradiography showed elevated tracer accumulation in the cortex and hippocampus of GA$^{\pm}$Camk2a$^{\pm}$ Tg brain slices compared to wild-type (Figure 2e,2f), which is consistent with the results of IHC and poly-GA immunoassay. The cerebellum reveals unspecific uptake in both transgenic and wild-type sections, qualifying the cerebellum as a reference region. To verify the specific interaction between the radiotracer and its target poly-GA, we performed a blocking experiment. The brain sections of transgenic mice were treated with the radiotracer in the presence of a 1000-fold excess of unlabeled antibodies, which resulted in a low-level homogeneous background signal (Figure 2g) similar to that of nontransgenic controls. Thus, [^{64}Cu]Cu-NODAGA-mAb1A12 shows high specificity for its target poly-GA in mouse tissues.

To obtain a quantitative readout from the *in vitro* autoradiography experiments, the cortex-to-cerebellum ratio ($Ratio_{CTX/CBL}$) was calculated in brain sections from transgenic ($n = 6$) and wild-type ($n = 4$) mice. The $\log_{10}$ ($Ratio_{CTX/CBL}$) was 0.05 ± 0.09 (mean ± SD) for Tg and −0.03 ± 0.05 for WT mice (Figure 2h).

PET Imaging 20 h Post-Injection Shows the Strongest Difference between Tg and WT Mice. To assess the novel poly-GA tracer *in vivo*, we used combined PET/CT in poly-GA transgenic and wild-type mice and analyzed the kinetics of

https://doi.org/10.1021/acsptsci.4c00037
ACS Pharmacol. Transl. Sci. XXXX, XXX, XXX−XXX

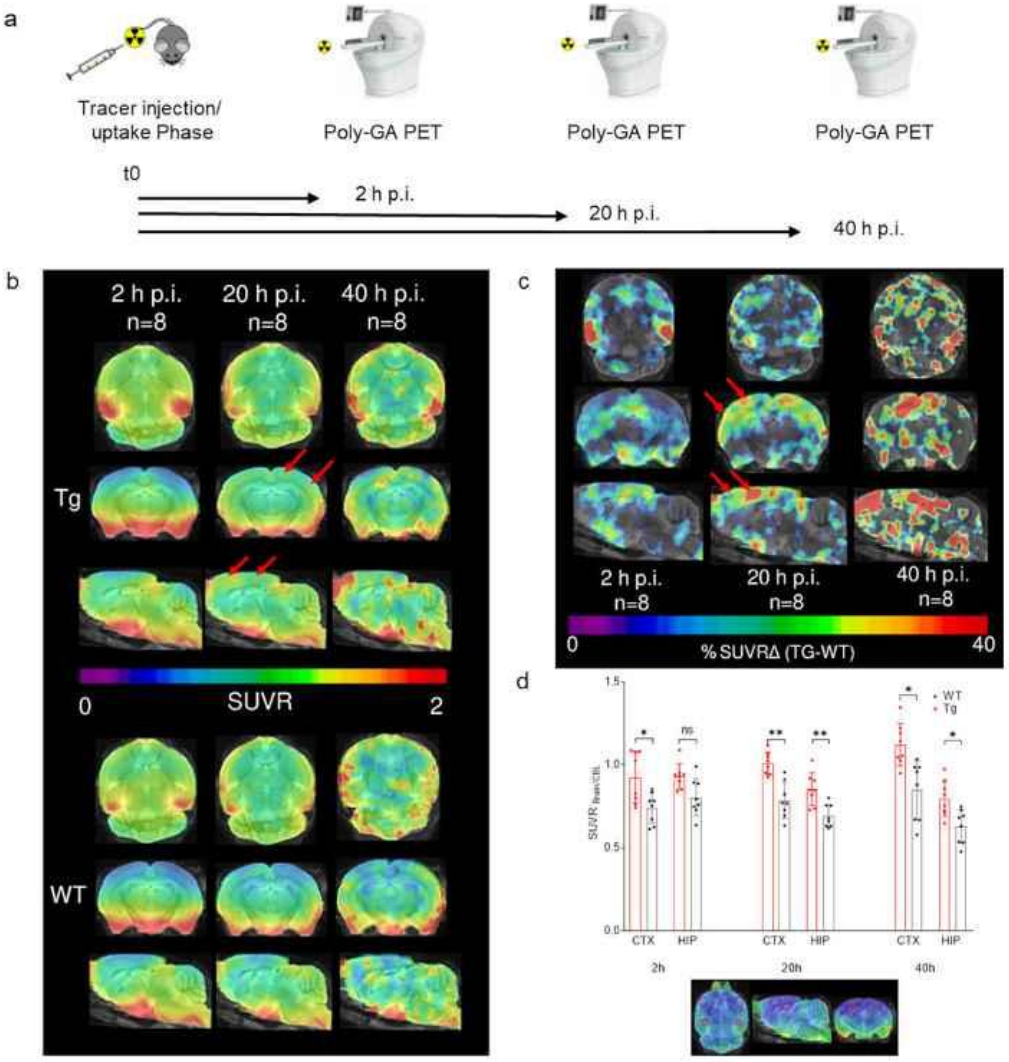

Figure 3. [^{64}Cu]Cu-NODAGA-mAb1A12 specifically detects neocortical poly-GA pathology in transgenic mice by PET. (a) Graphical representation of the PET study design. (b) PET SUVR images of the brains of Tg vs WT mice ($n = 8$) at 2, 20, and 40 h p.i. The color code shows the mean PET signal normalized to that of the cerebellum. Note that the basal brain regions initially take up antibodies regardless of genotype. At 20 h p.i., clear enrichment of the PET tracer is seen in the neocortex (arrows). (c) Differential PET images (% SUVRΔ) showing transgene-specific enrichment in the cortical areas (arrows). (d) $SUVR_{Brain/CBL}$ in the cortex and hippocampus of Tg and WT mice, measured by PET at 2, 20, and 40 h p.i. ($n = 8$) (mean ± SD, two-way analysis of variance (ANOVA) and Sidak's test for multiple comparisons, $p \leq 0.05$ (*) and ≤0.01 (**)). Circles in the images below the graph indicate the VOIs (volume of interests) used to quantify tracer uptake (purple: CTX; red: HIP).

CNS uptake in a time series covering 2, 20, and 40 h post-injection (p.i.) since the uptake of antibodies across the blood–brain barrier and into aggregate-bearing neurons may be slow (Figure 3a).

Standardized uptake value ratios ($SUVR_{Brain/CBL}$) were used to visualize cortical tracer uptake in the PET images (Figure 3b) (SUV-scaled PET images are shown in the Supporting Figure S4). PET images showed a higher $SUVR_{Brain/CBL}$ ratio in the transgenic mouse brains than in the control group. This result was most evident in axial slices after 20 h p.i., particularly in the cortical band. To further illustrate this result, Figure 3c shows the difference of $SUVR_{Brain/CBL}$ (%ΔTg-WT) in the

https://doi.org/10.1021/acsptsci.4c00037
ACS Pharmacol. Transl. Sci. XXXX, XXX, XXX−XXX

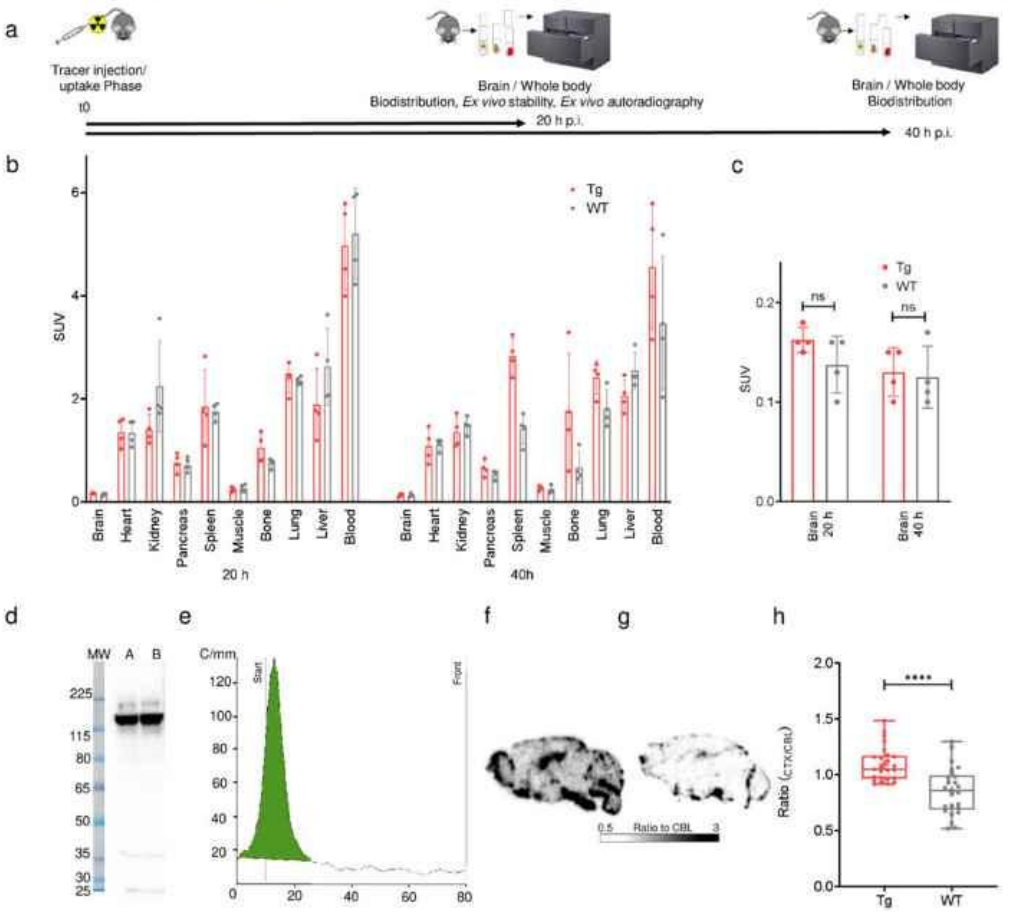

Figure 4. *Ex vivo* evaluation of [^{64}Cu]Cu-NODAGA-mAb1A12 shows an intact radiotracer and confirms the regional PET distribution pattern by autoradiography. (a) Graphical representation of the biodistribution study design. (b) SUV of [^{64}Cu]Cu-NODAGA-mAb1A12 in organs of WT and Tg mice at 20 and 40 h p.i. (n = 4), determined by biodistribution (mean ± SD). (c) SUV of [^{64}Cu]Cu-NODAGA-mAb1A12 in the brains of Tg vs WT mice (n = 4), measured by biodistribution at 20 and 40 h p.i. (mean ± SD, unpaired t-test, $p > 0.05$). (d) Autoradiography of SDS-PAGE gel loaded with plasma from two [^{64}Cu]Cu-NODAGA-mAb1A12-injected C57BL/6J mice (A, B). (e) Radio-TLC of plasma from [^{64}Cu]Cu-NODAGA-mAb1A12-injected C57BL/6J mice on ITLC-SG chromatography paper, R_f (tracer) = 0.0−0.1. *Ex vivo* autoradiography of brain sections from (f) transgenic and (g) wild-type mice. (h) Cortex-to-cerebellum ratio from *ex vivo* autoradiography sections of a representative transgenic and wild-type mouse (unpaired t-test, $p \leq 0.0001$).

brains of transgenic and wild-type mice. The strongest differences in $SUVR_{Brain/CBL}$ can be detected in the cortical band 20 h p.i. At 40 h p.i., PET signals became noisy due to low radioactivity levels in the brain, which may be explained by the decay of copper-64 (12.7 h half-life). Nevertheless, patches of enhanced $SUVR_{Brain/CBL}$ difference in the cortex are clearly visible.

Next, we quantified the SUV from the cortex and hippocampus normalized to the SUV in the cerebellum ($SUVR_{Brain/CBL}$) to compare the wild-type and transgenic mice. The VOIs (volume of interests) were carefully chosen to exclude regions rich in the vasculature, such as the ventricles and meninges. The $SUVR_{Brain/CBL}$ in the cortex and hippocampus of transgenic mice was significantly higher (up to 27%) than that in wild-type animals at 20 and 40 h p.i., indicating the sensitivity of this approach in distinguishing pathological from normal physiological states (Figure 3d). The $SUVR_{Brain/CBL}$ in the hippocampus decreased over time, whereas the $SUVR_{Brain/CBL}$ in the cortical band increased. Analysis of variance revealed a significant effect of genotype and time on tracer uptake in each brain area (Supporting Data).

***Ex Vivo* Analysis Confirms Enrichment of Anti-GA Tracer in the Brain of poly-GA Mice.** To further analyze the biodistribution of [^{64}Cu]Cu-NODAGA-mAb1A12, the isolated

https://doi.org/10.1021/acsptsci.4c00037
ACS Pharmacol. Transl. Sci. XXXX, XXX, XXX−XXX

organs of transgenic and wild-type mice were measured in a γ counter at 20 and 40 h p.i., and the tracer uptake was expressed as SUVs (standardized uptake values) (Figure 4a,4b and Supporting Table S2). There was a trend toward higher tracer uptake in the brain of the transgenic mice after 20 h compared to the wild type (Figure 4c). Most of the tracer remained in the blood circulation, as expected for antibodies. Increased tracer uptake was detected in the bone (SUV = 1.76) and spleen (SUV = 2.83) of transgenic mice at 40 h p.i. compared to that at 20 h p.i. (bone: 1.04, spleen: 1.84). Quantification of poly-GA levels in the peripheral organs of Tg and WT mice revealed only low poly-GA concentrations, indicating off-target binding of the antibody in these organs (Supporting Figure S3 and Table S1). To verify that no radiometal was detached from the complex, we performed *ex vivo* stability analysis using SDS-PAGE and radio-TLC of plasma samples from [^{64}Cu]Cu-NODAGA-mAb1A12-injected C57BL/6J mice at 20 h p.i. SDS-PAGE revealed an intact radiotracer and hardly any other proteins that might have been radiolabeled via transchelation (Figure 4d). Moreover, radio-TLC confirmed the absence of unbound copper-64 (Figure 4e). Release of the radiometal would also result in the accumulation of radioactivity in the liver due to its association with enzymes such as ceruloplasmin.[28] However, we did not observe any significant accumulation of radioactivity in the liver over time. Thus, we conclude that the complex is stable *in vivo* within the time of investigation and decomplexation does not occur.

To confirm CNS exposure to the 1A12 antibody, we performed a pharmacokinetic study in wild-type C57BL/6JOlaHsd mice that received a single dose of 1A12 antibody (IgG1, IgG2a, or IgG2c subtype, 30 mg/kg, s.c.). For this study, mice were extensively perfused with PBS prior to tissue collection before measuring antibody levels by immunoassay for up to 28 days after administration (Supporting Figure S5 and Table S3). Pharmacokinetic data unequivocally prove CNS exposure of the IgG2a isotype 1A12 antibody. 1A12 variants of the mIgG1 and mIgG2c isotypes also reached the CNS but at lower levels.

To validate the PET results, we performed *ex vivo* autoradiography on transgenic and wild-type mouse brain sections after 20 h p.i. and the final PET/CT scans (Figure 4f,4g). Visual assessment was impaired by interference signals from the vessels. To account for the uptake of the radiotracer in the brain parenchyma, we drew regions of interest excluding the vessels, and cortex-to-cerebellum ratios were calculated. Quantitative analysis of 25 sections of a representative mouse from each group confirmed a higher cortex-to-cerebellum ratio in transgenic mice compared to the wild-type control (1.09 $\pm$ 0.15 vs 0.86 $\pm$ 0.21, mean $\pm$ SD) (Figure 4h), which is consistent with the results from IHC and *ex vivo* poly-GA quantification in various brain regions by immunoassay.

In this study, we developed and evaluated a ^{64}Cu-labeled monoclonal anti-GA antibody (mAb1A12) as a novel tracer for the PET imaging of *C9orf72* FTD/ALS. The tracer clearly showed an increased signal in the brain of poly-GA-expressing mice *in vivo*, consistent with the beneficial effects observed in anti-GA immunotherapy strategies,[15,17,22] but due to limited penetration of the blood–brain barrier, the signal-to-noise ratio was rather low.

PET tracers for Aβ (such as PiB) have been instrumental as pharmacodynamic markers in large clinical trials to evaluate the efficacy of treatments aimed at reducing brain Aβ-deposits.[29] While small-molecule tracers for intracellular Tau are approaching clinical use, the development of suitable PET tracers for other less-abundant protein aggregates associated with neurodegenerative diseases (NDD), such as α-synuclein and TDP-43, has proven to be more challenging, which may be explained by the lower amounts compared to Aβ and Tau.

Monoclonal antibodies are one of the most important classes of biological agents used for targeted therapy and diagnostics. They exhibit several advantages, such as high affinity and specificity for their target and low background signal.[30,31] Because highly specific antibodies can be raised against almost any target molecule, monoclonal antibodies have become increasingly popular for molecular imaging and radionuclide therapy.[30,32] However, the large size of antibodies (150 kDa) greatly limits delivery across the blood–brain barrier (BBB).[30] However, 0.1–0.5% of unmodified antibodies reach the CNS, and the Aβ antibodies aducanumab and lecanemab have been approved for the treatment of Alzheimer's disease. Antibodies targeting intraneuronal aggregates are in clinical trials for Tau and α-synuclein.[7,33] Attempts have been made to facilitate delivery across the BBB, for example, by targeting the transferrin receptor (TfR). Transferrin receptor ligands promote the active transport of large cargo via transcytosis across brain endothelial cells. As a result, high-resolution PET/CT images can be obtained with radiolabeled bispecific antibodies, e.g., targeting Aβ.[30,34] A similar strategy would likely improve the signal-to-noise ratio for our tracer.

Two important factors to be considered in the development of a new tracer based on antibodies are the choice of the radiometal and a suitable chelator since the high stability of the radiometal–chelator complex *in vivo* and the half-life of the radionuclide are important factors given the slow and inefficient delivery to the CNS.[35] Zr-89 is very common to radiolabel antibodies due to its long half-life, and ^{89}Zr-DFO* complexes demonstrate good *in vivo* stability and have been applied in numerous clinical studies. However, high-energy γ emissions with high abundance in combination with a longer half-life are rather unfavorable in terms of absorbed doses. In this study, we selected the positron emitter copper-64, due to its half-life of 12.7 h, which enables imaging also at late time points, and its low positron energy, which results in high-resolution images. Moreover, its coordination chemistry is well understood, and several available chelators form complexes that are stable *in vivo*.[28,35] We conjugated the mAb1A12 antibody to *p*-NCS-benzyl-NODAGA since antibody modification and radiolabeling with copper-64 can be achieved under mild conditions, especially innocuous pH. In addition, the [^{64}Cu]Cu-NODAGA complex is highly stable *in vivo*. Radiolabeling was performed with high RCY and high RCP. The tracer was also shown to be stable for at least 24 h in murine plasma. The antibody was modified in a nonselective fashion, with the inherent risk of compromising target binding if the chelator interacted with the antibody epitope. However, ELISA confirmed that the binding affinity was not impaired after chemical modification. *In vitro* autoradiography showed tracer accumulation primarily in the neocortex and hippocampus of transgenic mice, consistent with immunohistochemical staining and the known Camk2a-Cre expression pattern, resulting in high poly-GA levels in these regions. The cerebellum was chosen as an internal reference region since the expression of poly-GA is low in this brain area and is not susceptible to any significant variation between animals. Therefore, the calculation of SUV ratios (SUVR) is a valuable tool for quantifying region-specific tracer uptake in the brain.

https://doi.org/10.1021/acsptsci.4c00037
ACS Pharmacol. Transl. Sci. XXXX, XXX, XXX−XXX

The SUVR values were significantly higher in Tg mice than in WT mice. Tracer binding to the poly-GA inclusions is highly specific, as shown by a blocking experiment in the presence of an excess of native antibodies.

Based on the favorable *in vitro* characteristics, tracer pharmacokinetics were assessed *in vivo* using a novel transgenic mouse model that allows conditional expression of GFP-$(GA)_{175}$ in excitatory neurons in the neocortex, hippocampus, and striatum using Camk2a-Cre because widespread expression in the CNS using Nestin-Cre resulted in a severe phenotype that would make PET/CT studies difficult.[26] Using Camk2a-Cre, mice develop cognitive deficits and reach the humane endpoint around 30 weeks of age compared to approximately 6 weeks of age for Nestin-Cre (in-depth characterization in preparation, Zhou et al.). The PET/CT imaging revealed increasing and most prominent enrichment of the [^{64}Cu]Cu-NODAGA-mAb1A12 tracer in the cortex of transgenic mice over time compared to that of WT, represented by higher $SUVR_{Brain/CBL}$ values. Both genotype and time significantly influence tracer uptake. PET images also indicate that 20 h p.i. is a favorable time point for image acquisition. Differential SUVR PET/CT images at 20 h p.i. show nearly optimal tracer distribution, whereas very early time points fail to identify clear distribution differences due to the slow uptake of antibodies across the BBB. Late time points are less useful due to the decay of ^{64}Cu, resulting in low radioactivity levels and low signal-to-noise ratios, leading to inferior image quality and poor accuracy of PET data. Relative differences in the images between transgenic and control mice are comparable to those seen with established amyloid-β radiotracers used for PET imaging in Alzheimer's disease.[36,37] Moreover, our data were obtained using a small-animal PET scanner with limited spatial resolution compared to human imaging. Due to the low resolution of PET/CT, we cannot distinguish between intracellular uptake of antibodies and binding of antibodies to extracellular poly-GA transmitted between cells.[17] These data support the development of an active and passive immunization therapeutic approach for poly-GA by showing target engagement in vivo.[15,22]

Consistent with the known poor penetration of antibodies through the BBB, tracer uptake in the brain is rather low. Still, our single-dose pharmacokinetic study proved that the antibody is able to penetrate the BBB, supporting the observation that the radiotracer enters the brain in sufficient amounts to obtain robust PET signals, despite high antibody levels in the vasculature. Whereas biodistribution revealed only a trend toward higher CNS retention in Tg animals 20 h p.i., PET and *ex vivo* autoradiography showed a significant difference between the two groups. The lack of significant biodistribution differences between genotypes at the group level is reasonable since regional analysis by PET and autoradiography allows for a local assessment of tracer uptake alterations, whereas biodistribution accounts for the overall tracer uptake in the brain, including basal activity levels. This shows that PET is an extremely valuable tool to detect regional differences in brain uptake, which cannot be achieved using other methods.

Biodistribution showed higher signals in the bone and spleen of transgenic mice after 40 h compared to 20 h post-injection. Presumably, the tracer also accumulates in the hematopoietic system over time, which may be driven by off-target binding of the radiotracer since poly-GA levels in the peripheral tissue were negligible. The antibody levels in the whole blood of Tg mice were also high. However, *ex vivo* autoradiography demonstrated a significant difference in the cortex/cerebellum ratio, clearly demonstrating that the uptake can be attributed to specific binding to poly-GA aggregates and that it is not just perfusion-driven. IHC and biochemical assessment of poly-GA levels confirm high target expression in brain regions, consistent with the expression pattern of the Camk2a-Cre driver.[27] These data fully corroborate the increased signals in PET and *ex vivo* autoradiography, thus providing strong evidence that the antibody enters the brain and that the signal is not derived from the vasculature.

The distribution of poly-GA in our mouse model is different from human *C9orf72* ALS/FTD because the cerebellum is largely spared in these mice.[4,13] The mouse model may show more peripheral expression than patients, who express poly-GA mainly in the CNS and to a lesser extent in the muscle and testis.[13,38] In *C9orf72* patients, poly-GA pathology is highly abundant in the neocortex, hippocampus, and thalamus.[21] It would be interesting to test whether the onset of poly-GA pathology in *C9orf72* mutation carriers correlates with the prodromal atrophy reported in these regions.[3] PET may also be useful to track poly-GA pathology in therapeutic studies in future clinical trials. Therefore, clinical translation of a poly-GA tracer is highly desired; however, improving BBB transmission through a shuttle system will likely be required to improve the signal-to-noise ratio for clinical use.

■ CONCLUSIONS

Herein, we present the first poly-GA targeting radiotracer and provide comprehensive *in vitro*, *in vivo*, and *ex vivo* data demonstrating that [^{64}Cu]Cu-NODAGA-mAb1A12 is a useful tracer for preclinical *C9orf72* ALS/FTD imaging. Despite low BBB penetration, high-quality images were obtained. To enhance tracer uptake in the brain, the 1A12 antibody can be engineered for receptor-mediated transcytosis via the TfR.

■ MATERIALS AND METHODS

The supporting information provides detailed information on the materials and experimental procedures, including methods, figures, and data for ELISA, SDS-PAGE, *in vitro* stability experiments, immunohistochemistry, PET/CT statistics, the arsenazo spectrometric assay, poly-GA immunoassay, the pharmacokinetics study, biodistribution, HPLC, radio-TLC chromatograms, and SUV-scaled PET images.

Animals. Floxed GA-stop mice were described previously and maintained at the C57BL/6J background. Briefly, GFP-$(GA)_{175}$ genes encoding nonrepeating alternate codons downstream of a floxed stop cassette encoding a puromycin resistance gene followed by SV40 polyadenylation signal were integrated at the Rosa26 safe harbor.[26] Crossing GA-stop with Camk2a-Cre (Tg(Camk2a-cre)93Kln)[27] and subsequent excision of the stop cassette resulted in DPR expression throughout Camk2a-positive excitatory neurons (ROSA26 GFP-$(GA)_{175}$ ±; Camk2a-Cre ±). The full phenotypic characterization of this mouse line will be reported in another article, which is currently under preparation. We compared (ROSA26 GFP-$(GA)_{175}$ ±; Camk2a-Cre ±) transgenic mice (Tg) and GA± Camk2a-Cre −/− littermate controls that did not express poly-GA referred to as wild-type (WT) mice (4−7 months, 15−33 g).

Antibody Modification. The mAb1A12 antibody modification was performed with *p*-NCS-benzyl-NODAGA (2,2′-

https://doi.org/10.1021/acsptsci.4c00037
ACS Pharmacol. Transl. Sci. XXXX, XXX, XXX−XXX

(7-(1-carboxy-4-((4-isothiocyanatobenzyl)amino)-4-oxobutyl)-1,4,7-triazonane-1,4-diyl)diacetic acid, CheMatech, Macrocycle Design Technologies) in metal-free phosphate buffer (pH 8.5, 0.1 M) as follows. The 1A12 antibody (4 mg) was dissolved in 1 mL of metal-free phosphate buffer (0.1 M, pH 8.5). An excess amount of dissolved *p*-NCS-benzyl-NODAGA (3.8 mg, 100 μL, 7.3 μmol) in metal-free phosphate buffer (0.1 M, pH 8.5) was added to the antibody solution. The reaction mixture was incubated overnight at 4 °C.[39] The mixture was purified using either Microcon centrifugal filter units (Ultracel 30 kDa, 0.5 mL, Merck Millipore Ltd.) or Amicon ultra-centrifugal filter units (Ultracel 30 kDa, 0.5 mL, Merck Millipore Ltd.). The buffer was changed to metal-free ammonium acetate (0.5 M, pH 6.8) by centrifugation (20,817*g*, 20 min, 4 °C, Centrifuge 5810 R, Eppendorf). Quality control of the conjugated antibody was performed by HPLC (Agilent Technologies, 1200 series) using a Phenomenex column (BioSep 5 μm SEC-s 4000 500 Å LC Column 300 mm × 7.8 mm) with 0.1 M sodium phosphate buffer (pH 7.2, isocratic run, 1 mL/min, 20−30 min). NODAGA-mAb1A12 eluted at R_t = 10.0 min, as detected by UV adsorption (280 nm).

Radiolabeling. NODAGA-mAb1A12 was centrifuged (5 min, 20,817*g*, 4 °C, Ultracel 30 kDa, 0.5 mL, Merck Millipore Ltd.) in order to decrease the reaction volume to 200 μL of ammonium acetate buffer (0.5 M, pH 6.8) before labeling. Next, 100−150 MBq [^{64}Cu]$CuCl_2$ was added to NODAGA-mAb1A12 (100 μg). The pH was adjusted to 5.6 using ammonium acetate buffer (0.1 M, pH 5.5). The mixture was incubated for 30−45 min, with gentle shaking at 400 r.p.m. at 42 °C. The reaction mixture was purified using Microcon Centrifugal filter units, and the buffer was changed to phosphate-buffered saline (ABX) for injection into mice. For quality control, radio-TLC on ITLC-SG glass microfiber chromatography paper (Agilent Technologies, Folsom, CA) was performed with sodium citrate buffer (0.1 M, pH 5.0) as the mobile phase (R_f (tracer) = 0.0, R_f ([^{64}Cu]$CuCl_2$) = 0.9, R_f ([^{64}Cu]Cu-NODAGA) = 0.5). Furthermore, radio-HPLC showed a retention time of 11.0 min for [^{64}Cu]Cu-NODAGA-mAb1A12.

Autoradiography. Brain sections from GA ± Camk2a ± Tg vs WT mice were deparaffinized in xylene followed by washing with 100, 99, 95, and 70% ethanol and water. The sections were preincubated in 50 mM Tris-HCl (pH 7.4, RT, 10 min) and then incubated with a maximum of 1 MBq/mL of [^{64}Cu]Cu-NODAGA-mAb1A12 in phosphate buffer (pH 7, 60 min, RT). To determine specificity, brain sections from GA ± Camk2a ± Tg mice were preincubated with a 1000-fold excess of nonlabeled mAb1A12 (300 μg) in the presence of ∼0.3 MBq [^{64}Cu]Cu-NODAGA-mAb1A12 (0.3 μg). The sections were washed with cold Tris-HCl + 5% ethanol (pH 7.4, 1 × 5 min, 4 °C), followed by distilled water (RT, 5 s). Finally, the sections were dried at RT for 1 h. *Ex vivo* autoradiography was performed on the transgenic and wild-type mice after 20 h p.i. After the PET/CT scan, one hemisphere of the brain was isolated and fixed on a polymer (Tissue-Tek O.C.T. compound). The brain was frozen at −20 °C and cut into sagittal sections of 20 μm thickness using a Leica CM 1860 cryostat machine. All brain sections were exposed to a phosphor imaging plate for 24 to 30 h in the dark at RT and then scanned with a CR-Reader (CR35 BIO, DÜRR MEDICAL). The images were analyzed using Aida Image Analyzer software (v.4.50.010, Elysia-raytest GmbH). A manually drawn region of interest (ROI) was placed in the cerebellum as a pseudoreferencing tissue. After background subtraction, intensity normalization of all sections was performed by calculating the brain-to-cerebellum (CBL) ratios.

Small-Animal PET/CT Imaging. Mice (4−7 months) were injected with 9.7 ± 2.4 MBq of [^{64}Cu]Cu-NODAGA-mAb1A12 (corresponding to 10.3 ± 3.0 μg per mouse) in 200 μL of phosphate buffer via the lateral tail vein under isoflurane anesthesia. The mice (n = 8) were scanned first with CT (70kVp/650 μA, exposure time 300 ms, Helical 1.0 pitch). The scan was followed by 30 min static animal PET imaging (with coincidence mode 1−5 in 1 scan position) 2, 20, and 40 h post-injection (p.i.). Small-animal PET imaging was carried out under constant anesthesia with isoflurane (1.5% at 1.5 L flow per minute) with a Mediso Nanoscan PET/CT (Budapest, Hungary). PET/CT images were reconstructed using the Tera Tomo 3D algorithm (4 iterations and 6 subsets) and analyzed using PMOD (version 3.5; PMOD Technologies Ltd., Zurich, Switzerland). PET images of each mouse were co-registered with CT images of the corresponding mice. The images were aligned to the magnetic resonance imaging (MRI) mouse brain atlas. Volumes of interest (VOIs) were drawn to assess tracer enrichment in different brain regions (from the atlas and manually as spheres). Standard uptake value (SUV) ratios were calculated by dividing the SUV of interest by that of the cerebellum. Average and differential (%SUVRΔ (Tg-WT)) PET images were generated from all measured mice (n = 8 per group) at 2 h, 20 and 40 h p.i.

Biodistribution. The biodistribution of [^{64}Cu]Cu-NODAGA-mAb1A12 was studied in GA ± Camk2a ± Tg vs WT mice at 20 and 40 h p.i. (n = 4). After PET/CT scanning, the mice were transferred to the anesthesia box for isoflurane overdose and euthanized by cervical dislocation. Mouse organs including the brain, heart, kidneys, liver, bone, muscle, spleen, pancreas, lungs, and blood were collected for biodistribution analysis. The brain was divided into two hemispheres. One hemisphere was used for biodistribution together with the other organs. The mass and radioactivity of each organ were measured in a γ counter (HIDEX AMG γ Counter, version 1.6.0.0, counting time of 1 min, counting window of 450−570 keV).

Statistical Analysis. Statistical analyses were conducted using GraphPad Prism 8.4.3 and 9. Unpaired Student's t-test, two-way ANOVA, or pairwise Sidak's multiple comparison tests were performed, as indicated in the captions. Statistical significance was set at $p > 0.05$ (ns), ≤ 0.05 (*), ≤ 0.01 (**), ≤ 0.001 (***), and ≤0.0001 (****).

■ ASSOCIATED CONTENT

Supporting Information

The Supporting Information is available free of charge at https://pubs.acs.org/doi/10.1021/acsptsci.4c00037.

Materials, supporting methods for ELISA, SDS-PAGE, *in vitro* stability experiments, immunohistochemistry, and PET/CT statistics; figures of the arsenazo spectrometric assay, HPLC and radio-TLC chromatograms, poly-GA immunoassay, SUV-scaled PET images, and pharmacokinetic studies; data on poly-GA concentrations in tissue, biodistribution, and pharmacokinetic studies (PDF)

https://doi.org/10.1021/acsptsci.4c00037
ACS Pharmacol. Transl. Sci. XXXX, XXX, XXX−XXX

AUTHOR INFORMATION

Corresponding Author

Simon Lindner − *Department of Nuclear Medicine, University Hospital, LMU Munich, 81377 Munich, Germany;* orcid.org/0009-0007-4379-4436; Email: simon.lindner@med.uni-muenchen.de

Authors

Monireh Shojaei − *Department of Nuclear Medicine, University Hospital, LMU Munich, 81377 Munich, Germany*

Qihui Zhou − *German Center for Neurodegenerative Diseases (DZNE), 81377 Munich, Germany*

Giovanna Palumbo − *Department of Nuclear Medicine, University Hospital, LMU Munich, 81377 Munich, Germany*

Rebecca Schaefer − *Department of Nuclear Medicine, University Hospital, LMU Munich, 81377 Munich, Germany*

Janne Kaskinoro − *Orion Corporation Orion Pharma, 02200 Espoo, Finland*

Pirjo Vehmaan-Kreula − *Orion Corporation Orion Pharma, 02200 Espoo, Finland*

Peter Bartenstein − *Department of Nuclear Medicine, University Hospital, LMU Munich, 81377 Munich, Germany; Munich Cluster for Systems Neurology (SyNergy), 81377 Munich, Germany*

Matthias Brendel − *Department of Nuclear Medicine, University Hospital, LMU Munich, 81377 Munich, Germany; German Center for Neurodegenerative Diseases (DZNE), 81377 Munich, Germany; Munich Cluster for Systems Neurology (SyNergy), 81377 Munich, Germany*

Dieter Edbauer − *German Center for Neurodegenerative Diseases (DZNE), 81377 Munich, Germany; Munich Cluster for Systems Neurology (SyNergy), 81377 Munich, Germany*

Complete contact information is available at: https://pubs.acs.org/10.1021/acsptsci.4c00037

Author Contributions

All authors contributed to the study's conception and design. Material preparation, data collection, and analysis were performed by M.S., G.P., R.S., J.K., P.V.−K., and Q.Z. Analysis and data interpretation were done by S.L., M.B., D.E., and P.B. The first draft of the manuscript was written by M.S. All authors commented on the previous versions of the manuscript. All authors read and approved the final manuscript.

Notes

The authors declare no competing financial interest.

Animal handling and experiments in this study were performed under the supervision of a veterinarian in accordance with the German Animal Welfare Law and were approved by the Government of Upper Bavaria, Germany (vet_2−17−106).

ACKNOWLEDGMENTS

This work was supported by the Deutsche Forschungsgemeinschaft (DFG, German Research Foundation) within the framework of the Munich Cluster for Systems Neurology (EXC 2145 SyNergy—ID 390857198) (M.B., D.E., S.L.) and the Horizon Europe Framework Programme (HORIZON) under grant agreement 101057649 (GA-VAX) (D.E.).

ABBREVIATIONS

FTD, frontotemporal dementia; ALS, amyotrophic lateral sclerosis; PET/CT, positron emission tomography/computed tomography; SUVR, standardized uptake value ratio; VOI, volume of interest; RCP, radiochemical purity; RCY, radiochemical yield; HPLC, high-performance liquid chromatography; TLC, thin-layer chromatography; IHC, immunohistochemistry; CNS, central nervous system; TfR, transferrin receptor; BBB, blood−brain barrier

REFERENCES

(1) Puppala; Kumar, G.; Gorthi, S. P.; Chandran, V.; Gundabolu, G. Frontotemporal Dementia - Current Concepts. *Neurol. India* **2021**, *69*, 1144−1152, DOI: 10.4103/0028-3886.329593.

(2) McCauley, M. E.; Baloh, R. H. Inflammation in ALS/FTD pathogenesis. *Acta Neuropathol.* **2019**, *137*, 715−730.

(3) Rohrer, J. D.; Nicholas, J. M.; Cash, D. M.; van Swieten, J.; Dopper, E.; Jiskoot, L.; van Minkelen, R.; Rombouts, S. A.; Cardoso, M. J.; Clegg, S.; Espak, M.; Mead, S.; Thomas, D. L.; De Vita, E.; Masellis, M.; Black, S. E.; Freedman, M.; Keren, R.; MacIntosh, B. J.; Rogaeva, E.; Tang-Wai, D.; Tartaglia, M. C.; Laforce, R.; Tagliavini, F.; Tiraboschi, P.; Redaelli, V.; Prioni, S.; Grisoli, M.; Borroni, B.; Padovani, A.; Galimberti, D.; Scarpini, E.; Arighi, A.; Fumagalli, G.; Rowe, J. B.; Coyle-Gilchrist, I.; Graff, C.; Fallström, M.; Jelic, V.; Ståhlbom, A. K.; Andersson, C.; Thonberg, H.; Lilius, L.; Frisoni, G. B.; Binetti, G.; Pievani, M.; Bocchetta, M.; Benussi, L.; Ghidoni, R.; Finger, E.; Sorbi, S.; Nacmias, B.; Lombardi, G.; Polito, C.; Warren, J. D.; Ourselin, S.; Fox, N. C.; Rossor, M. N. Presymptomatic cognitive and neuroanatomical changes in genetic frontotemporal dementia in the Genetic Frontotemporal dementia Initiative (GENFI) study: a cross-sectional analysis. *Lancet Neurol.* **2015**, *14*, 253−262.

(4) Mori, K.; Weng, S.-M.; Arzberger, T.; May, S.; Rentzsch, K.; Kremmer, E.; Schmid, B.; Kretzschmar, H. A.; Cruts, M.; Van Broeckhoven, C.; Haass, C.; Edbauer, D. The C9orf72 GGGGCC Repeat Is Translated into Aggregating Dipeptide-Repeat Proteins in FTLD/ALS. *Science* **2013**, *339*, 1335−1338.

(5) Neumann, M.; Sampathu, D. M.; Kwong, L. K.; Truax, A. C.; Micsenyi, M. C.; Chou, T. T.; Bruce, J.; Schuck, T.; Grossman, M.; Clark, C. M.; McCluskey, L. F.; Miller, B. L.; Masliah, E.; Mackenzie, I. R.; Feldman, H.; Feiden, W.; Kretzschmar, H. A.; Trojanowski, J. Q.; Lee, V. M. Y. Ubiquitinated TDP-43 in Frontotemporal Lobar Degeneration and Amyotrophic Lateral Sclerosis. *Science* **2006**, *314*, 130−133.

(6) Edbauer, D.; Haass, C. An amyloid-like cascade hypothesis for C9orf72 ALS/FTD. *Curr. Opin Neurobiol.* **2016**, *36*, 99−106.

(7) Khosravi, B.; LaClair, K. D.; Riemenschneider, H.; Zhou, Q.; Frottin, F.; Mareljic, N.; Czuppa, M.; Farny, D.; Hartmann, H.; Michaelsen, M.; Arzberger, T.; Hartl, F. U.; Hipp, M. S.; Edbauer, D. Cell-to-cell transmission of C9orf72 poly-(Gly-Ala) triggers key features of ALS/FTD. *EMBO J.* **2020**, *39*, No. e102811.

(8) Dormann, D.; Haass, C. TDP-43 and FUS: a nuclear affair. *Trends Neurosci.* **2011**, *34*, 339−348.

(9) Lomen-Hoerth, C.; Anderson, T.; Miller, B. The overlap of amyotrophic lateral sclerosis and frontotemporal dementia. *Neurology* **2002**, *59*, 1077−1079, DOI: 10.1212/WNL.59.7.1077.

(10) Mori, K.; Arzberger, T.; Grässer, F. A.; Gijselinck, I.; May, S.; Rentzsch, K.; Weng, S.-M.; Schludi, M. H.; van der Zee, J.; Cruts, M.; Van Broeckhoven, C.; Kremmer, E.; Kretzschmar, H. A.; Haass, C.; Edbauer, D. Bidirectional transcripts of the expanded C9orf72 hexanucleotide repeat are translated into aggregating dipeptide repeat proteins. *Acta Neuropathol.* **2013**, *126*, 881−893.

(11) Freibaum, B. D.; Taylor, J. P. The Role of Dipeptide Repeats in C9ORF72-Related ALS-FTD. *Front. Mol. Neurosci.* **2017**, *10*, No. 35, DOI: 10.3389/fnmol.2017.00035.

(12) Guo, Q.; Lehmer, C.; Martínez-Sánchez, A.; Rudack, T.; Beck, F.; Hartmann, H.; Pérez-Berlanga, M.; Frottin, F.; Hipp, M. S.; Hartl, F. U.; Edbauer, D.; Baumeister, W.; Fernández-Busnadiego, R. In Situ Structure of Neuronal C9orf72 Poly-GA Aggregates Reveals Proteasome Recruitment. *Cell* **2018**, *172*, 696−705.

(13) Ash, P. E. A.; Bieniek, K. F.; Gendron, T. F.; Caulfield, T.; Lin, W.-L.; DeJesus-Hernandez, M.; van Blitterswijk, M. M.; Jansen-West, K.; Paul, J. W.; Rademakers, R.; Boylan, K. B.; Dickson, D. W.;

https://doi.org/10.1021/acsptsci.4c00037
ACS Pharmacol. Transl. Sci. XXXX, XXX, XXX−XXX

Petrucelli, L. Unconventional Translation of C9ORF72 GGGGCC Expansion Generates Insoluble Polypeptides Specific to c9FTD/ALS. *Neuron* **2013**, *77*, 639−646.
(14) Lee, Y.-B.; Baskaran, P.; Gomez-Deza, J.; Chen, H.-J.; Nishimura, A. L.; Smith, B. N.; Troakes, C.; Adachi, Y.; Stepto, A.; Petrucelli, L.; Gallo, J.-M.; Hirth, F.; Rogelj, B.; Guthrie, S.; Shaw, C. E. C9orf72 poly GA RAN-translated protein plays a key role in amyotrophic lateral sclerosis via aggregation and toxicity. *Hum. Mol. Genet.* **2017**, *26*, 4765−4777.
(15) Zhou, Q.; Mareljic, N.; Michaelsen, M.; Parhizkar, S.; Heindl, S.; Nuscher, B.; Farny, D.; Czuppa, M.; Schludi, C.; Graf, A.; Krebs, S.; Blum, H.; Feederle, R.; Roth, S.; Haass, C.; Arzberger, T.; Liesz, A.; Edbauer, D. Active poly-GA vaccination prevents microglia activation and motor deficits in a C9orf72 mouse model. *EMBO Mol. Med.* **2020**, *12*, No. e10919.
(16) Khosravi, B.; Hartmann, H.; May, S.; Möhl, C.; Ederle, H.; Michaelsen, M.; Schludi, M. H.; Dormann, D.; Edbauer, D. Cytoplasmic poly-GA aggregates impair nuclear import of TDP-43 in C9orf72 ALS/FTLD. *Hum. Mol. Genet.* **2017**, *26*, 790−800.
(17) Zhou, Q.; Lehmer, C.; Michaelsen, M.; Mori, K.; Alterauge, D.; Baumjohann, D.; Schludi, M. H.; Greiling, J.; Farny, D.; Flatley, A.; Feederle, R.; May, S.; Schreiber, F.; Arzberger, T.; Kuhm, C.; Klopstock, T.; Hermann, A.; Haass, C.; Edbauer, D. Antibodies inhibit transmission and aggregation of C9orf72 poly-GA dipeptide repeat proteins. *EMBO Mol. Med.* **2017**, *9*, 687−702.
(18) Westergard, T.; Jensen, B. K.; Wen, X.; Cai, J.; Kropf, E.; Iacovitti, L.; Pasinelli, P.; Trotti, D. Cell-to-Cell Transmission of Dipeptide Repeat Proteins Linked to C9orf72-ALS/FTD. *Cell Rep.* **2016**, *17*, 645−652.
(19) Nonaka, T.; Masuda-Suzukake, M.; Hosokawa, M.; Shimozawa, A.; Hirai, S.; Okado, H.; Hasegawa, M. C9ORF72 dipeptide repeat poly-GA inclusions promote intracellular aggregation of phosphorylated TDP-43. *Hum. Mol. Genet.* **2018**, *27*, 2658−2670.
(20) Schludi, M. H.; Becker, L.; Garrett, L.; Gendron, T. F.; Zhou, Q.; Schreiber, F.; Popper, B.; Dimou, L.; Strom, T. M.; Winkelmann, J.; von Thaden, A.; Rentzsch, K.; May, S.; Michaelsen, M.; Schwenk, B. M.; Tan, J.; Schoser, B.; Dieterich, M.; Petrucelli, L.; Hölter, S. M.; Wurst, W.; Fuchs, H.; Gailus-Durner, V.; de Angelis, M. H.; Klopstock, T.; Arzberger, T.; Edbauer, D. Spinal poly-GA inclusions in a C9orf72 mouse model trigger motor deficits and inflammation without neuron loss. *Acta Neuropathol.* **2017**, *134*, 241−254.
(21) Mackenzie, I. R.; Arzberger, T.; Kremmer, E.; Troost, D.; Lorenzl, S.; Mori, K.; Weng, S.-M.; Haass, C.; Kretzschmar, H. A.; Edbauer, D.; Neumann, M. Dipeptide repeat protein pathology in C9ORF72 mutation cases: clinico-pathological correlations. *Acta Neuropathol.* **2013**, *126*, 859−879.
(22) Nguyen, L.; Montrasio, F.; Pattamatta, A.; Tusi, S. K.; Bardhi, O.; Meyer, K. D.; Hayes, L.; Nakamura, K.; Banez-Coronel, M.; Coyne, A.; Guo, S.; Laboissonniere, L. A.; Gu, Y.; Narayanan, S.; Smith, B.; Nitsch, R. M.; Kankel, M. W.; Rushe, M.; Rothstein, J.; Zu, T.; Grimm, J.; Ranum, L. P. W. Antibody Therapy Targeting RAN Proteins Rescues C9 ALS/FTD Phenotypes in C9orf72 Mouse Model. *Neuron* **2020**, *105*, 645−662.e611.
(23) Proudfoot, M.; Gutowski, N. J.; Edbauer, D.; Hilton, D. A.; Stephens, M.; Rankin, J.; Mackenzie, I. R. Early dipeptide repeat pathology in a frontotemporal dementia kindred with C9ORF72 mutation and intellectual disability. *Acta Neuropathol.* **2014**, *127*, 451−458.
(24) Staffaroni, A. M.; Quintana, M.; Wendelberger, B.; Heuer, H. W.; Russell, L. L.; Cobigo, Y.; Wolf, A.; Goh, S. M.; Petrucelli, L.; Gendron, T. F.; Heller, C.; Clark, A. L.; Taylor, J. C.; Wise, A.; Ong, E.; Forsberg, L.; Brushaber, D.; Rojas, J. C.; VandeVrede, L.; Ljubenkov, P.; Kramer, J.; Casaletto, K. B.; Appleby, B.; Bordelon, Y.; Botha, H.; Dickerson, B. C.; Domoto-Reilly, K.; Fields, J. A.; Foroud, T.; Gavrilova, R.; Geschwind, D.; Ghoshal, N.; Goldman, J.; Graff-Radford, J.; Graff-Radford, N.; Grossman, M.; Hall, M. G. H.; Hsiung, G. Y.; Huey, E. D.; Irwin, D.; Jones, D. T.; Kantarci, K.; Kaufer, D.; Knopman, D.; Kremers, W.; Lago, A. L.; Lapid, M. I.; Litvan, I.; Lucente, D.; Mackenzie, I. R.; Mendez, M. F.; Mester, C.; Miller, B. L.; Onyike, C. U.; Rademakers, R.; Ramanan, V. K.; Ramos, E. M.; Rao, M.; Rascovsky, K.; Rankin, K. P.; Roberson, E. D.; Savica, R.; Tartaglia, M. C.; Weintraub, S.; Wong, B.; Cash, D. M.; Bouzigues, A.; Swift, I. J.; Peakman, G.; Bocchetta, M.; Todd, E. G.; Convery, R. S.; Rowe, J. B.; Borroni, B.; Galimberti, D.; Tiraboschi, P.; Masellis, M.; Finger, E.; van Swieten, J. C.; Seelaar, H.; Jiskoot, L. C.; Sorbi, S.; Butler, C. R.; Graff, C.; Gerhard, A.; Langheinrich, T.; Laforce, R.; Sanchez-Valle, R.; de Mendonça, A.; Moreno, F.; Synofzik, M.; Vandenberghe, R.; Ducharme, S.; Le Ber, I.; Levin, J.; Danek, A.; Otto, M.; Pasquier, F.; Santana, I.; Kornak, J.; Boeve, B. F.; Rosen, H. J.; Rohrer, J. D.; Boxer, A. L.; et al. Temporal order of clinical and biomarker changes in familial frontotemporal dementia. *Nat. Med.* **2022**, *28*, 2194−2206.
(25) Brady, E. D.; Chong, H. S.; Milenic, D. E.; Brechbiel, M. W. Development of a spectroscopic assay for bifunctional ligand-protein conjugates based on copper. *Nucl. Med. Biol.* **2004**, *31*, 795−802.
(26) LaClair, K. D.; Zhou, Q.; Michaelsen, M.; Wefers, B.; Brill, M. S.; Janjic, A.; Rathkolb, B.; Farny, D.; Cygan, M.; de Angelis, M. H.; Wurst, W.; Neumann, M.; Enard, W.; Misgeld, T.; Arzberger, T.; Edbauer, D. Congenic expression of poly-GA but not poly-PR in mice triggers selective neuron loss and interferon responses found in C9orf72 ALS. *Acta Neuropathol.* **2020**, *140*, 121−142.
(27) Minichiello, L.; Korte, M.; Wolfer, D.; Kühn, R.; Unsicker, K.; Cestari, V.; Rossi-Arnaud, C.; Lipp, H. P.; Bonhoeffer, T.; Klein, R. Essential role for TrkB receptors in hippocampus-mediated learning. *Neuron* **1999**, *24*, 401−414.
(28) Price, E. W.; Orvig, C. Matching chelators to radiometals for radiopharmaceuticals. *Chem. Soc. Rev.* **2014**, *43*, 260−290.
(29) Sevigny, J.; Chiao, P.; Bussière, T.; Weinreb, P. H.; Williams, L.; Maier, M.; Dunstan, R.; Salloway, S.; Chen, T.; Ling, Y.; O'Gorman, J.; Qian, F.; Arastu, M.; Li, M.; Chollate, S.; Brennan, M. S.; Quintero-Monzon, O.; Scannevin, R. H.; Arnold, H. M.; Engber, T.; Rhodes, K.; Ferrero, J.; Hang, Y.; Mikulskis, A.; Grimm, J.; Hock, C.; Nitsch, R. M.; Sandrock, A. The antibody aducanumab reduces Aβ plaques in Alzheimer's disease. *Nature* **2016**, *537*, 50−56.
(30) Sehlin, D.; Syvänen, S. Engineered antibodies: new possibilities for brain PET? *Eur. J. Nucl. Med. Mol. Imaging* **2019**, *46*, 2848−2858.
(31) Hermanson, G. T. Antibody Modification and Conjugation. In *Bioconjugate Techniques*, 3rd ed.; Hermanson, G. T., Ed.; Academic Press: Boston, 2013; Chapter 20, pp 867−920.
(32) Schjoeth-Eskesen, C.; Nielsen, C. H.; Heissel, S.; Højrup, P.; Hansen, P. R.; Gillings, N.; Kjaer, A. [^{64}Cu]-labelled trastuzumab: optimization of labelling by DOTA and NODAGA conjugation and initial evaluation in mice. *J. Labelled Compd. Radiopharm.* **2015**, *58*, 227−233.
(33) Sengupta, U.; Kayed, R. Amyloid β, Tau, and α-Synuclein aggregates in the pathogenesis, prognosis, and therapeutics for neurodegenerative diseases. *Prog. Neurobiol.* **2022**, *214*, No. 102270.
(34) Faresjö, R.; Lindberg, H.; Ståhl, S.; Löfblom, J.; Syvänen, S.; Sehlin, D. Transferrin Receptor Binding BBB-Shuttle Facilitates Brain Delivery of Anti-Aβ-Affibodies. *Pharm. Res.* **2022**, *39*, 1509−1521.
(35) Price, T. W.; Greenman, J.; Stasiuk, G. J. Current advances in ligand design for inorganic positron emission tomography tracers ^{68}Ga, ^{64}Cu, ^{89}Zr and ^{44}Sc. *Dalton Trans.* **2016**, *45*, 15702−15724.
(36) Rominger, A.; Brendel, M.; Burgold, S.; Keppler, K.; Baumann, K.; Xiong, G.; Mille, E.; Gildehaus, F.-J.; Carlsen, J.; Schlichtiger, J.; Niedermoser, S.; Wängler, B.; Cumming, P.; Steiner, H.; Herms, J.; Haass, C.; Bartenstein, P. Longitudinal Assessment of Cerebral β-Amyloid Deposition in Mice Overexpressing Swedish Mutant β-Amyloid Precursor Protein Using ^{18}F-Florbetaben PET. *J. Nucl. Med.* **2013**, *54*, 1127−1134.
(37) Brendel, M.; Probst, F.; Jaworska, A.; Overhoff, F.; Korzhova, V.; Albert, N. L.; Beck, R.; Lindner, S.; Gildehaus, F. J.; Baumann, K.; Bartenstein, P.; Kleinberger, G.; Haass, C.; Herms, J.; Rominger, A. Glial Activation and Glucose Metabolism in a Transgenic Amyloid Mouse Model: A Triple-Tracer PET Study. *J. Nucl. Med.* **2016**, *57*, 954−960.
(38) Cykowski, M. D.; Dickson, D. W.; Powell, S. Z.; Arumanayagam, A. S.; Rivera, A. L.; Appel, S. H. Dipeptide repeat

https://doi.org/10.1021/acsptsci.4c00037
ACS Pharmacol. Transl. Sci. XXXX, XXX, XXX−XXX

(DPR) pathology in the skeletal muscle of ALS patients with C9ORF72 repeat expansion. *Acta Neuropathol.* **2019**, *138*, 667−670.
(39) Liu, Q.; Johnson, E. M.; Lam, R. K.; Wang, Q.; Ye, H. B.; Wilson, E. N.; Minhas, P. S.; Liu, L.; Swarovski, M. S.; Tran, S.; Wang, J.; Mehta, S. S.; Yang, X.; Rabinowitz, J. D.; Yang, S. S.; Shamloo, M.; Mueller, C.; James, M. L.; Andreasson, K. I. Peripheral TREM1 responses to brain and intestinal immunogens amplify stroke severity. *Nat. Immunol.* **2019**, *20*, 1023−1034.

https://doi.org/10.1021/acsptsci.4c00037
ACS Pharmacol. Transl. Sci. XXXX, XXX, XXX−XXX

Development and preclinical evaluation of a copper-64 labeled antibody targeting glycine-alanine dipeptides for PET imaging of *C9orf72* associated amyotrophic lateral sclerosis / frontotemporal dementia

Monireh Shojaei[1], Qihui Zhou[2], Giovanna Palumbo[1], Rebecca Schaefer[1], Janne Kaskinoro[3], Pirjo Vehmaan-Kreula[3], Peter Bartenstein[1,4], Matthias Brendel[1,2,4], Dieter Edbauer[2,4], Simon Lindner[1]*

1 Department of Nuclear Medicine, University Hospital, LMU Munich, 81377 Munich, Germany

2 German Center for Neurodegenerative Diseases (DZNE), 81377 Munich, Germany

3 Orion Corporation Orion Pharma, 02200 Espoo, Finland

4 Munich Cluster for Systems Neurology (SyNergy), 81377 Munich, Germany

*Corresponding author: simon.lindner@med.uni-muenchen.de

Supplemental Data

SUPPLEMENTAL METHODS

MATERIALS

Chemicals and materials were purchased from Merck, VWR, Thermo Fisher Scientific, CheMatech, Roche, Agilent, Eppendorf, and Sigma Aldrich, and were used as received without any purification. [^{64}Cu]$CuCl_2$ was obtained from the Department of Preclinical Imaging and Radiopharmacy, University Hospital Tuebingen, Germany.

ELISA

The Nunc MaxiSorp™ flat-bottom 96-well plates were incubated with recombinant GST-$(GA)_{15}$ produced in E. coli [1, 2] in PBS overnight at 4°C at various concentrations (0.5. 0.1, 0.02, 0.004, 0.0008, 0.00016, 0.00032 and 0 ng/µl). After 1 h incubation in blocking solution (1% BSA, 0.05% Tween 20 in PBS), 0.5 µg/ml of mAb1A12 or NODAGA-mAb1A12 were added for 1 h. After three washes with 0.05% Tween 20 in PBS, anti-GA antibodies were detected with anti-mouse HRP. 3,3′,5,5′-Tetramethylbenzidine was used as chromogenic substrate. After stopping the reaction with 2 M H_2SO_4, the absorbance was read at 450 nm. Two technical replicates were measured for each sample. EC_{50} values were calculated using Quest Graph EC_{50} Calculator, AAT Bioquest, Inc.

SDS-PAGE

Antibody integrity was assessed by SDS-PAGE under non-reducing conditions. Unmodified antibody mAb1A12, modified antibody NODAGA-mAb1A12 and labeled antibody [^{64}Cu]Cu-NODAGA-mAb1A12 (0.4 µg, PBS) were incubated with SDS sample buffer at 90°C for 10 min, loaded onto an 8% Bolt Bis-Tris Plus gel and run with MOPS buffer at 200V for 35 min. Spectra™ Multicolor Broad Range Protein Ladder (Thermo Fisher Scientific) served as standard. Coomassie staining (SimplyBlue Safestain, Thermo Fisher Scientific) was performed overnight. 2 mL of 20% aq. NaCl (w/v) were added to 20 mL of stain to avoid decrease of sensitivity. Radioactive read out of the gel was done via radio-TLC (miniGita, raytest, iTLC-SG, 0.1 M sodium citrate buffer pH 5) and autoradiography. The gel was exposed to a phosphorimaging plate for four hours, scanned with a CR-Reader (CR35 BIO, Dürr Medical), and analyzed using Aida Image Analyzer software.

Antibody integrity was analysed *ex vivo* in plasma samples from [^{64}Cu]Cu-NODAGA-mAb1A12 (46.0 ± 4.1 MBq, C57BL/6J, n = 3, 2 males and 1 female) injected mice 20h p.i. Blood was collected from the heart in EDTA tubes (Sarstedt Microvette 100 K3E). Tubes were centrifuged (3000 × g, 5 min) and the top layer (plasma) separated. Plasma concentrations were quantified by radioactivity measurements using a gamma counter. SDS-PAGE was performed as previously described, with the exception that 0.13 µg of antibody was loaded per well. Autoradiography and radio-TLC were performed accordingly.

IN VITRO STABILITY

The stability of ^{64}Cu-labeled NODAGA-mAb1A12 was determined in mouse plasma. Anaesthetized mice (isoflurane) were killed by cervical dislocation. Then, murine blood was collected by cardiac puncture and transferred to an Eppendorf tube. Murine plasma was separated from blood cells by centrifugation (Mini spin centrifuge, Eppendorf) for 10 min at 3000 × g and then stored at -20 °C. 113 MBq of [^{64}Cu]Cu-NODAGA-mAb1A12 in 70 µL phosphate-buffered saline were incubated in 200 µL murine plasma

(gentle shaking at 400 r.p.m, 37°C, 24 h). 10 µL of sample were taken at 30 min, 1 h, 1.5 h, 2 h, 15 h, 20 h, and 24 h for stability measurements using HPLC (Agilent Technologies, 1200 series, Phenomenex column, BioSep ™ 5 µm SEC-s 4000 500 Å LC Column 300 x 7.8 mm, with 0.1 M sodium phosphate buffer, pH 7.2, isocratic run, 1 ml/min, 20 - 30 min).

IMMUNOHISTOCHEMISTRY

Immunohistochemistry was performed on 5 µm paraffin-embedded tissue sections as described previously [3] using the following antibodies: GFP (632381, Takara 1: 250), poly-GA (1A12, IgG1 mouse, purified and biotinylated, 1:500), 1x Anti-HA high Affinity Rat monoclonal antibody clone 3F10 (11867423001, Roche), recombinant anti-mouse IgG2a antibody [RM107] (ab190463, Abcam). After deparaffinization and dehydration, heat-induced antigen retrieval was performed with citrate buffer (pH 6) for 20 min in the steamer. Slides were then blocked and incubated with primary antibody overnight at 4°C. Slides were washed and detected with the DCS supervision 2 Kit (DCS innovative diagnostic-system) according to the manufacturer's instructions. Bright-field images were taken on a Leica DMi8 fluorescence microscope (Leica).

STATISTICAL ANALYSIS OF SUVRs FROM PET/CT IMAGES

The results (Two-way ANOVA) revealed that genotype alone has a significant effect in CTX ($F(1,14) = 22.92$, $p = 0.0003$) and HIP ($F(1,14) = 20.34$, $p = 0.0005$) on tracer uptake. Additionally, time shows a significant correlation with tracer uptake in CTX ($F(1.717, 24.04) = 8.710$, $p = 0.0021$) and HIP ($F(1.835, 25.69) = 14.11$, $p = 0.0001$. A significant interaction effect between genotype and time in the CTX ($F(2,28) = 0.7942$, $p = 0.4618$) and HIP (($F(2,28) = 0.3210$, $p = 0.7281$) could not be observed. Pairwise Sidak's multiple comparison tests were conducted to examine differences between the genotype at each time point for each brain region (Fig. 3d). We found that there were statistically significant differences in tracer uptake between the genotype in CTX at 2 h p.i. ($p = 0.0416$), at 20 h p.i. ($p = 0.0011$) and at 40 h p.i. ($p = 0.0106$), and in HIP at 20 h p.i. ($p = 0.0065$) and at 40 h p.i. ($p = 0.0181$). No significant differences were observed at 2 h p.i. ($p = 0.0637$) in HIP.

SUPPLEMENTAL FIGURES

FIG. S1 ARSENAZO SPECTROMETRIC ASSAY

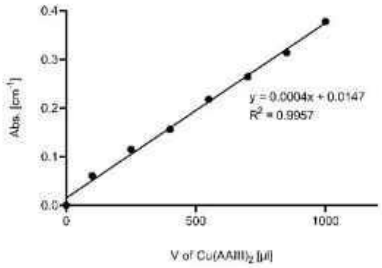

Validation of Lambert Beer's law. The adsorption was measured at different concentrations of $Cu(AAIII)_2$ in a solution of 0.15 M NH_4OAc at pH 7.0 in a 1.0 mL cuvette using a UV-Vis spectrophotometer. Linear regression, $R^2 = 0.9957$.

FIG. S2 HPLC AND RADIO-TLC

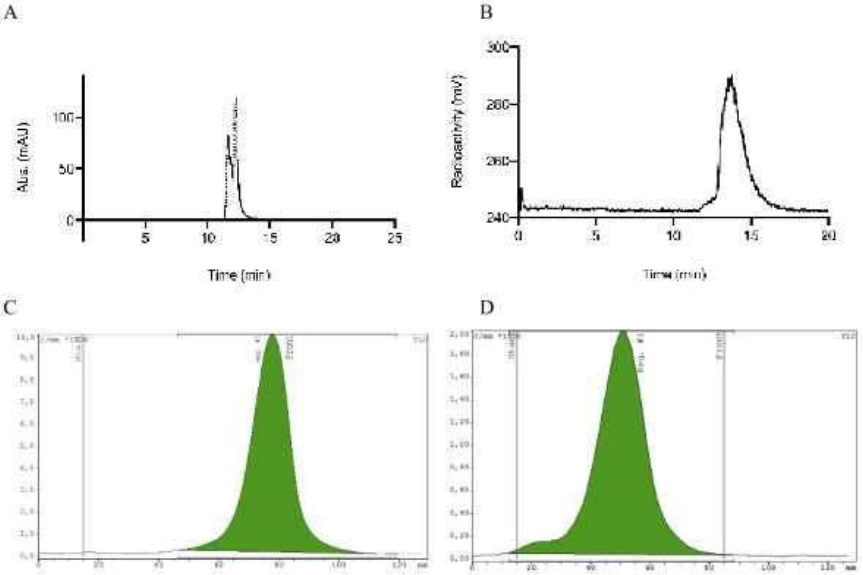

(A) HPLC chromatogram of *p*-NCS-benzyl-NODAGA, R_t = 13.6 to 14.2 min at 280 nm (UV channel). (B) HPLC chromatogram of [^{64}Cu]Cu-NODAGA, R_t = 13.8 min (radio channel). (C) Radio-TLC of [^{64}Cu]$CuCl_2$ on ITLC-SG chromatography paper, R_f = 0.9. (D) Radio-TLC of [^{64}Cu]Cu-NODAGA on ITLC-SG chromatography paper, R_f = 0.5.

FIG. S3 POLY-GA IMMUNOASSAY

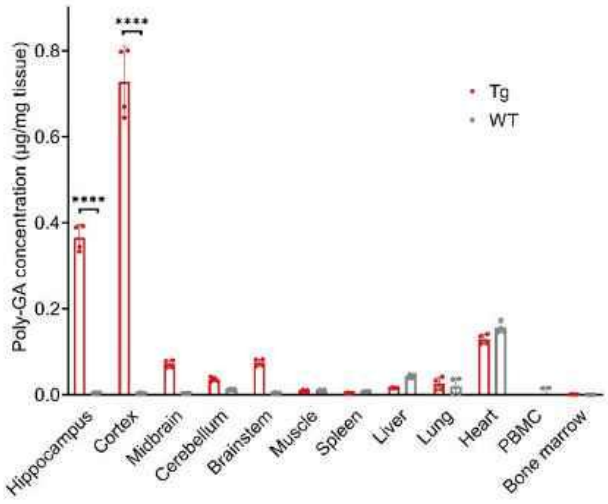

The poly-GA immunoassay was performed to measure poly-GA in different tissue of GA-CFP mice as described previously with slight modification (Zhou et al, 2020). Mouse tissue samples were homogenized in 400µl to 600µl of RIPA buffer (137 mM NaCl, 20 mM Tris pH 7.5, 10% glycine, 1% Triton X-100, 0.5% Na-deoxycholate, 0.1% SDS, 2 mM EDTA, protease and phosphatase inhibitors, benzonase nuclease) using homogenizer (Precellys). Samples were incubated with shaking at 4°C for 20 min and centrifuged at 13,000 g for 10 min at 4°C. Supernatant was then collected for immunoassay analysis and protein concentration was determined by Bradford assay. Streptavidin Gold multi-array 96-well plates were incubated with biotinylated anti-GA clone 1A12 overnight at 4°C and blocked with 1% BSA, 0.05% Tween 20 in PBS for 1 h. Equal amounts of samples were added in duplicate wells for 1.5 h, followed by 1.5 h incubation with the secondary sulfo-tag labeled α-GA clone 1A12. Serial dilution of recombinant RR-$(GA)_8$-RR in blocking buffer was used to generate a standard curve. The intensity of emitted light upon electrochemical stimulation was measured using the MSD QuickPlex 520, and the background was corrected by the average response obtained from blank wells. Data are given as mean ± SD, unpaired t-test, $p \leq 0.0001$.

FIG. S4 SUV SCALED PET IMAGES

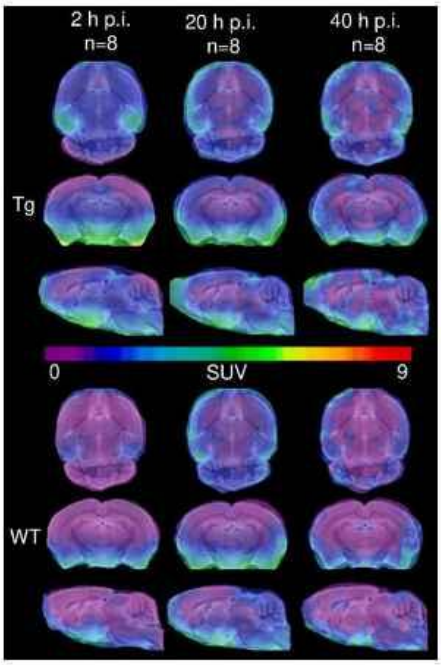

Tracer uptake in brains of Tg and WT mice at 2 h p.i. (left), 20 h p.i. (center) and 40 h p.i. (right) expressed as standard uptake values (SUV).

FIG. S5 CNS EXPOSURE OF THE 1A12 ANTIBODY

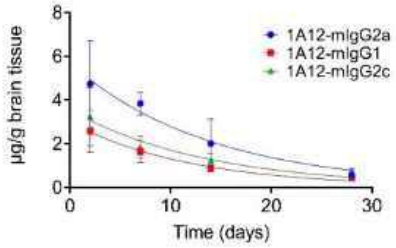

Study Design

The pharmacokinetics of 1A12 antibodies was investigated in plasma and brain of C57BL/6JOlaHsd mice (male, 3-6 animals/group). Mice were administered a single dose (30 mg/kg s.c.) of 1A12 antibodies of different IgG isotypes (IgG1, IgG2a, IgG2c). Sampling times for plasma were 0.5 h, 6 h, 1 d, 2 d, 3 d, 7 d, 14 d, 21 d, 28 d p.i. and for brain tissue 2 d, 7 d, 14 d and 28 d p.i. (compare Table S3). Before tissue collection mice were perfused with PBS. Samples were analyzed by anti-DPR ELISA using GST-$(GA)_{15}$ antigen.

Anti-DPR ELISA

Plasma samples were diluted with 0.1% Tween in PBS (1:50000 – 1:1000000), brain was homogenized into 10 × v/w, and concentration was adjusted to 10-14 mg/mL (1:10-1:40 dilution with 0.1% Tween in PBS). 96-well covalent binding plates (Thermo Fisher Scientific) were coated overnight at 4°C with 10 ng GST-$(GA)_{15}$ per well. After 1 hour blocking (PBS with 2% BSA and 0.1% Tween-20), serial dilutions of plasma or brain tissue samples of 1A12 antibodies (mIgG1, mIgG2a, mIgG2c, 4-9000 pg/mL) were added to the wells, incubated for 2 hours on a shaker, and detected after a 1-hour incubation on a shaker with HRP-conjugated antibodies (rabbit anti-mouse IgG1-HRP, dilution 1:10000; goat anti-mouse IgG2a-HRP, 1:1000; goat anti-mouse IgG2c-HRP, 1:10000). Signals were developed using Pierce™ TMB Substrate Kit (Thermo Fisher Scientific) and detected via spectrophotometry at 450 nm.

SUPPLEMENTAL TABLES

TABLE S1 POLY-GA IMMUNOASSAY DATA

Poly-GA concentration µg/mg tissue	**Tg**	**WT**
Hippocampus	0.365 ± 0.026	0.004 ± 0.001
Cortex	0.728 ± 0.072	0.004 ± 0.001
Midbrain	0.072 ± 0.008	0.003 ± 0.000
Cerebellum	0.036 ± 0.005	0.012 ± 0.001
Brainstem	0.075 ± 0.007	0.004 ± 0.001
Muscle	0.009 ± 0.002	0.009 ± 0.002
Spleen	0.004 ± 0.001	0.007 ± 0.001
Liver	0.016 ± 0.001	0.043 ± 0.004
Lung	0.025 ± 0.013	0.019 ± 0.017
Heart	0.129 ± 0.010	0.156 ± 0.011
PBMC	-0.006 ± 0.003	0.001 ± 0.015
Bone marrow	0.001 ± 0.000	0.000 ± 0.000

TABLE S2 BIODISTRIBUTION DATA 20 h AND 40 h p.i.

SUV Mean ± SD	**20 h**		**40 h**	
	Tg	**WT**	**Tg**	**WT**
Brain	0.16 ± 0.01	0.14 ± 0.03	0.13 ± 0.02	0.13 ± 0.02
Heart	1.35 ± 0.24	1.34 ± 0.21	1.08 ± 0.28	1.11 ± 0.10
Kidney	1.41 ± 0.25	2.24 ± 0.76	1.35 ± 0.25	1.48 ± 0.14
Pancreas	0.76 ± 0.15	0.72 ± 0.12	0.65 ± 0.13	0.53 ± 0.07
Spleen	1.84 ± 0.63	1.75 ± 0.14	2.83 ± 0.30	1.41 ± 0.25
Muscle	0.24 ± 0.04	0.26 ± 0.06	0.27 ± 0.04	0.23 ± 0.06
Bone	1.04 ± 0.25	0.75 ± 0.07	1.76 ± 0.98	0.67 ± 0.26
Lung	2.40 ± 0.25	2.35 ± 0.06	2.41 ± 0.28	1.81 ± 0.32
Liver	1.88 ± 0.61	2.62 ± 0.64	2.06 ± 0.28	2.55 ± 0.30
Blood	4.97 ± 0.74	5.20 ± 0.76	4.55 ± 1.05	3.46 ± 1.13

TABLE S3 PHARMAKOKINETIC DATA OF THE 1A12 ANTIBODY

Drug	**Tissue**	**C_{max} (µg/ml, µg/g)**	**C_{last} (µg/ml, µg/g)**	**AUC_{48-672} (h×µg/ml, h×µg/g)**	**$t_{1/2z}$ (h)**	**$K_{p,\ brain}$ (AUC_{48-672})**
1A12-mIgG1	Brain	2.57 ± 0.97	0.43 ± 0.04	742	272	0,024
	Plasma	121 ± 38	13 ± 2	31107	202	
1A12-mIgG2a	Brain	4.73 ± 1.97	0.57 ± 0.29	1549	183	0,034
	Plasma	159 ± 28	7 ± 12	45632	121	
1A12-mIgG2c	Brain	3.23 ± 1.33	0.77 ± 0.06	975	411	0,016
	Plasma	215 ± 27	29 ± 1	62522	239	

REFERENCES

(1) Mori, K., Arzberger, T., Grässer, F. A., Gijselinck, I., May, S., Rentzsch, K., Weng, S.-M., Schludi, M. H., van der Zee, J., Cruts, M., Van Broeckhoven, C., Kremmer, E., Kretzschmar, H. A., Haass, C.,Edbauer, D. (**2013**) Bidirectional transcripts of the expanded C9orf72 hexanucleotide repeat are translated into aggregating dipeptide repeat proteins, *Acta Neuropathol. 126*, 881-893. doi:https://doi.org/10.1007/s00401-013-1189-3.

(2) Mori, K., Weng, S.-M., Arzberger, T., May, S., Rentzsch, K., Kremmer, E., Schmid, B., Kretzschmar, H. A., Cruts, M., Van Broeckhoven, C., Haass, C.,Edbauer, D. (**2013**) The C9orf72 GGGGCC Repeat Is Translated into Aggregating Dipeptide-Repeat Proteins in FTLD/ALS, *AAAS Sel. Symp. 339*, 1335-1338. doi:https://doi.org/10.1126/science.1232927

(3) Zhou, Q., Mareljic, N., Michaelsen, M., Parhizkar, S., Heindl, S., Nuscher, B., Farny, D., Czuppa, M., Schludi, C., Graf, A., Krebs, S., Blum, H., Feederle, R., Roth, S., Haass, C., Arzberger, T., Liesz, A.,Edbauer, D. (**2020**) Active poly-GA vaccination prevents microglia activation and motor deficits in a C9orf72 mouse model, *EMBO Mol Med 12*, e10919. doi:https://doi.org/10.15252/emmm.201910919.

9. Publication II

Theranostics 2024, Vol. 14, Issue 16 6319

IVYSPRING INTERNATIONAL PUBLISHER

Theranostics

2024; 14(16): 6319-6336. doi: 10.7150/thno.97149

Research Paper

PET imaging of microglia in Alzheimer's disease using copper-64 labeled TREM2 antibodies

Monireh Shojaei[1*], Rebecca Schaefer[1*], Kai Schlepckow[2], Lea H. Kunze[1], Felix L. Struebing[2,3], Bettina Brunner[2], Michael Willem[2], Laura M. Bartos[1], Astrid Feiten[2,4], Giovanna Palumbo[1], Thomas Arzberger[3,5], Peter Bartenstein[1,6], Gian Carlo Parico[7], Dan Xia[7], Kathryn M. Monroe[7], Christian Haass[2,4,6], Matthias Brendel[1,2,6*✉], Simon Lindner[1*✉]

1. Department of Nuclear Medicine, University Hospital, LMU Munich, Munich, Germany.
2. German Center for Neurodegenerative Diseases (DZNE), Munich, Germany.
3. Center for Neuropathology and Prion Research, University Hospital, LMU Munich, Munich, Germany.
4. Metabolic Biochemistry, Biomedical Center (BMC), Faculty of Medicine, LMU Munich, Munich, Germany.
5. Department of Psychiatry and Psychotherapy, University Hospital, LMU Munich, Munich, Germany.
6. Munich Cluster of Systems Neurology (SyNergy), Munich, Germany.
7. Denali Therapeutics Inc, South San Francisco, CA, USA.

*Contributed equally.

✉ Corresponding authors: Simon Lindner: Marchioninistraße 15, 81377 Munich, Germany; email: simon.lindner@med.uni-muenchen.de, phone: +49 89 4400 69941. Matthias Brendel: Marchioninistraße 15, 81377 Munich, Germany; email: matthias.brendel@med.uni-muenchen.de, phone: +49 89 4400 74610.

Received: 2024.04.09; Accepted: 2024.09.11; Published: 2024.09.30

Abstract

Triggering receptor expressed on myeloid cells 2 (TREM2) plays an essential role in microglia activation and is being investigated as a potential therapeutic target for modulation of microglia in several neurological diseases. In this study, we present the development and preclinical evaluation of ^{64}Cu-labeled antibody-based PET radiotracers as tools for non-invasive assessment of TREM2 expression. Furthermore, we tested the potential of an antibody transport vehicle (ATV) that binds human transferrin receptor to facilitate transcytosis of TREM2 antibody-based radiotracers to the CNS and improve target engagement.

Methods: A TREM2 antibody with an engineered transport vehicle (ATV:4D9) and without (4D9) were covalently modified with *p*NCS-benzyl-NODAGA and labeled with copper-64. Potency, stability, and specificity were assessed *in vitro* followed by *in vivo* PET imaging at the early 2 h, intermediate 20 h, and late imaging time points 40 h post-injection using a human transferrin receptor (hTfR) expressing model for amyloidogenesis (5xFAD;TfR$^{mu/hu}$) or wild-type mice (WT;TfR$^{mu/hu}$), and hTfR negative controls. Organs of interest were isolated to determine biodistribution by *ex vivo* autoradiography. Cell sorting after *in vivo* tracer injection was used to demonstrate cellular specificity for microglia and to validate TREM2 PET results in an independent mouse model for amyloidogenesis (App^{SAA};TfR$^{mu/hu}$). For translation to human imaging, a human TREM2 antibody (14D3) was radiolabeled and used for *in vitro* autoradiography on human brain sections.

Results: The ^{64}Cu-labeled antibodies were obtained in high radiochemical purity (RCP), radiochemical yield (RCY), and specific activity. Antibody modification did not impact TREM2 binding. ATV:4D9 binding proved to be specific, and the tracer stability was maintained over 48 h. The uptake of [^{64}Cu]Cu-NODAGA-ATV:4D9 in the brains of hTfR expressing mice was up to 4.6-fold higher than [^{64}Cu]Cu-NODAGA-4D9 in mice without hTfR. TREM2 PET revealed elevated uptake in the cortex of 5xFAD mice compared to wild-type, which was validated by autoradiography. PET-to-biodistribution correlation revealed that elevated radiotracer uptake in brains of 5xFAD;TfR$^{mu/hu}$ mice was driven by microglia-rich cortical and hippocampal brain regions. Radiolabeled ATV:4D9 was selectively enriched in microglia and cellular uptake explained PET signal enhancement in App^{SAA};TfR$^{mu/hu}$ mice. Human autoradiography showed elevated TREM2 tracer binding in the cortex of patients with Alzheimer's disease.

Conclusion: [^{64}Cu]Cu-NODAGA-ATV:4D9 has potential for non-invasive assessment of TREM2 as a surrogate marker for microglia activation *in vivo*. ATV engineering for hTfR binding and transcytosis overcomes the blood-brain barrier restriction for antibody-based PET radiotracers. TREM2 PET might be a versatile tool for many applications beyond Alzheimer's disease, such as glioma and chronic inflammatory diseases.

Keywords: TREM2, ATV:4D9, copper-64, microglia, PET

Introduction

Neurodegenerative diseases (NDD) are characterized by the gradual degeneration and loss of neurons within the central nervous system (CNS) [1, 2]. This neuronal damage leads to cognitive and movement dysfunctions observed in diseases like Alzheimer's (AD) and Parkinson's disease (PD). NDDs are also associated with the accumulation and misfolding of amyloidogenic proteins [3, 4]. In addition, neuroinflammation is observed in many NDDs and chronic inflammation contributes significantly to the development and pathology of the disease [5, 6].

Microglia, the main resident macrophages in the CNS, exhibit different phenotypes depending on the specific conditions of the brain microenvironment [6]. In the healthy brain, resting microglia persist in a homeostatic state and play a crucial role in immune surveillance and maintaining brain homeostasis [7, 8]. Upon a challenge such as accumulating amyloid pathology, microglia activate a defensive gene network [9, 10]. Microglia that respond to pathological challenges, have a common transcriptional signature and are referred to as disease-associated microglia (DAM) [7, 11-13]. Under persistent inflammatory conditions, microglia can remain activated losing their normal protective function and mediate chronic inflammatory processes [13-15]. The dysregulation of the immune defense in the CNS seems to be an important factor in NDD progression and particularly emerges at an early stage in TREM2 late-onset Alzheimer's disease variants, even before other NDD pathologies come into play [8, 9, 16]. Early diagnosis of NDDs is of utmost importance for patients as more therapy options can be applied [16]. In this respect, positron emission tomography (PET) is an ideal diagnostic tool as it is a non-invasive imaging technology with high sensitivity and allows for accurate target detection and quantification at spatial resolution. Further, regional analyses of the entire brain by PET can identify heterogeneous target profiles and can detect regional changes by longitudinal imaging schemes.

The most investigated PET biomarker for activated microglia in the brain and spinal cord is the 18 kDa translocator protein (TSPO). TSPO is associated with the activation of microglia and is regarded as a distinctive characteristic of neuroinflammation. The initial tracer developed to target TSPO, (*R*)-[^{11}C]PK11195, had certain drawbacks such as challenging radiochemistry, a short half-life and a low signal-to-noise ratio [17, 18]. Among others, [^{18}F]GE-180 is a widely used third-generation TSPO tracer with longer half-life, improved brain uptake and higher affinity [19]. Although TSPO imaging provides useful clinical information, several drawbacks remain. Allelic variants in human populations with low TSPO binding hamper a broader use of TSPO PET for *in vivo* diagnostics [20]. Furthermore, TSPO PET signals are not entirely specific to microglia, as TSPO is also expressed by endothelial cells, astrocytes and neurons [21]. Limitations of TSPO as an imaging approach for microglia led us to investigate other biomarkers that are more microglia-specific, such as Triggering receptor expressed on myeloid cells 2 (TREM2) [16, 22, 23].

TREM2 is a type-1 transmembrane protein that plays an essential role in microglial functions [24, 25] and their transition from a homeostatic state to DAM [7, 11, 26, 27]. Microglia combat amyloid pathology by phagocytosis and encapsulation of amyloid plaques [11, 24, 28, 29]. TREM2 polymorphism, which has been reported previously as risk factor for late-onset AD (LOAD) [30, 31], impairs microglial activation leading to reduced Aβ plaque clearance [24, 32]. Therapeutic approaches targeting TREM2 largely focus on agonistic antibodies stimulating protective microglial functions in the brain during the preclinical stage of AD [33]. However, methods to assess direct target engagement are not available yet, and utilize an indirect measure of binding to soluble TREM2 present in biofluids [12]. TSPO PET is not a suitable biomarker as it does not selectively represent TREM2-activated microglia. Thus, TREM2 PET would allow regional assessment of the TREM2-positive DAM subset and could be used as a novel biomarker to directly monitor CNS target engagement in preclinical studies and clinical trials.

Previous attempts to image TREM2 highlight the challenges in the CNS. In contrast, in the periphery, Shi *et al.* reported ^{68}Ga-labeled COG1410, an ApoE-derived peptide that targets TREM2 on

tumor-associated macrophages (TAMs) for the diagnosis of gastrointestinal tumors [34], and ^{124}I- and ^{99m}Tc-labeled antibody fragments showing potential for targeting human TREM2 in gastric carcinoma [35] and lung cancer [36]. For neuroimaging, Meier *et al.* presented a ^{124}I-labeled TREM2 antibody with a linked single-chain variable fragment that binds transferrin receptor to target TREM2 in AD mice. Using PET, the tracer was unable to image TREM2 *in vivo*, but could visualize TREM2 *ex vivo* [8].

In our study, we focused on the development of a TREM2-targeting PET imaging agent based on the monoclonal agonistic antibody 4D9 that binds to the mouse TREM2 stalk region, *N*-terminal to the cleavage site of TREM2 [12], and competes with α-secretase-mediated shedding and subsequent release of soluble TREM2 (sTREM2) [12, 37-40]. TREM2 agonism is mediated by: 1) TREM2 stabilization at the cell surface by lowering TREM2 shedding; 2) Activation of phospho-SYK signaling downstream of TREM2 by antibody-mediated receptor cross-linking. These mechanisms lead to an increase in phagocytic uptake of Aβ fibrils by primary mouse microglia *in vitro* [12]. To overcome the blood-brain barrier (BBB), which effectively restricts the delivery of antibodies into the brain, we engineered an ATV-enabled version of the mouse 4D9 antibody for use in our studies [41]. The ATV selectively binds to the apical domain of the human transferrin receptor (hTfR) and facilitates active transport of the antibody into the brain parenchyma via TfR-mediated transcytosis within endothelial cells [41, 42].

We developed and evaluated two new radiotracers targeting TREM2, [^{64}Cu]Cu-NODAGA-ATV:4D9 and [^{64}Cu]Cu-NODAGA-4D9, i.e. the antibody chemically modified with the chelator NODAGA, which forms a complex with the radioisotope copper-64. These tracers enabled us to image TREM2 in the CNS of an AD mouse model. The effectiveness of tracer delivery into the brain was strongly enhanced by the ATV technology. Cell sorting after *in vivo* radiotracer injection proved microglia-specific binding of ATV:4D9.

Materials and Methods

Detailed information on materials and experimental procedures are provided in the supplemental materials, including patient tissue, chemicals, p-SYK assay, arsenazo spectrophotometric assay, HPLC and TLC chromatograms, stability measurements, biodistribution data, PET images, Cohen's d calculations, tracer uptake data from regression analysis and flow cytometry data.

Animals

All animal studies were carried out according to the German animal protection regulations and protocols, and a veterinarian was in charge of them (ROB-55.2-2532.Vet_02-21-156; ROB-55.2-2532.Vet_02-19-26). The animals were obtained from The Jackson Laboratory, Sacramento, CA, United States and Charles River, Sulzfeld, Germany. Mice were housed in isolated ventilated cages (IVC) at 23-26 °C and humidity levels of 55-60%, including a 12-hour light/dark cycle. Prior to the study, all mice were given at least two weeks of care and acclimatization. Following mouse cohorts were selected:

1A) 5xFAD (B6.Cg-Tg(APPSwFILon,PSEN1*M146L*L286V)6799Vas/Mmjax), (n = 18, female = 9, male = 9)

1B) C57BL/6J, hereafter referred to as wild-type (WT) mice (n = 18, female = 8, male = 10)

2A) 5xFAD;TfR$^{mu/hu}$ (hemizygous for 5xFAD, homozygous for TfR$^{mu/hu}$), (n = 18, female = 9, male = 9)

2B) WT;TfR$^{mu/hu}$ (homozygous for TfR$^{mu/hu}$), (n = 18, female = 9, male = 9)

3) App^{SAA};TfR$^{mu/hu}$ (homozygous for App^{SAA}, homozygous for TfR$^{mu/hu}$), (n = 4)

Mice from cohorts 2A, 2B and 3 express human transferrin receptors, with the apical domain of human TfR knocked into the mouse TfR locus. This approach preserves the native murine transferrin binding domain and retains the majority of the transferrin receptor gene [42]. Mice from cohort 1 and 2 were age-matched (6-7 months) and included males and females. Cohort 3 mice (all male) were 19.7 ± 1.1 months old to ensure high TREM2 expression levels.

Antibody modification

4D9, ATV:4D9 and ATV:ISO conjugation to the chelator 2,2'-(7-(1-carboxy-4-((4-isothiocyanatobenzyl) amino)-4-oxobutyl)-1,4,7-triazonane-1,4-diyl)diacetic acid (p-NCS-benzyl-NODAGA) was done as follows:

3.8 mg (7.3 µmol) *p*-NCS-benzyl-NODAGA was dissolved in a metal-free phosphate buffer (0.1 M, 100 µL, pH 8.5) and added to the antibody mixture (4 mg antibody in 1 mL PBS buffer). After the incubation of the reaction mixture (overnight, 4 °C) [43], the mixture was purified by Microcon® centrifugal filter units (Ultracel® 30 kDa, 0.5 mL, Merck Millipore Ltd). The HPLC (Agilent Technologies, 1200 series) quality control was done using a Phenomenex column (BioSep TM 5 m SEC s 4000 500 Å LC Column 300 × 7.8 mm) and sodium phosphate buffer (0.1 M, pH 7.2, 1 mL/min) as eluent. NODAGA-4D9 and bispecific NODAGA-ATV:4D9 antibodies revealed a retention time of 10.3 min and 10.4 min respectively in the UV channel at 280 nm. The number of chelators per

antibody was determined using a spectrometric arsenazo assay as reported elsewhere [44].

Radiolabeling

NODAGA-4D9, NODAGA-ATV:4D9 or NODAGA-ATV:ISO antibodies (100-200 µg) were incubated with 100-200 MBq of [^{64}Cu]$CuCl_2$ in a metal-free ammonium acetate buffer (0.1 M, pH 5.6, 42 °C). After the reaction (30 min), the buffer was changed to phosphate-buffered saline (ABX) via ultrafiltration (14000 g, 4 °C). Quality control was performed by radio-TLC (ITLC-SG glass microfiber chromatography paper, Agilent Technologies, Folsom, CA) and radio-HPLC (BioSep TM 5 m SEC s 4000 500 Å LC column 300 × 7.8 mm, 0.1 M sodium phosphate buffer, pH 7.2, 1 mL/min). The retention factors in the TLC analysis were R_f ([^{64}Cu]Cu-NODAGA-4D9) = 0.0, R_f ([^{64}Cu]Cu-NODAGA-ATV:4D9) = 0.0, R_f ([^{64}Cu]$CuCl_2$) = 1.0, R_f ([^{64}Cu]Cu-NODAGA) = 0.5. [^{64}Cu]Cu-NODAGA-4D9 and [^{64}Cu]Cu-NODAGA-ATV:4D9 revealed a retention time of 10.3 and 10.7 minutes, respectively, by radio-HPLC.

Autoradiography

Brain sections of 5xFAD;TfR$^{mu/hu}$ and WT;TfR$^{mu/hu}$ mice were pretreated with buffer solution (50 mM Tris-HCl, pH 7.4, RT, 10 min) and then incubated with [^{64}Cu]Cu-NODAGA-ATV:4D9 (0.1 to 0.5 MBq) in phosphate buffer (pH 7, 60 min, RT). To verify specificity, a 1000-fold excess of unlabeled ATV:4D9 antibody (2000 µg) was added to 2 MBq of [^{64}Cu]Cu-NODAGA-ATV:4D9 (1.3 µg), and each section was incubated with 0.1 MBq of the tracer. Sections were rinsed first with cold Tris-HCl + 5% ethanol (pH 7.4, 1 × 5 min, 4 °C), distilled water (RT, 5 sec.) and then dried for 1 h at RT. For *ex vivo* autoradiography, one brain hemisphere was isolated, fixed with polymer gel (Tissue-Tek® O.C.T. Compound), and frozen at -20 °C. The brain tissues were cut in sagittal sections of 20 µm thickness using a Leica CM 1860 cryostate. All brain sections were exposed to a phosphor imaging plate and placed in a dark cassette. After 24 to 30 h exposure, the plate was scanned by a CR-Reader (CR35 BIO, DÜRR MEDICAL). The Aida Image Analyzer v 450 software was used for image analysis. A manually drawn region of interest (ROI) was placed in the cerebellum as a pseudo-reference tissue. After background subtraction, intensity normalization of all sections was performed by calculation of brain-to-cerebellum (CBL) ratios. Human brain sections were deparaffinized (xylene, xylene:EtOH 1:1, 100% EtOH, 95% EtOH, 70% EtOH, 50% EtOH, dH_2O, 3 min each), unmasked via antigen retrieval (Tris/EDTA pH 9.0, heat-induced in a pressure cooker, boiling for 3 min), blocked (5% BSA in PBS/Triton (0.25% v/v) for 1 h at RT), incubated with [^{64}Cu]Cu-NODAGA-14D3 (0.1 MBq or an added 1000-fold excess of unlabeled 14D3 antibody, 1 h at RT), and washed (PBS, 3×10 min). Subsequent steps were carried out in accordance with the methodology for murine brain sections. For human brain sections, white matter (WM) was used as the internal reference region, and cortex-to-white matter ratios are given.

Small animal PET

Mice from cohorts 1 and 2 were administered 13.1 ± 3.2 MBq [^{64}Cu]Cu-NODAGA-4D9 (n = 29) or 10.2 ± 1.3 MBq [^{64}Cu]Cu-NODAGA-ATV:4D9 (n = 30) (corresponding to 8.1 ± 1.1 µg and 10.2 ± 1.9 µg per mouse) in 150 µL phosphate buffer by intravenous injection through the tail vein. Table 1 indicates which tracer was applied to which individual mouse model. The PET scan (Mediso Nanoscan PET/CT, 70 kvp/650 µA, exposure time 300 ms, Helical 1.0 pitch, with coincidence mode 1-5 in 1 scan position) was conducted 2 h, 20 h, and 40 h post-injection (n = 8 per time point, 30 min emission time). The mice were continuously anesthetized with isoflurane during the scan. PET images were reconstructed using the Tera Tomo™ 3D algorithm (4 iterations and 6 subsets). The resulting images were analyzed using PMOD (version 3.5; PMOD Technologies Ltd.). The CT and PET images of each mouse were aligned and registered to the magnetic resonance imaging (MRI) mouse brain atlas. An average image was generated for each group at 2 h, 20 h and 40 h p.i. Volumes-of-interest (VOIs) were manually placed in the hippocampus and cortex to assess tracer uptake by calculating the percentage of injected dose per gram of tissue (%ID/g). Cohen's d was calculated to estimate effect sizes. PET-to-biodistribution correlation analysis was performed using whole-brain voxel-wise SPM analysis (Wellcome Department of Cognitive Neurology, London, UK) in MATLAB (v2011-R2016) [45]. The correlation was considered significant if $p < 0.05$. Data-driven cluster VOIs from SPM analysis were used for regression coefficient calculation and comparison of tracer uptake (%ID/g) between all groups.

Mice from cohort 3 were administered 38.1 ± 1.2 MBq [^{64}Cu]Cu-NODAGA-ATV:4D9 (n = 4) (corresponding 30.5 ± 1.0 µg per mouse) into the tail vein. PET imaging was performed and analyzed at 20 h p.i. following the protocol described above. PET signal increases of cohort 3 (in contrast to WT;TfR$^{mu/hu}$ of cohort 2B) were quantitatively compared with radioactivity of isolated microglial cells (single cell Radiotracing (scRadiotracing), see

detailed description below) in all four individual App^{SAA};$TfR^{mu/hu}$ mice. To this end, 7.4×10^6 microglia built the basis for estimation of microglia cell numbers in aged App^{SAA};$TfR^{mu/hu}$ mice.

Table 1: Tracers used for individual mouse lines.

Cohort	Mouse line	Tracer
1A	5xFAD	[^{64}Cu]Cu-NODAGA-4D9
1B	WT	[^{64}Cu]Cu-NODAGA-4D9
2A	5xFAD;$TfR^{mu/hu}$	[^{64}Cu]Cu-NODAGA-ATV:4D9
2B	WT;$TfR^{mu/hu}$	[^{64}Cu]Cu-NODAGA-ATV:4D9 [^{64}Cu]Cu-NODAGA-ATV:ISO
3	APP^{SAA};$TfR^{mu/hu}$	[^{64}Cu]Cu-NODAGA-ATV:4D9

Biodistribution

After PET acquisition, a solution of ketamine 10% (m/v) and xylazine 2% (m/v) in 0.9% NaCl was administered intraperitoneally to each mouse. Mice were intracardially perfused using 40 mL PBS buffer. At 2 h and 20 h post-injection, the brain (either the whole brain or one hemisphere) was collected, and the tracer enrichment was measured using a gamma counter (n = 6). Additionally, a whole-body biodistribution study was carried out at 40 h post-injection (n = 6), including brain, liver, lungs, heart, blood, kidneys, muscle, pancreas, spleen and bone. The tracer enrichment in the individual organs was measured using a gamma counter (HIDEX AMG Gamma Counter, version 1.6.0.0, counting window from 450 to 570 keV; 1 min; including mass measurement) and expressed as %ID/g.

Single cell Radiotracing

App^{SAA};$TfR^{mu/hu}$ mice were injected with 38.1 ± 1.2 MBq [^{64}Cu]Cu-NODAGA-ATV:4D9 (corresponding 30.5 ± 1.0 µg per mouse) into the tail vein. At 20 h p.i., the mice were euthanized via cervical dislocation and the mouse brains were removed and briefly washed and stored in cold Dulbrecco's phosphate-buffered saline (D-PBS). The brains were placed in a 10 mm petri dish containing 2 mL cold D-PBS under a dissecting microscope (Leica Microsystems M80, Wetzlar, Germany), and meninges were gently detached from the skull and removed using fine forceps (Dumont, 11254-20). Immunomagnetic cell separation (MACS) was performed as described previously [46, 47] with slight modifications. Adult Brain Dissociation Kit, mouse and rat (Miltenyi Biotec, 130-107-677) was used for brain tissue dissociation according to the supplier's instructions. The brains were cut into small pieces and dissociated with enzyme mix 1 and 2 using gentleMACS Octo Dissociator with heaters (Miltenyi Biotec, 130-096-427). The cell suspension was applied to a preconditioned 70 µm MACS SmartStrainer (Miltenyi Biotec, 130-110-916) and debris was removed by using Debris Removal Solution. Microglia were labeled using CD11b MicroBeads (Miltenyi Biotec, 130-049-601) and subsequently separated using two-column sorting on the autoMACS Pro Separator (Miltenyi Biotec, 130-092-545). CD11b-enriched and depleted fractions were collected, centrifuged (4 °C, 400 × g, 10 min) and the supernatant was aspirated. The cell pellets were resuspended in 100 µL cold D-PBS and incubated with 2 µL anti-mouse CD11b antibody, (Miltenyi Biotec, 130-113-238) at 4 °C for 10 minutes in the dark. Cells were washed with 1 mL D-PBS, centrifuged (4 °C, 300 × g, 10 min), and the supernatant was aspirated. The cell pellets of the CD11b-enriched fractions were resuspended in 500 µL D-PBS and the depleted fractions were resuspended in 1 mL D-PBS. Radioactivity of the samples was measured in a gamma counter (Hidex AMG Automatic Gamma Counter, Mainz, Germany) and decay corrected to 20 h post tracer injection. Absolute cell counts and purity of CD11b-enriched cell pellets in each sample were acquired on a MACSQuant10 analyzer (Miltenyi Biotec, 130-105-100).

Immunohistochemistry of human brain sections

Human brain tissue for *in vitro* autoradiography and images of stained human brain sections were provided by the Center of Neuropathology and Prion Research, LMU Munich, Germany. Approval for *ex vivo* tissue staining was obtained from the local ethics committee (application number 19–244).

AD brain tissues were taken from six patients with following characteristics: ABC score A3/B3/C3 (which is an amyloid β score modified from Thal of phases 4 or 5, neurofibrillary tangles stage modified from Braak of stage V or VI, and neuritic plaque score modified from CERAD of score frequent), 63-88 years old, n = 4 female and n = 2 male. The TREM2 polymorphisms were unknown for all cases.

Immunohistochemistry, including counter-staining with hematoxylin, was performed on 5 µm thick paraffin sections using a Ventana BenchMark ULTRA (Roche) according to the instructions of the manufacturer. Primary antibody was mouse anti-TREM2 (diluted 1:200; Merck MABN1534). Pretreatment for antibody was boiling in CC2 buffer (Roche) for 48 min. The diaminobenzidine/peroxidase based detection system was optiView (Roche). Immunohistochemical stains were scanned with a Zeiss Axio Scan.Z1 using a 20x objective. Zeiss blue and ImageJ were used for quantification. TREM2 was quantified as the % area.

Statistical analysis

GraphPad Prism (version 9) was used to carry out the statistical analysis. Biodistribution and PET (frontal cortex and hippocampus and data-driven regions) were analyzed using one-way ANOVA and Tukey's post hoc test to adjust for multiple comparisons. Ratios of autoradiography experiments (*in vitro* and *ex vivo*) were compared between genotypes using an unpaired t-test. A regression analysis between biodistribution and PET was performed using statistical parametric mapping (SPM) using SPM12 routines (Wellcome Department of Cognitive Neurology, London, UK) implemented in MATLAB (version 2016). Individual %ID images were subject to a linear regression analysis with biodistribution tracer uptake as a vector in the pooled cohort of all genotypes. Data-driven clusters were selected at a threshold of $p < 0.005$ uncorrected, $k > 20$ voxels. Pearson's coefficient of determination (R^2) was calculated for VOI-based PET to biodistribution correlation analysis. Similarity of quantitative brain radiotracer uptake and microglial radiotracer uptake was assessed with a paired t-test.

Results

^{64}Cu-labeling of 4D9 and ATV:4D9 antibodies yields radiotracers of high stability

Antibodies were modified via covalent attachment of the *p*-NCS-benzyl-NODAGA chelator to lysine residues on the surface of the antibody. 1-2 chelators were bound to the antibodies as determined with an arsenazo assay (Figure S1) [44]. This spectrophotometric assay allows for the determination of the chelator-antibody ratio. The number of chelators per antibody should be kept on a low level to avoid alterations of biodistribution and impairment of the antibody's immunoreactivity. High radiochemical purity (RCP), radiochemical yield (RCY) and specific activity (A_s) were obtained for both [^{64}Cu]Cu-NODAGA-4D9 and [^{64}Cu]Cu-NODAGA-ATV:4D9 (Table 2). The RCP was determined using radio-TLC, radio-HPLC and SDS-PAGE (Figure S2). The results confirmed that there was no chelator-bound or free [^{64}Cu]$CuCl_2$ present in the injectable solutions.

The stability of [^{64}Cu]Cu-NODAGA-ATV:4D9 was assessed by incubation in murine plasma for 48 h at 37 °C. Samples were taken and analyzed by SEC-HPLC showing that the tracer remained stable over 48 h. We performed *ex vivo* stability analysis using SDS-PAGE and radio-TLC of plasma samples from [^{64}Cu]Cu-NODAGA-ATV:4D9 and [^{64}Cu]Cu-NODAGA-4D9 injected WT mice 20 h p.i. SDS-PAGE revealed intact radiotracer and the absence of any other proteins that might have been radiolabeled via trans-chelation whereas radio-TLC confirmed the absence of unbound copper-64 (Figure S3).

Table 2: Results of ^{64}Cu-labeling. RCY and RCP are given as mean (range), A_s as mean ± SD. The RCP was obtained from radio-TLC quality control measurements.

Tracer	RCY (%)	RCP (%)	A_s (MBq/µg)
[^{64}Cu]Cu-NODAGA-4D9	69.4 (60.0-85.7) (n = 5)	98.5 (95.8-99.5) (n = 4)	1.4 ± 0.3 (n = 4)
[^{64}Cu]Cu-NODAGA-ATV:4D9	67.1 (61.3-72.6) (n = 6)	97.3 (90.5-100) (n = 6)	1.0 ± 0.2 (n = 6)

RCY: radiochemical yield; RCP: radiochemical purity; A_s: specific activity.

Antibody-based TREM2 tracer exhibits full functionality and high specificity

Brain sections (4 mice, 12 sections) from 5xFAD;TfR$^{mu/hu}$ mice were used for *in vitro* autoradiography using [^{64}Cu]Cu-NODAGA-ATV:4D9 (Figure 1A). The images revealed high tracer enrichment in the frontal cortex and the hippocampus, where strong microglial activation occurs in this mouse model [48-51]. When brain sections from 5xFAD;TfR$^{mu/hu}$ (5 mice, 20 sections) were treated with [^{64}Cu]Cu-NODAGA-ATV:4D9 in the presence of 1000-fold excess of cold ATV:4D9 antibody, tracer accumulation was significantly reduced, indicating that the tracer binds specifically to its target (Figure 1A). Compared to 5xFAD;TfR$^{mu/hu}$ mice, the brain sections (3 mice, 11 sections) of WT;TfR$^{mu/hu}$ mice revealed less pronounced tracer enrichment in cortical and hippocampal areas and a rather equally distributed accumulation pattern (Figure 1A). Quantitative readout from *in vitro* experiments revealed a cortex-to-cerebellum ratio of 1.35 ± 0.14 (mean ± SD) for 5xFAD;TfR$^{mu/hu}$ and 0.80 ± 0.13 for WT;TfR$^{mu/hu}$ mice (Figure 1B).

To investigate if the antibody modification affects TREM2 binding, NODAGA-modified antibodies were compared with the native antibodies using a p-SYK signaling assay (Figure 1C). Antibody-mediated activation of p-SYK signaling downstream of TREM2 was not reduced, indicating that TREM2 binding is not impaired. Higher potency of ATV:4D9 compared to 4D9 antibodies can be explained by the concomitant expression of hTfR on TREM2-DAP12 overexpressing HEK293 cells enabling increased cross-linking of TREM2 and enhanced endosomal signaling [41].

hTfR-mediated transcytosis facilitates higher brain uptake of ^{64}Cu-labeled TREM2 antibodies in mice

Brain uptake of [^{64}Cu]Cu-NODAGA-ATV:4D9

and [^{64}Cu]Cu-NODAGA-4D9 was measured after intracardial perfusion using gamma counting at 2 h, 20 h and 40 h p.i. (n = 6) (Figure 2A). Brain uptake of [^{64}Cu]Cu-NODAGA-ATV:4D9 in 6-7 months old 5xFAD;TfR$^{mu/hu}$ mice was up to 4.6-fold higher compared to [^{64}Cu]Cu-NODAGA-4D9 in age-matched 5xFAD mice (Figure 2B, Table S1) and remained at a high level over 20 h. Similar results were obtained when comparing WT;TfR$^{mu/hu}$ and WT mice at the same age. To break down the relative proportion of hTfR binding to total binding, we determined brain uptake of [^{64}Cu]Cu-NODAGA-ATV:ISO (isotype, reflecting hTfR binding only) and [^{64}Cu]Cu-NODAGA-ATV:4D9 (reflecting hTfR and TREM2 binding) in WT;TfR$^{mu/hu}$ mice 20 h p.i. via biodistribution (Figure S4). We found that 80% of the signal in the brain is attributed to hTfR binding.

Whole-body biodistribution (Figure 2C, Table S2) of perfused mice was performed at 40 h p.i. (n = 6). High tracer uptake was observed in bone, spleen, liver and kidney. Uptake levels were low in heart, pancreas and lung, and lowest in muscle. With the exception of the brain, 5xFAD;TfR$^{mu/hu}$ mice tended to exhibit lower tracer uptake in all organs compared to 5xFAD mice. The same trend could be observed in WT;TfR$^{mu/hu}$ mice compared to WT mice (except bone). Blood retention assessed before perfusion was considerably higher in mice without hTfR expression compared to 5xFAD;TfR$^{mu/hu}$ and WT;TfR$^{mu/hu}$ mice. In summary, biodistribution data confirm the hypothesis that organ biodistribution was mainly driven by TfR binding.

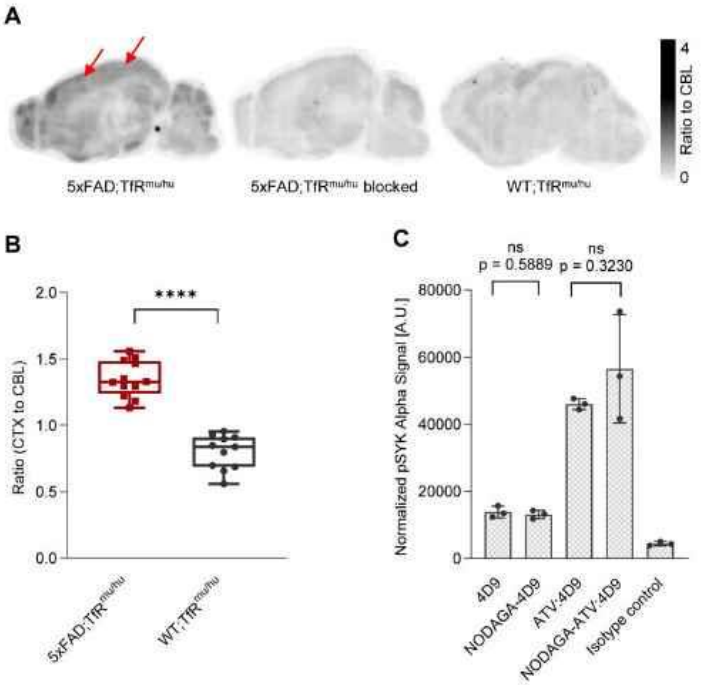

Figure 1: *In vitro* autoradiography experiments. (**A**) Sagittal sections show autoradiography results from 5xFAD;TfR$^{mu/hu}$ brain, upon blocking with 1000-fold excess cold ATV:4D9 antibody, and WT;TfR$^{mu/hu}$ brain. Arrows indicate increased uptake of [^{64}Cu]Cu-NODAGA-ATV:4D9 in the frontal cortex. (**B**) The brain sections of 5xFAD;TfR$^{mu/hu}$ (4 mice, 12 sections) revealed higher cortex-to-cerebellum ratio compared to WT;TfR$^{mu/hu}$ (3 mice, 11 sections) mice. Unpaired t-test, $p < 0.0001$ (****), boxplot min to max. (**C**) Quantification of pSYK levels by AlphaLISA (normalized to protein concentration) in lysates from HEK293 Flp-In cells that stably overexpress mouse TREM2 and mouse DAP12. Cells were stimulated with 4D9, NODAGA-4D9, ATV:4D9, NODAGA-ATV:4D9, and an isotype control. The experiment was performed once including n = 3 technical replicates. Unpaired t-test, (n = 3, mean ± SD).

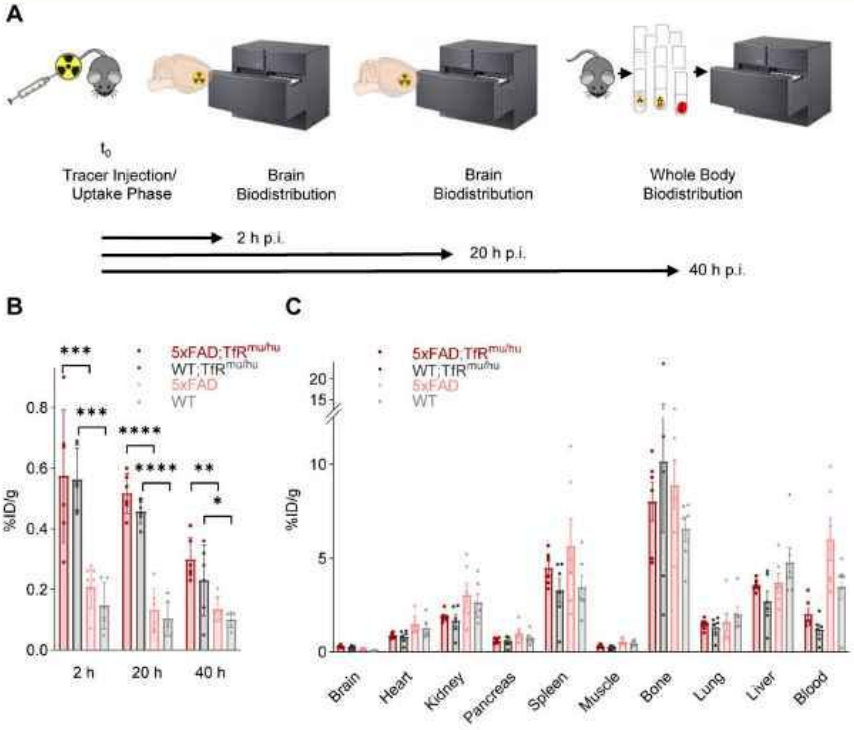

Figure 2: Biodistribution experiments. (**A**) Schematic representation of the biodistribution workflow. (**B**) Decay-corrected brain uptake of [^{64}Cu]Cu-NODAGA-ATV:4D9 in 5xFAD;TfR$^{mu/hu}$ and WT;TfR$^{mu/hu}$, as well as [^{64}Cu]Cu-NODAGA-4D9 in 5xFAD and WT mice, was determined after intracardial perfusion at 2 h, 20 h, and 40 h p.i. One-way ANOVA/Tukey's multiple comparison test, $p \leq 0.05$ (*), $p \leq 0.01$ (**), $p \leq 0.001$ (***), and $p \leq 0.0001$ (****), mean ± SD. Non-decay-corrected data are presented in Figure S5. (**C**) Whole-body biodistribution at 40 h p.i.

TREM2 PET shows elevated signals in mice with increased TREM2 levels

Next, we investigated if ^{64}Cu-labeled 4D9 and ATV:4D9 antibodies are suitable radiotracers to visualize TREM2 *in vivo* using small animal PET imaging at 2 h, 20 h and 40 h p.i. (Figure 3A). Figure 3B presents group average PET images generated 20 h p.i. (images at 2 h p.i. and 40 h p.i. are shown in Figure S6). Regions of interest (VOIs) were predefined in the frontal cortex and the hippocampus based on the Mirrione atlas [52, 53] with adjustment to exclude spill-in signals from skull, which was characterized by high biodistribution. A significantly higher uptake was found in the frontal cortex (Figure 3C) and in the hippocampus (Figure 3D) at 20 h p.i. of 5xFAD;TfR$^{mu/hu}$ compared to WT;TfR$^{mu/hu}$ mice at 6-7 months of age (Tables S3 and S4). Considering the fraction of hTfR-related binding determined by biodistribution, which is comparable in both animal models [41], it is evident that the tracer is able to unveil TREM2-dependent signal enhancement. Elevated TREM2 PET signals were consistent with higher TREM2 protein levels found in 5xFAD brain lysates compared to wild-type controls (Figure S7). No difference in tracer uptake was observed at the 40 h p.i. time point, likely due to a decay-related decrease in signal-to-noise ratios. In addition, effect sizes expressed as Cohen's d were high comparing 5xFAD;TfR$^{mu/hu}$ vs WT;TfR$^{mu/hu}$ and 5xFAD;TfR$^{mu/hu}$ vs 5xFAD mice at 2 h and 20 h p.i. in cortex and 20 h p.i. in the hippocampus (Table S5). A comparison of ^{64}Cu-labeled ATV:4D9 to a compilation of PET data from multiple TSPO tracers revealed that TREM2 PET resulted in higher %ID/g and SUVR ratios than TSPO PET (Figure S8, Tables S6 and S7).

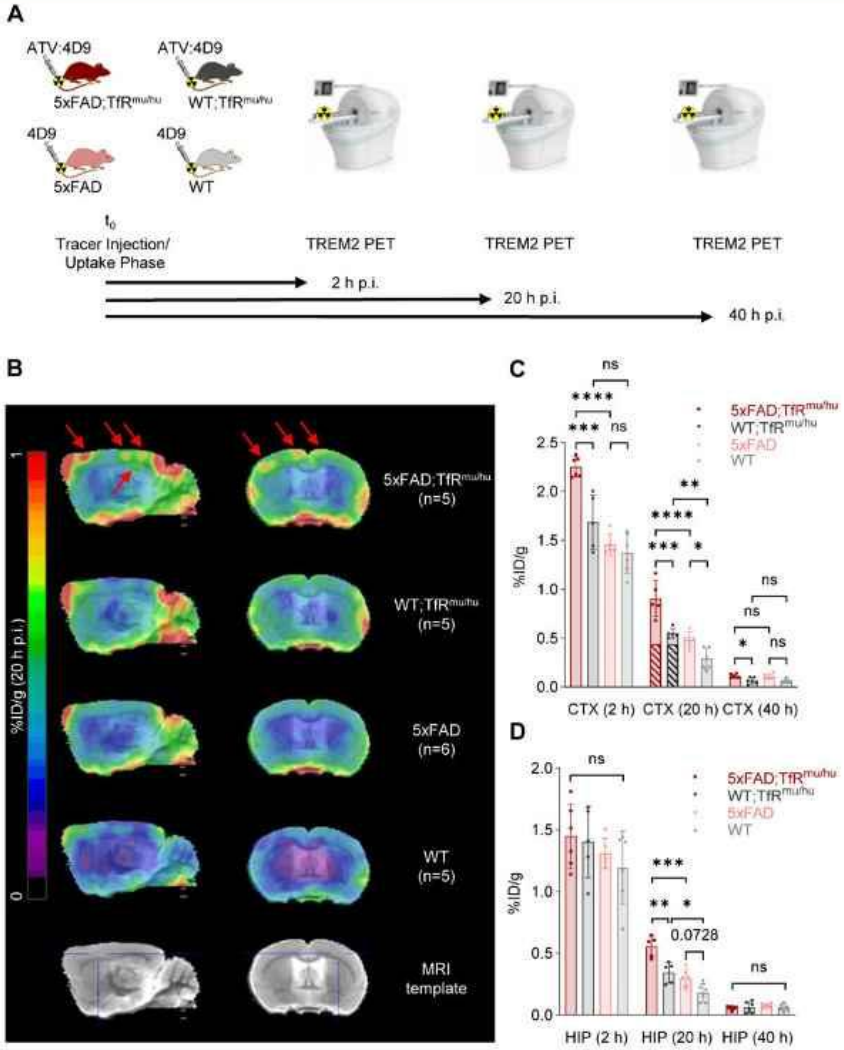

Figure 3: TREM2 PET imaging in 5xFAD and wild-type mice. (**A**) Schematic representation of the PET/CT workflow. (**B**) Group average PET images of 5xFAD;TfR$^{mu/hu}$, 5xFAD, WT;TfR$^{mu/hu}$ and WT mouse brains at 20 h p.i. overlaid on an MRI template. Red arrows indicate highest uptake in the frontal cortex and the hippocampus of 5xFAD;TfR$^{mu/hu}$ animals. (**C, D**) Quantitative tracer uptake (%ID/g) in predefined VOIs of the frontal cortex (CTX) and the hippocampus (HIP). Striped bars illustrate the fraction of hTfR-related binding determined by biodistribution using ^{64}Cu-labeled ATV:ISO (Figure S4). One-way ANOVA/Tukey's multiple comparison test, $p \leq 0.05$ (*), $p \leq 0.01$ (**), $p \leq 0.001$ (***), and $p \leq 0.0001$ (****), mean ± SD.

To address spill-in from skull into cortex due to limited spatial resolution of small animal PET, we performed data-driven identification of cortical brain regions where PET signals are derived from TREM2 target engagement. To this end, we performed a voxel-wise correlation analysis between brain biodistribution and brain uptake in TREM2 PET. Statistical maps derived from regression analyses revealed cluster VOIs, which were most strongly associated with uptake values from biodistribution. Accordingly, elevated radiotracer uptake in whole brain of 5xFAD;TfR$^{mu/hu}$ mice was driven by voxels in the frontal cortex (Figure 4A), which showed an excellent linear correlation with biodistribution,

pronounced at 20 h p.i. (Figure 4B and Table S8). In this optimized target region, 5xFAD;TfR$^{mu/hu}$ mice revealed significantly higher uptake than the WT;TfR$^{mu/hu}$ controls at 20 h p.i. (Figure 4C and Table S9). At 2 h p.i., the correlation between biodistribution and PET was also high, but only a trend towards higher uptake in 5xFAD;TfR$^{mu/hu}$ compared to WT;TfR$^{mu/hu}$ mice was detected. The correlation between biodistribution and PET was lower at 40 h p.i. and no statistically significant differences were obtained. Altogether, these data supported 20 h p.i. as the most robust time point for TREM2 PET imaging with antibody-labeled tracers.

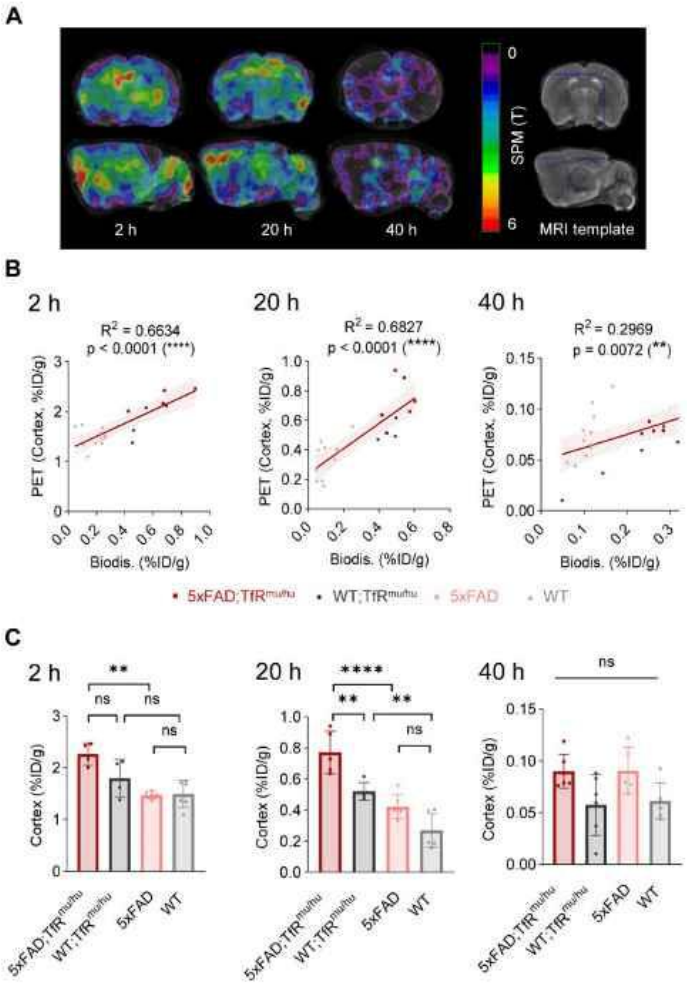

Figure 4: PET-to-biodistribution associations. (**A**) Images from voxel-wise regression analysis of biodistribution brain uptake with PET images using statistical parametric mapping (SPM). Color scale shows TREM2 PET voxels with highest correlation to biodistribution in red using all four genotypes. (**B**) TREM2 PET signals in data-driven cortical cluster VOIs derived from the regression analysis in correlation with brain uptake from biodistribution at 2 h, 20 h and 40 h p.i. (linear regression, $\alpha = 0.05$, 95% CI), (**C**) Group comparison of TREM2 PET results in data-driven cortical cluster VOIs across genotypes. One-way ANOVA/Tukey's multiple comparison test, $p \leq 0.01$ (**), $p \leq 0.001$ (***), and $p \leq 0.0001$ (****), mean ± SD.

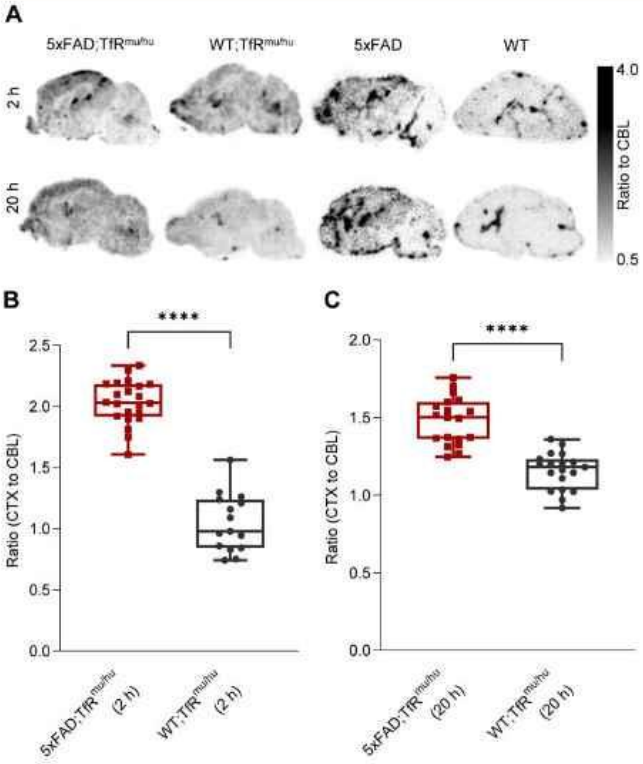

Figure 5: *Ex vivo* autoradiography confirmation of regional TREM2 PET signals. (**A**) *Ex vivo* autoradiography of 5xFAD;TfR$^{mu/hu}$, WT;TfR$^{mu/hu}$, 5xFAD and WT brain sections at 2 h and 20 h p.i. (**B,C**) Higher cortex-to-cerebellum ratios were observed in 5xFAD;TfR$^{mu/hu}$ mice compared to WT;TfR$^{mu/hu}$ mice at the 2 h p.i. time point (5xFAD;TfR$^{mu/hu}$: 2 mice, 22 sections; WT;TfR$^{mu/hu}$: 2 mice, 15 sections; unpaired t-test, $p < 0.0001$ (****), boxplot min to max) and the 20 h p.i. time point (5xFAD;TfR$^{mu/hu}$: 2 mice, 19 sections; WT;TfR$^{mu/hu}$: 2 mice, 19 sections; unpaired t-test, $p < 0.0001$ (****), boxplot min to max).

Ex vivo autoradiography confirms the regional TREM2 PET distribution pattern of tracer uptake in the brain

Ex vivo autoradiography was performed from brain sections of perfused 5xFAD;TfR$^{mu/hu}$, WT;TfR$^{mu/hu}$, 5xFAD and WT mice at 2 h and 20 h p.i. as a validation experiment for *in vivo* patterns as obtained by TREM2 PET imaging (Figure 5A). The cortex-to-cerebellum ratio was calculated as a quantitative readout. Obtained CTX/CBL values were 2.04 ± 0.18 (mean ± SD) for 5xFAD;TfR$^{mu/hu}$, 1.05 ± 0.24 for WT;TfR$^{mu/hu}$ mice at 2 h p.i. ($p < 0.0001$) (Figure 5B), and 1.48 ± 0.15 for 5xFAD;TfR$^{mu/hu}$ and 1.16 ± 0.12 for WT;TfR$^{mu/hu}$ mice at 20 h p.i. ($p < 0.0001$) (Figure 5C). Patterns of tracer retention in autoradiography mirrored data-driven clusters of highest TREM2 tracer binding in PET.

scRadiotracing confirms high cellular selectivity of [^{64}Cu]Cu-NODAGA-ATV:4D9 for microglia and validates TREM2 PET in a second mouse model of amyloidogenesis

To validate the cellular origin (i.e. microglial specificity) of TREM2 PET signals in the brain, we applied a novel technique of cell sorting after PET tracer injection and PET imaging [47] in an independent mouse model of amyloidogenesis, i.e. App^{SAA};TfR$^{mu/hu}$ mice (Figure 6A and Figure S9) [54]. With this approach, we detected [^{64}Cu]Cu-NODAGA-ATV:4D9 in microglial and non-microglial cells of the brain at the time of PET imaging. This mouse model has a humanized apical domain of TfR where the chimeric receptor is referred to as TfR$^{mu/hu}$, in addition to the presence of β-amyloid plaques with concomitant increase in TREM2 levels [54]. TREM2 PET revealed an enhanced signal predominantly in

frontal cortex and hippocampal brain regions of aged App^{SAA};TfR$^{mu/hu}$ mice (Figure 6B, group-average PET images are shown in Figure S10). Immunomagnetic cell sorting allowed isolation of a microglia-enriched fraction with 98% CD11b$^+$ and microglia-depleted cell pellets with nearly complete absence of CD11b$^+$ cells (Figure 6C-D). App^{SAA};TfR$^{mu/hu}$ mice showed a 3.3-fold increase in microglia in whole brain (Figure 6E). Gamma emission recordings indicated a strong signal in the microglia-enriched fraction but negligible signal in the microglia-depleted fraction, confirming the cellular specificity of [^{64}Cu]Cu-NODAGA-ATV:4D9 binding to microglia (Figure 6F). Furthermore, we estimated the microglia-related increase in brain radiotracer uptake in PET of App^{SAA};TfR$^{mu/hu}$ vs. WT;TfR$^{mu/hu}$ controls. To do so, microglial cell number was multiplied by the activity per microglial cell from scRadiotracing experiments to obtain the signal derived from microglial uptake in App^{SAA};TfR$^{mu/hu}$ mice (dark red bars in Figure 6G), which explains 67% of the PET signal increase in App^{SAA};TfR$^{mu/hu}$ mice compared to WT;TfR$^{mu/hu}$ controls (Figure 6G).

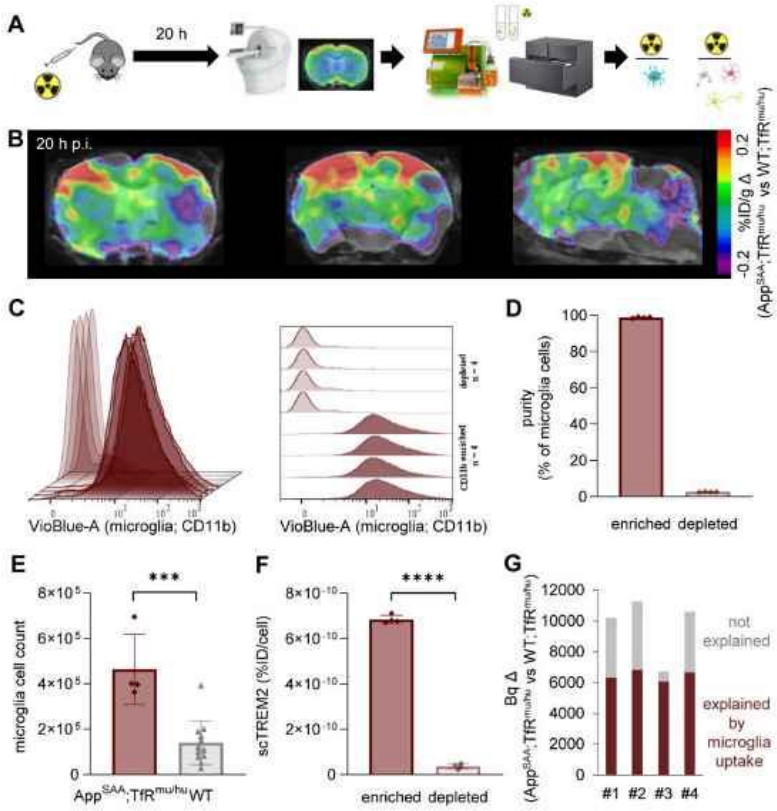

Figure 6: scRadiotracing demonstrates specificity of [^{64}Cu]Cu-NODAGA-ATV:4D9 to microglia. (**A**) Experimental workflow, including TREM2 PET at 20 h p.i., brain dissociation and cell sorting as well as flow cytometry and gamma emission recording to calculate radioactivity per cell (microglia = turquoise, astrocyte = pink, neuron = yellow, oligodendrocyte = gray). (**B**) TREM2 PET results are shown as axial (frontal cortex, hippocampus) and sagittal (forebrain, hindbrain) regional difference maps (n = 4 App^{SAA};TfR$^{mu/hu}$ mice compared to n = 5 WT;TfR$^{mu/hu}$ of Fig.3) projected upon an MRI template. (**C, D**) Flow cytometry indicates high purity of CD11b-positive cells in microglia-enriched fractions and absence of CD11b-positive cells in the microglia-depleted fractions of n = 4 individual App^{SAA};TfR$^{mu/hu}$ mice. Data are shown as mean fluorescence intensity. (**E**) Relative cellular abundance of microglial cells in App^{SAA};TfR$^{mu/hu}$ (n = 4) mice compared to WT (n = 12) mice. Unpaired t-test, p = 0.0002 (***), mean ± SD. (**F**) TREM2 radiotracer uptake of microglia-enriched vs microglia-depleted (i.e. mixed fraction of neurons, astrocytes, oligodendrocytes) fractions in App^{SAA};TfR$^{mu/hu}$ mice, confirming high specificity to microglia. Unpaired t-test, p < 0.0001 (****), mean ± SD. (**G**) Estimation of the PET signal percentage which is explained by microglial uptake as a product of microglial abundance and microglial tracer uptake per cell. Based on (**E**) and 7.4 × 10^6 microglia in WT brains taken from literature, we calculated 24.7 × 10^6 microglia in App^{SAA};TfR$^{mu/hu}$ brains.

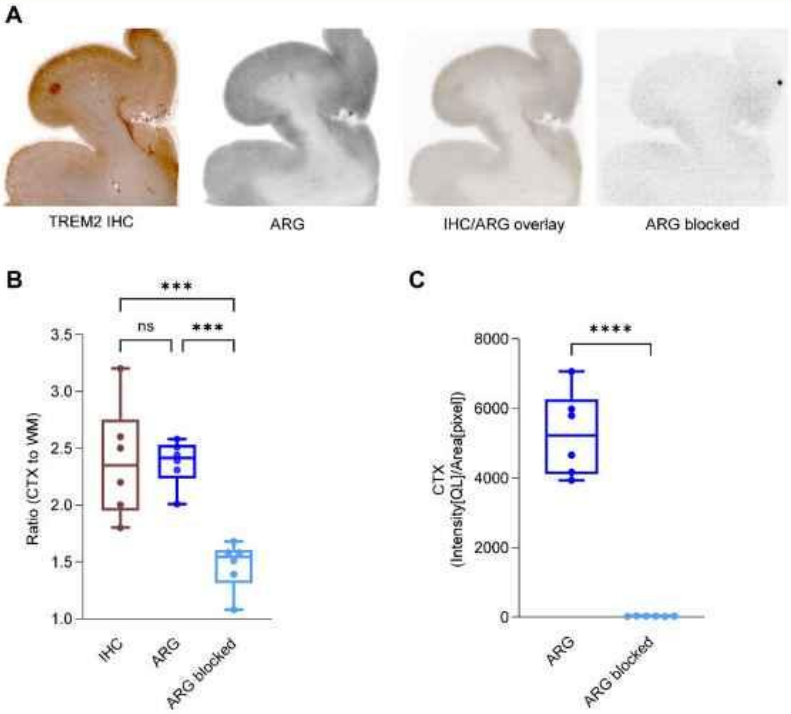

Figure 7: [^{64}Cu]Cu-NODAGA-14D3 ARG signal represents TREM2 IHC signal in Alzheimer's disease patients. (**A**) Representative TREM2 immunohistochemistry (IHC) and *in vitro* autoradiography (ARG) of frontal brain sections derived from a patient with Alzheimer's disease (AD) revealed cortical binding of [^{64}Cu]Cu-NODAGA-14D3. TREM2 IHC and tracer binding in ARG co-localized. Autoradiography of a blocked brain slice demonstrated a negligible signal. (**B**) Cortex-to-white matter ratios were consistent in IHC and ARG and significantly higher than in blocked ARG (One-way ANOVA/Tukey's multiple comparison test, $p \leq 0.001$ (***), boxplot min to max). (**C**) ARG-blocking resulted in a cortical signal reduction (unpaired t-test, $p < 0.0001$ (****), boxplot min to max).

Labeled anti-human TREM2 antibody indicates potential for translation to clinical TREM2 PET imaging

We next investigated the translation of our promising preclinical findings into clinical applications. We conducted immunohistochemistry and *in vitro* autoradiography on human brain sections of patients with AD. The 14D3 antibody [55] targeting human TREM2 (Figure S11) was analogously modified with the chelator NODAGA and labeled with copper-64 (RCP > 99%, measured by radio-TLC, n = 2) in accordance with the techniques and methods established for 4D9. 14D3 exclusively binds full-length TREM2 at the cleavage site of human TREM2, in contrast to 4D9, which also binds sTREM2. Further, this antibody was not ATV-enabled, hence does not contain a binding site for the human TfR. TREM2 immunohistochemistry and [^{64}Cu]Cu-NODAGA-14D3 autoradiography co-localized in adjacent sections, with enriched binding in the cortex but not in the subcortical white matter of the brain sections (Figure 7A), suggesting high regional TREM2 expression associated with AD pathology, including Aβ plaque and Tau protein (Figure S12). No significant differences between cortex-to-white matter ratios in immunohistochemistry (2.35 ± 0.46, median ± SD) and autoradiography (2.42 ± 0.18, median ± SD) confirmed the consistency of both methods to detect TREM2 (Figure 7B). Autoradiography of blocked brain sections with a 1000-fold excess of the 14D3 antibody demonstrated an almost negligible signal (Figure 7C) and only a minimal unspecific binding (Figure 7A). These preliminary findings suggest that the ATV-enabled 14D3 antibody might be a potential candidate that can be tested in models for subsequent translation of TREM2 PET imaging into the clinic.

Discussion

TREM2 has emerged as a highly relevant molecular biomarker and therapeutic target in various

indications [56], since it is associated with critical functions of macrophages and microglia in disease. We present a proof of concept for a novel imaging tool to detect TREM2-expressing microglia by direct target engagement of TREM2 antibodies. We developed two radiotracers using ATV:4D9 and 4D9 antibodies targeting mouse TREM2 [12, 41]. We showed that the potency of both tracers remained unchanged after chemical modification, and [^{64}Cu]Cu-NODAGA-ATV:4D9 was stable in murine plasma for 48 hours. The specificity of [^{64}Cu]Cu-NODAGA-ATV:4D9 was proven in a blocking experiment in the presence of an excess amount of unlabeled antibody. *In vivo* TREM2 PET revealed significantly elevated TREM2 binding in a mouse model of amyloid pathology compared to wild-type mice, which was validated by *ex vivo* autoradiography. Moreover, the cellular specificity of [^{64}Cu]Cu-NODAGA-ATV:4D9 binding to microglia was demonstrated by cell sorting after *in vivo* radiotracer injection. Preliminary *in vitro* testing of an analogously copper-64 labeled human TREM2 antibody revealed promising binding patterns on AD post-mortem tissue.

In vitro autoradiography with brain sections of 5xFAD;TfR$^{mu/hu}$ mice at 6-7 months of age showed elevated [^{64}Cu]Cu-NODAGA-ATV:4D9 uptake in frontal cortex and hippocampus compared to brain sections of WT;TfR$^{mu/hu}$ mice. Amyloid pathology in 5xFAD mice manifests as early as 2 months of age and results in a high plaque load in cortical and hippocampal brain regions, which is accompanied by strong microglial activation [48, 49, 51]. Therefore, high TREM2 levels are present in these brain regions, which is in line with our autoradiography results. When testing the developed radiotracers *in vivo*, [^{64}Cu]Cu-NODAGA-ATV:4D9 revealed a 4-fold higher brain uptake in 5xFAD;TfR$^{mu/hu}$ than [^{64}Cu]Cu-NODAGA-4D9 in 5xFAD mice and 4.6-fold higher brain uptake in WT;TfR$^{mu/hu}$ than [^{64}Cu]Cu-NODAGA-4D9 in WT mice at 20 h p.i. due to the BBB penetrance of the ATV technology [41], which improved tracer delivery into the brain [41, 42]. A literature review shows that the radiotracer concentration in the brain in our study is higher than what has been reported for bispecific constructs using TREM2 or Aβ targeting antibodies and scFv8D3 for TfR binding [8, 57]. Even higher brain concentrations were achieved with smaller TfR-targeting bispecific tribody constructs with more than 1 %ID/g, which is comparable to small molecule tracers [58].

Transferrin receptor 1 (TfR1) expression is not limited to brain endothelial cells, where it plays a vital role in the uptake of transferrin-bound iron into cells across the BBB, but TfR1 is also expressed in bone marrow [41]. Notably, peripheral biodistribution studies revealed high tracer uptake in bone. While TREM2 is expressed in microglia in the CNS, it is also present on peripheral myeloid cells. Consequently, TfR and TREM2 binding may be the cause of high tracer accumulation in the bone marrow. Accordingly, tissue retention of the copper-64 labeled 4D9 antibody in mice without hTfR apical domain knock-in was higher in most organs and blood than copper-64 labeled ATV:4D9 in mice with hTfR knock-in. We conclude that a considerable amount of ATV:4D9 localizes in bone due to TfR binding compared to 4D9 antibody, reducing blood retention and bioavailability of residual ATV:4D9 antibody to other organs. A tracer application requires only a minimal quantity of antibody, and thus, further investigations are needed to fully understand the impact of TfR binding for ATV:4D9 at these low doses.

Next, we evaluated if both tracers are suitable for TREM2 PET imaging with a focus on different time points and target region optimization. We were able to verify higher PET-derived tracer uptake in the frontal cortex and the hippocampus of 5xFAD;TfR$^{mu/hu}$ mice compared to WT;TfR$^{mu/hu}$ controls. 20 h p.i. emerged as a robust imaging time point since it allowed to detect differences between genotypes also in the hippocampus as a smaller and more challenging region compared to the frontal cortex. We also noticed spill-in from adjacent bone and endeavored to optimize our target regions by a data-driven approach using voxel-wise statistical parametric mapping. Here, PET-to-biodistribution correlation showed that elevated radiotracer uptake in whole brain of 5xFAD;TfR$^{mu/hu}$ mice was mostly driven by voxels in the deeper layers of the frontal cortex, and good correlation between both read-outs was achieved, especially at 20 h p.i. This indicated a high accuracy of regional PET quantification when a safety margin is considered at the edge of the brain, and the overall high correlation validated the reliability of PET imaging at that time point. hTfR-related signal represented 80% of the brain signal in WT;TfR$^{mu/hu}$ mice with low TREM2 expression levels. Given that hTfR expression is identical in 5xFAD;TfR$^{mu/hu}$ [41], it can be inferred that the significant increase in the PET signal in 5xFAD;TfR$^{mu/hu}$ cortex depends on TREM2. Thus, we speculate that biodistribution rather reflects hTfR-driven tracer uptake, whereas PET uncovers the activated DAM-driven brain retention in TREM2-enriched regions. Lacking biodistribution differences between genotypes at the group level appeared reasonable, since regional analysis by PET allows a local assessment of tracer uptake alterations, whereas biodistribution accounts for overall tracer uptake in the brain, including basal activity levels. It is

also noteworthy, that the fraction of TREM2 binding in the cortex of 5xFAD;TfR$^{mu/hu}$ mice is comparable in 5xFAD mice. Hence, ATV technology increases the retention of antibodies in the brain via hTfR binding, strongly increasing TREM2 signaling [41], but does not increase the relative proportion of TREM2 binding. The results of our small animal TREM2 PET investigation were confirmed by *ex vivo* autoradiography showing distinct differences in cortex-to-cerebellum ratios between 5xFAD;TfR$^{mu/hu}$ mice and WT;TfR$^{mu/hu}$ controls. Regional TREM2 PET sensitivity will increase in a human setting where the brain signal is less affected by adjacent structures due to higher PET resolution relative to the brain size.

Ultimately, we sought to prove the cellular selectivity of the novel TREM2 PET agents. In this regard, scRadiotracing has been shown to be a powerful methodology to disentangle cellular sources of PET signals over a variety of different cell types [46, 47]. This methodology was already applied for radiotracers, which are taken up and retained within the cell, such as [^{18}F]FDG and [^{18}F]GE-180. We showed that this also applies to ligands of membrane-bound targets on the cell surface. At this point, we cannot distinguish if the measured activity comes from the surface-bound tracer or from the internalized radioligand-receptor complex. Therefore, we showed high cellular specificity of the ATV:4D9 tracer targeting microglia. Microglial enrichment correlated well with the TREM2 PET signal in aged App^{SAA};TfR$^{mu/hu}$ mice. Thus, our cell sorting experiments provide strong evidence that TREM2 PET using ATV:4D9 is a powerful tool to monitor TREM2 on microglia.

While our preclinical data with ATV:4D9 are promising, translation into the clinic warrants a radiotracer which targets human TREM2. Hence, we prepared a radiotracer using the 14D3 antibody, which binds hTREM2 specifically (Figure S11). *In vitro* autoradiography experiments employing AD brain sections and [^{64}Cu]Cu-NODAGA-14D3 revealed a distinct detection primarily concentrated in the cortex, which overlaps with TREM2-expressing microglia and typical Aβ plaque and phosphorylated Tau protein deposits in the cortex. This is consistent with clustering of TREM2-positive microglia around amyloid plaques in both mice and humans [24, 32, 59].

Attempts to detect TREM2 via imaging in the CNS using PET have been reported previously using a bispecific antibody construct [8]. ^{124}I-labeled mAb1729 was used to target TREM2 and scFv8D3 for TfR-mediated transcytosis. The radiotracer showed good brain uptake and could detect TREM2 *ex vivo*. However, it failed to detect TREM2 *in vivo*. This was explained by high blood retention and possibly poor target binding due to TREM2 shedding and low TREM2 affinity. In our study, [^{64}Cu]Cu-NODAGA-ATV:4D9 revealed lower blood retention which could be attributed to a smaller antibody format compared to the mAb1729-scFv8D3 construct or target-mediated drug disposition. TREM2 agonist activity was not impaired compared to the native antibody (0.03 nM for ATV:4D9) [41], indicating preserved affinity and epitope upon radiotracer labeling.

The application of TREM2 PET imaging could extend beyond Alzheimer's disease to other brain conditions, notably leukodystrophies that are linked to microglial activation. The critical function of TREM2 is highlighted by the homozygous loss-of-function mutation that results in Nasu-Hakola disease, which is characterized by central microglial pathology [60, 61]. Leukodystrophies resulting from lysosomal or peroxisomal deficiencies also significantly affect microglia, resulting in dysfunctional myelination and white matter maintenance [62, 63]. It has been demonstrated that demyelination and the death of oligodendrocytes result in astrogliosis, microglial activation, and macrophage recruitment, with immune activation frequently occurring prior to white matter damage [64, 65]. While FDG PET has been used to examine cerebral glucose metabolism alterations [66-68], TREM2 PET could provide a novel approach for evaluating leukodystrophies given the pivotal role of microglia in their pathogenesis. Furthermore, TREM2 PET may prove valuable in assessing traumatic brain injury, considering the correlation between microglial activation and the progression to chronic traumatic encephalopathy and other related disorders [69, 70].

Some limitations have to be considered within this study. 4D9 not only targets membrane-bound TREM2, but also soluble TREM2 (sTREM2) [12, 37, 71]. It has to be clarified to what extent sTREM2 might trap the radiotracer, and if binding to diffusible sTREM2 facilitates clearance or deteriorates the spatial resolution of the PET images. In future, alternative TREM2 epitopes could be considered to optimize TREM2 as a radiotracer target. Our ongoing studies will concentrate on characterizing the specific role of TfR binding using PET and single cell Radiotracing [72]. Furthermore, longitudinal TREM2 PET imaging will be important to investigate if the radiotracer is able to image alterations of microglial activation during disease progression.

Conclusions

In conclusion, we present the first microglia-specific PET radiotracer, which proved suitable for imaging TREM2-associated activation of microglia in

the CNS in a mouse model of AD. We leveraged ATV technology to improve the efficiency of tracer delivery across the BBB. To pave the way for a human application, we performed preliminary experiments with a radiotracer targeting human TREM2. Results obtained from immunohistochemistry and *in vitro* autoradiography on brain sections of AD patients provide a strong rationale for future translation of this research into clinical applications. TREM2 PET imaging has great potential to verify target engagement and to monitor therapy response in antibody-based TREM2 agonistic interventions.

Abbreviations

AD: Alzheimer's disease; ARG: autoradiography; ATV: antibody transport vehicle; BBB: blood-brain barrier; CBL: cerebellum; CNS: central nervous system; CT: computed tomography; CTX: cortex; DAM: disease-associated microglia; HIP: hippocampus; HPLC: high performance liquid chromatography; hTfR: human transferrin receptor; IHC: immunohistochemistry; MACS: magnetic cell separation; MRI: magnetic resonance imaging; PD: Parkinson's disease; PET: positron emission tomography; RCP: radiochemical purity; RCY: radiochemical yield; ROI: region of interest; SDS-PAGE: sodium dodecyl sulfate polyacrylamide gel electrophoresis; scRadiotracing: single cell Radiotracing; SEC: size exclusion chromatography; SPM: statistical parametric mapping; TLC: thin layer chromatography; TREM2: Triggering receptor expressed on myeloid cells 2; TSPO: 18 kDa translocator protein; VOI: volume of interest.

Supplementary Material

Supplementary figures and tables.
https://www.thno.org/v14p6319s1.pdf

Funding

This work was supported by the Deutsche Forschungsgemeinschaft (DFG, German Research Foundation) with individual applications (ID 495961210, BR 4580/3-1, LI 3533/1-1) to SL and MB and under Germany's Excellence Strategy within the framework of the Munich Cluster for Systems Neurology (EXC 2145 SyNergy – ID 390857198 to CH and MB), by the DFG research unit FOR2858 (ID 403161218 to MB) and a Koselleck Project HA1737/16-1 (to CH).

Competing Interests

G.C.P., D.X., and K.M.M. are full-time employees and shareholders of Denali Therapeutics. The other authors have declared that no competing interest exists.

References

1. Amor S, Peferoen LA, Vogel DY, Breur M, van der Valk P, Baker D, et al. Inflammation in neurodegenerative diseases - an update. Immunology. 2014; 142: 151-66.
2. Przedborski S, Vila M, Jackson-Lewis V. Neurodegeneration: what is it and where are we? J Clin Invest. 2003; 111: 3-10.
3. Jucker M, Walker LC. Propagation and spread of pathogenic protein assemblies in neurodegenerative diseases. Nat Neurosci. 2018; 21: 1341-9.
4. Prusiner SB. Biology and genetics of prions causing neurodegeneration. Annu Rev Genet. 2013; 47: 601-23.
5. Heneka MT, Carson MJ, El Khoury J, Landreth GE, Brosseron F, Feinstein DL, et al. Neuroinflammation in Alzheimer's disease. Lancet Neurol. 2015; 14: 388-405.
6. Holtman IR, Raj DD, Miller JA, Schaafsma W, Yin Z, Brouwer N, et al. Induction of a common microglia gene expression signature by aging and neurodegenerative conditions: a co-expression meta-analysis. Acta Neuropathol Commun. 2015; 3: 31.
7. Krasemann S, Madore C, Cialic R, Baufeld C, Calcagno N, El Fatimy R, et al. The TREM2-APOE Pathway Drives the Transcriptional Phenotype of Dysfunctional Microglia in Neurodegenerative Diseases. Immunity. 2017; 47: 566-81.e9.
8. Meier SR, Sehlin D, Hultqvist G, Syvänen S. Pinpointing Brain TREM2 Levels in Two Mouse Models of Alzheimer's Disease. Mol Imaging Biol. 2021; 23: 665-75.
9. Blume T, Focke C, Peters F, Deussing M, Albert NL, Lindner S, et al. Microglial response to increasing amyloid load saturates with aging: a longitudinal dual tracer in vivo μPET-study. J Neuroinflammation. 2018; 15: 307.
10. Butovsky O, Weiner HL. Microglial signatures and their role in health and disease. Nat Rev Neurosci. 2018; 19: 622-35.
11. Keren-Shaul H, Spinrad A, Weiner A, Matcovitch-Natan O, Dvir-Szternfeld R, Ulland TK, et al. A Unique Microglia Type Associated with Restricting Development of Alzheimer's Disease. Cell. 2017; 169: 1276-90.e17.
12. Schlepckow K, Monroe KM, Kleinberger G, Cantuti-Castelvetri L, Parhizkar S, Xia D, et al. Enhancing protective microglial activities with a dual function TREM2 antibody to the stalk region. EMBO Mol Med. 2020; 12: e11227.
13. Chiu IM, Morimoto ET, Goodarzi H, Liao JT, O'Keeffe S, Phatnani HP, et al. A neurodegeneration-specific gene-expression signature of acutely isolated microglia from an amyotrophic lateral sclerosis mouse model. Cell Rep. 2013; 4: 385-401.
14. Kulkarni B, Kumar D, Cruz-Martins N, Sellamuthu S. Role of TREM2 in Alzheimer's Disease: A Long Road Ahead. Mol Neurobiol. 2021; 58: 5239-52.
15. Calsolaro V, Edison P. Neuroinflammation in Alzheimer's disease: Current evidence and future directions. Alzheimers Dement. 2016; 12: 719-32.
16. Morenas-Rodriguez E, Li Y, Nuscher B, Franzmeier N, Xiong C, Suárez-Calvet M, et al. Soluble TREM2 in CSF and its association with other biomarkers and cognition in autosomal-dominant Alzheimer's disease: a longitudinal observational study. Lancet Neurol. 2022; 21: 329-41.
17. Chauveau F, Boutin H, Van Camp N, Dollé F, Tavitian B. Nuclear imaging of neuroinflammation: a comprehensive review of [^{11}C]PK11195 challengers. Eur J Nucl Med Mol Imaging. 2008; 35: 2304-19.
18. Boutin H, Murray K, Pradillo J, Maroy R, Smigova A, Gerhard A, et al. ^{18}F-GE-180: a novel TSPO radiotracer compared to ^{11}C-R-PK11195 in a preclinical model of stroke. Eur J Nucl Med Mol Imaging. 2015; 42: 503-11.
19. Wadsworth H, Jones PA, Chau W-F, Durrant C, Fouladi N, Passmore J, et al. [^{18}F]GE-180: A novel fluorine-18 labelled PET tracer for imaging Translocator protein 18kDa (TSPO). Bioorg Med Chem Lett. 2012; 22: 1308-13.
20. Rojas C, Stathis M, Coughlin JM, Pomper M, Slusher BS. The Low-Affinity Binding of Second Generation Radiotracers Targeting TSPO is Associated with a Unique Allosteric Binding Site. J Neuroimmune Pharmacol. 2018; 13: 1-5.
21. Lee JW, Nam H, Yu SW. Systematic Analysis of Translocator Protein 18 kDa (TSPO) Ligands on Toll-like Receptors-mediated Pro-inflammatory Responses in Microglia and Astrocytes. Exp Neurobiol. 2016; 25: 262-8.
22. Suárez-Calvet M, Kleinberger G, Araque Caballero M, Brendel M, Rominger A, Alcolea D, et al. sTREM2 cerebrospinal fluid levels are a potential biomarker for microglia activity in early-stage Alzheimer's disease and associate with neuronal injury markers. EMBO Mol Med. 2016; 8: 466-76.

23. Suárez-Calvet M, Araque Caballero M, Kleinberger G, Bateman RJ, Fagan AM, Morris JC, et al. Early changes in CSF sTREM2 in dominantly inherited Alzheimer's disease occur after amyloid deposition and neuronal injury. Sci Transl Med. 2016; 8: 369ra178.
24. Parhizkar S, Arzberger T, Brendel M, Kleinberger G, Deussing M, Focke C, et al. Loss of TREM2 function increases amyloid seeding but reduces plaque-associated ApoE. Nat Neurosci. 2019; 22: 191-204.
25. Hou J, Chen Y, Grajales-Reyes G, Colonna M. TREM2 dependent and independent functions of microglia in Alzheimer's disease. Mol Neurodegener. 2022; 17: 84.
26. Ulland TK, Song WM, Huang SC-C, Ulrich JD, Sergushichev A, Beatty WL, et al. TREM2 Maintains Microglial Metabolic Fitness in Alzheimer's Disease. Cell. 2017; 170: 649-63.e13.
27. Mazaheri F, Snaidero N, Kleinberger G, Madore C, Daria A, Werner G, et al. TREM2 deficiency impairs chemotaxis and microglial responses to neuronal injury. EMBO Rep. 2017; 18: 1186-98.
28. Meyer-Luehmann M, Spires-Jones TL, Prada C, Garcia-Alloza M, de Calignon A, Rozkalne A, et al. Rapid appearance and local toxicity of amyloid-beta plaques in a mouse model of Alzheimer's disease. Nature. 2008; 451: 720-4.
29. Serrano-Pozo A, Muzikansky A, Gómez-Isla T, Growdon JH, Betensky RA, Frosch MP, et al. Differential relationships of reactive astrocytes and microglia to fibrillar amyloid deposits in Alzheimer disease. J Neuropathol Exp Neurol. 2013; 72: 462-71.
30. Guerreiro R, Wojtas A, Bras J, Carrasquillo M, Rogaeva E, Majounie E, et al. TREM2 Variants in Alzheimer's Disease. N Engl J Med. 2012; 368: 117-27.
31. Jonsson T, Stefansson H, Steinberg S, Jonsdottir I, Jonsson PV, Snaedal J, et al. Variant of TREM2 Associated with the Risk of Alzheimer's Disease. N Engl J Med. 2012; 368: 107-16.
32. Wang Y, Cella M, Mallinson K, Ulrich JD, Young KL, Robinette ML, et al. TREM2 lipid sensing sustains the microglial response in an Alzheimer's disease model. Cell. 2015; 160: 1061-71.
33. Schlepckow K, Morenas-Rodriguez E, Hong S, Haass C. Stimulation of TREM2 with agonistic antibodies-an emerging therapeutic option for Alzheimer's disease. Lancet Neurol. 2023; 22: 1048-60.
34. Shi D, Si Z, Xu Z, Cheng Y, Lin Q, Fu Z, et al. Synthesis and Evaluation of ^{68}Ga-NOTA-COG1410 Targeting to TREM2 of TAMs as a Specific PET Probe for Digestive Tumor Diagnosis. Anal Chem. 2022; 94: 3819-30.
35. Shi D, Xu Z, Cheng Y, Lin Q, Si Z, Fu W, et al. ^{124}I-Labeled Immuno-PET Targeting hTREM2 for the Diagnosis of Gastric Carcinoma. Mol Pharm. 2023; 20: 2235-44.
36. Shi D, Fu W, Tan H, Lin Q, Shi H, Cheng D. Preclinical Evaluation of ^{99m}Tc-MAG$_3$-5-Fab Targeting TREM2 in Lung Cancer Mouse Models: A Comparison with ^{99m}Tc-MAG$_3$-5-F(ab')$_2$. Mol Pharm. 2024; 21: 303-12.
37. Schlepckow K, Kleinberger G, Fukumori A, Feederle R, Lichtenthaler SF, Steiner H, et al. An Alzheimer-associated TREM2 variant occurs at the ADAM cleavage site and affects shedding and phagocytic function. EMBO Mol Med. 2017; 9: 1356-65.
38. Wunderlich P, Glebov K, Kemmerling N, Tien NT, Neumann H, Walter J. Sequential proteolytic processing of the triggering receptor expressed on myeloid cells-2 (TREM2) protein by ectodomain shedding and γ-secretase-dependent intramembranous cleavage. J Biol Chem. 2013; 288: 33027-36.
39. Kleinberger G, Yamanishi Y, Suárez-Calvet M, Czirr E, Lohmann E, Cuyvers E, et al. TREM2 mutations implicated in neurodegeneration impair cell surface transport and phagocytosis. Sci Transl Med. 2014; 6: 243ra86.
40. Thornton P, Sevalle J, Deery MJ, Fraser G, Zhou Y, Ståhl S, et al. TREM2 shedding by cleavage at the H157-S158 bond is accelerated for the Alzheimer's disease-associated H157Y variant. EMBO Mol Med. 2017; 9: 1366-78.
41. van Lengerich B, Zhan L, Xia D, Chan D, Joy D, Park JI, et al. A TREM2-activating antibody with a blood–brain barrier transport vehicle enhances microglial metabolism in Alzheimer's disease models. Nat Neurosci. 2023; 26: 416-29.
42. Kariolis MS, Wells RC, Getz JA, Kwan W, Mahon CS, Tong R, et al. Brain delivery of therapeutic proteins using an Fc fragment blood-brain barrier transport vehicle in mice and monkeys. Sci Transl Med. 2020; 12: eaay1359.
43. Liu Q, Johnson EM, Lam RK, Wang Q, Bo Ye H, Wilson EN, et al. Peripheral TREM1 responses to brain and intestinal immunogens amplify stroke severity. Nat Immunol. 2019; 20: 1023-34.
44. Brady ED, Chong HS, Milenic DE, Brechbiel MW. Development of a spectroscopic assay for bifunctional ligand-protein conjugates based on copper. Nucl Med Biol. 2004; 31: 795-802.
45. Sawiak S, Wood N, Williams G, Morton A, Carpenter T. SPMMouse: a new toolbox for SPM in the animal brain. ISMRM 17th Scientific Meeting & Exhibition. 2009: 18-24.
46. Bartos LM, Kirchleitner SV, Kolabas ZI, Quach S, Beck A, Lorenz J, et al. Deciphering sources of PET signals in the tumor microenvironment of glioblastoma at cellular resolution. Sci Adv. 2023; 9: eadi8986.
47. Xiang X, Wind K, Wiedemann T, Blume T, Shi Y, Briel N, et al. Microglial activation states drive glucose uptake and FDG-PET alterations in neurodegenerative diseases. Sci Transl Med. 2021; 13: eabe5640.
48. Bader AS, Gnädig MU, Fricke M, Büschgens L, Berger LJ, Klafki HW, et al. Brain Region-Specific Differences in Amyloid-β Plaque Composition in 5XFAD Mice. Life. 2023; 13: 1053.
49. Boeddrich A, Haenig C, Neuendorf N, Blanc E, Ivanov A, Kirchner M, et al. A proteomics analysis of 5xFAD mouse brain regions reveals the lysosome-associated protein Arl8b as a candidate biomarker for Alzheimer's disease. Genome Med. 2023; 15: 50.
50. Price BR, Sudduth TL, Weekman EM, Johnson S, Hawthorne D, Woolums A, et al. Therapeutic Trem2 activation ameliorates amyloid-beta deposition and improves cognition in the 5XFAD model of amyloid deposition. J Neuroinflammation. 2020; 17: 238.
51. Oakley H, Cole SL, Logan S, Maus E, Shao P, Craft J, et al. Intraneuronal β-amyloid aggregates, neurodegeneration, and neuron loss in transgenic mice with five familial Alzheimer's disease mutations: potential factors in amyloid plaque formation. J Neurosci. 2006; 26: 10129-40.
52. Ma Y, Hof PR, Grant SC, Blackband SJ, Bennett R, Slatest L, et al. A three-dimensional digital atlas database of the adult C57BL/6J mouse brain by magnetic resonance microscopy. Neuroscience. 2005; 135: 1203-15.
53. Mirrione MM, Schiffer WK, Fowler JS, Alexoff DL, Dewey SL, Tsirka SE. A novel approach for imaging brain-behavior relationships in mice reveals unexpected metabolic patterns during seizures in the absence of tissue plasminogen activator. Neuroimage. 2007; 38: 34-42.
54. Xia D, Lianoglou S, Sandmann T, Calvert M, Suh JH, Thomsen E, et al. Novel App knock-in mouse model shows key features of amyloid pathology and reveals profound metabolic dysregulation of microglia. Mol Neurodegener. 2022; 17: 41.
55. Haass C, Kleinberger G, Schlepckow K. TREM2 cleavage modulators and uses thereof. WO2018015573A2; 2018.
56. Jay TR, von Saucken VE, Landreth GE. TREM2 in Neurodegenerative Diseases. Mol Neurodegener. 2017; 12: 56.
57. Sehlin D, Fang XT, Cato L, Antoni G, Lannfelt L, Syvänen S. Antibody-based PET imaging of amyloid beta in mouse models of Alzheimer's disease. Nat Commun. 2016; 7: 10759.
58. Syvänen S, Fang XT, Hultqvist G, Meier SR, Lannfelt L, Sehlin D. A bispecific Tribody PET radioligand for visualization of amyloid-beta protofibrils - a new concept for neuroimaging. Neuroimage. 2017; 148: 55-63.
59. Frank S, Burbach GJ, Bonin M, Walter M, Streit W, Bechmann I, et al. TREM2 is upregulated in amyloid plaque-associated microglia in aged APP23 transgenic mice. Glia. 2008; 56: 1438-47.
60. Filipello F, You S-F, Mirfakhar FS, Mahali S, Bollman B, Acquarone M, et al. Defects in lysosomal function and lipid metabolism in human microglia harboring a TREM2 loss of function mutation. Acta Neuropathol. 2023; 145: 749-72.
61. Paloneva J, Manninen T, Christman G, Hovanes K, Mandelin J, Adolfsson R, et al. Mutations in two genes encoding different subunits of a receptor signaling complex result in an identical disease phenotype. Am J Hum Genet. 2002; 71: 656-62.
62. Berdowski WM, Sanderson LE, van Ham TJ. The multicellular interplay of microglia in health and disease: lessons from leukodystrophy. Dis Model Mech. 2021; 14: dmm048925.
63. Thakkar RN, Patel D, Kioutchoukova IP, Al-Bahou R, Reddy P, Foster DT, et al. Leukodystrophy Imaging: Insights for Diagnostic Dilemmas. Med Sci. 2024; 12: 7.
64. Potter GB, Petryniak MA. Neuroimmune mechanisms in Krabbe's disease. J Neurosci Res. 2016; 94: 1341-8.
65. Marteyn A, Baron-Van Evercooren A. Is involvement of inflammation underestimated in Pelizaeus-Merzbacher disease? J Neurosci Res. 2016; 94: 1572-8.
66. Salsano E, Marotta G, Manfredi V, Giovagnoli AR, Farina L, Savoiardo M, et al. Brain fluorodeoxyglucose PET in adrenoleukodystrophy. Neurology. 2014; 83: 981-9.
67. Benzoni C, Moscatelli M, Farina L, Magri S, Ciano C, Scaioli V, et al. Adult-onset leukodystrophy with vanishing white matter: a case series of 19 patients. J Neurol. 2023; 270: 4219-34.
68. Finnsson J, Lubberink M, Savitcheva I, Fällmar D, Melberg A, Kumlien E, et al. Glucose metabolism in the brain in LMNB1-related autosomal dominant leukodystrophy. Acta Neurol Scand. 2019; 139: 135-42.
69. Donat CK, Scott G, Gentleman SM, Sastre M. Microglial Activation in Traumatic Brain Injury. Front Aging Neurosci. 2017; 9: 208.
70. Alberts A, Lucke-Wold B. Updates on Improving Imaging Modalities for Traumatic Brain Injury. J Integr Neurosci. 2023; 22: 142.

71. Filipello F, Goldsbury C, You SF, Locca A, Karch CM, Piccio L. Soluble TREM2: Innocent bystander or active player in neurological diseases? Neurobiol Dis. 2022; 165: 105630.
72. Bartos LM, Kunte ST, Beumers P, Xiang X, Wind K, Ziegler S, et al. Single-Cell Radiotracer Allocation via Immunomagnetic Sorting to Disentangle PET Signals at Cellular Resolution. J Nucl Med. 2022; 63: 1459-62.

Supplement to:

PET imaging of microglia in Alzheimer's disease using copper-64 labeled TREM2 antibodies

Monireh Shojaei[1*], Rebecca Schaefer[1*], Kai Schlepckow[2], Lea H. Kunze[1], Felix L. Struebing[2,3], Bettina Brunner[2], Michael Willem[2], Laura M. Bartos[1], Astrid Feiten[2,4], Giovanna Palumbo[1], Thomas Arzberger[3,5], Peter Bartenstein[1,6], Gian Carlo Parico[7], Dan Xia[7], Kathryn M. Monroe[7], Christian Haass[2,4,6], Matthias Brendel[1,2,6*], Simon Lindner[1*]

[1] Department of Nuclear Medicine, University Hospital, LMU Munich, Munich, Germany

[2] German Center for Neurodegenerative Diseases (DZNE), Munich, Germany

[3] Center for Neuropathology and Prion Research, University Hospital, LMU Munich, Munich, Germany

[4] Metabolic Biochemistry, Biomedical Center (BMC), Faculty of Medicine, LMU Munich, Munich, Germany

[5] Department of Psychiatry and Psychotherapy, University Hospital, LMU Munich, Munich, Germany

[6] Munich Cluster of Systems Neurology (SyNergy), Munich, Germany

[7] Denali Therapeutics Inc, South San Francisco, CA, USA

*contributed equally

SUPPLEMENTAL METHODS

CHEMICALS

Chemicals were obtained from the following companies: CheMatech, Thermo Fischer Scientific macrocycle design technologies, Merck, Sigma Aldrich, VWR, and Advanced Biochemical Compounds (ABX). All chemicals were utilized directly without any further purification. [^{64}Cu]$CuCl_2$ was received from the Department of Preclinical Imaging and Radiopharmacy, University Hospital Tuebingen, Germany. 14D3 [1], 4D9 (Schlepckow *et al,* 2020 [2]), and ATV:4D9 antibody (Van Lengerich *et al*, 2023 [3]) were provided by DENALI Therapeutics, South San Francisco, United States, and German Center for Neurodegenerative Diseases (DZNE Munich).

p-SYK ASSAY

Quantification of p-SYK levels in HEK293 cells stably overexpressing TREM2 and DAP12 upon stimulation with either 4D9 or ATV:4D9 was determined using the AlphaLISA technology. The experiment was performed as described previously by Schlepckow *et al*. 2020 [2].

IN VITRO STABILITY

[^{64}Cu]Cu-NODAGA-ATV:4D9 was incubated in murine plasma for 48 h. After neck dislocation of the mouse, the blood was collected by cardiac puncture and transferred into an Eppendorf tube. The blood samples were centrifuged for 10 minutes at 2000 rpm (Mini spin centrifuge, Eppendorf), and blood cells were separated from the plasma, which was subsequently kept at -20 °C. The tracer (172.5 MBq) was incubated in 100 µL of murine plasma with gentle shaking (400 rpm) at 37 °C for 48 h. After 30 min, 180 min, 270 min, 19 h, 42 h and 48 h, 10 µL of the mixture was taken and injected into HPLC (Agilent Technologies, 1200 series, Phenomenex column, BioSep ™ 5 µm SEC-s 4000 500 Å LC Column 300 x 7.8 mm, with 0.1 M sodium phosphate buffer, pH 7.2, isocratic run, 1 mL/min, 20 min).

SDS-PAGE

Antibody integrity was assessed by SDS-PAGE under non-reducing conditions for unmodified antibodies 4D9 and ATV:4D9, modified antibodies NODAGA-4D9 and NODAGA-ATV:4D9, and labeled antibodies [^{64}Cu]Cu-NODAGA-4D9 and [^{64}Cu]Cu-NODAGA-ATV:4D9. Antibodies (2 µg in PBS) were incubated with SDS sample buffer (bio-rad, #1610747), loaded onto an 8% Bolt Bis-Tris Plus gel and run with MOPS buffer at 200 V for 35 min. Seeblue™ Plus2 Protein Ladder (Thermo Fisher Scientific) was used as a standard. Proteins were stained using Coomassie staining (SimplyBlue Safestain, Thermo Fisher Scientific) for one hour. The radioactive gels were exposed to a phosphor imaging plate for 30 minutes. The plates were scanned with a CR-Reader (CR35 BIO, Dürr Medical), and analyzed using Aida Image Analyzer software.

Analysis of antibody integrity and functionality of the NODAGA modification was performed *ex vivo* using plasma samples from mice 20 h p.i. treated with [^{64}Cu]Cu-NODAGA-4D9 (39.8 MBq, WT, n = 1, male) or [^{64}Cu]Cu-NODAGA-ATV:4D9 (42.3 MBq, WT;TfR$^{mu/hu}$, n = 1, male). Cardiac blood was collected in EDTA tubes (Sarstedt Microvette 100 K3E), centrifuged (3000 × g, 10 min) and the plasma was separated. Radioactivity measurements using a gamma counter were used to quantify tracer concentrations in the plasma. SDS-PAGE and autoradiography were conducted as previously described, except that 0.2 µg of antibody was loaded per well.

TRACER BENCHMARKING

%ID/g and SUVR values from PET studies utilizing a range of TSPO tracers were compiled. Ratios were calculated by comparing TSPO-rich tissues with reference tissues, and compared to ratios derived from [^{64}Cu]Cu-NODAGA-4D9 PET data of 5xFAD;TfR$^{mu/hu}$ and WT;TfR$^{mu/hu}$ 20 h p.i. in the frontal cortex.

IMMUNOHISTOCHEMISTRY

AD brain tissue was taken from an 83-year-old female patient with following characteristics: AD Braak stage VI, Aβ phase 5 according to Thal, cerebral amyloid angiopathy (especially in leptomeninx, occasionally in neocortex) stage 2 according to Thal, CERAD C + Lewy Body Disease (amygdala predominantly) + TDP43 stage 2 according to Josephs. The TREM2 genotype was unknown.

Immunohistochemistry was performed on paraffin sections using a Ventana BenchMark ULTRA (Roche). Primary antibodies were (a) mouse anti-beta-amyloid (17-24) (clone 4G8; diluted 1:5,000; Biolegend SIG-39220) and (b) mouse anti-hyperphosphorylated microtubule-associated protein tau (MAPT) (clone AT-8; diluted 1:400; ThermoFisher #MN1020). Pretreatment for antibody (a) was 80% formic acid for 15 min and antibody (b) boiling in CC1 buffer for 36 min. Diaminobenzidine/peroxidase-based detection system was UltraView. Stains were scanned with a Zeiss Axio Scan.Z1.

AUTORADIOGRAPHY OF HUMAN BRAIN SECTION

In vitro autoradiography of the human brain section was conducted as described for 5xFAD;TfR$^{mu/hu}$ and WT;TfR$^{mu/hu}$ mice (Methods, main manuscript).

SUPPLEMENTAL FIGURES

FIGURE S1 - ARSENAZO SPECTROPHOTOMETRIC ASSAY

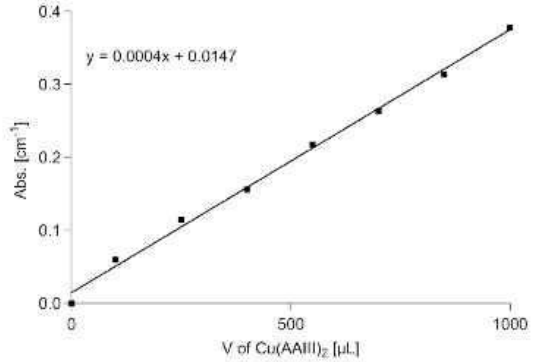

Validation of Lambert Beer's law. The absorbance of different concentrations of $Cu(AAIII)_2$ in 0.15 M NH_4OAc, pH 7.0 was measured at 652 nm in a 1.0 mL quartz cuvette using a UV-Vis spectrophotometer. Linear regression, $R^2 = 0.9957$. Modified from [4].

FIGURE S2 - QUALITY CONTROL OF [^{64}Cu]Cu-NODAGA-ATV:4D9 AND [^{64}Cu]Cu-NODAGA-4D9

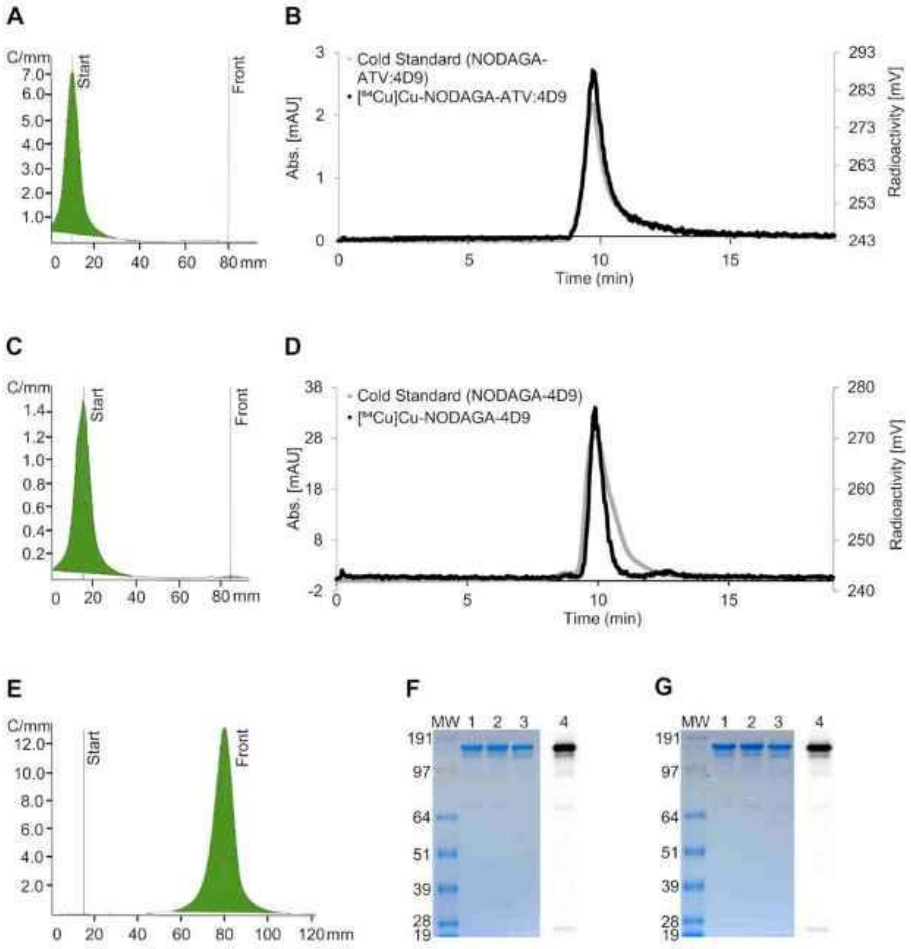

(A) Radio-TLC of [^{64}Cu]Cu-NODAGA-ATV:4D9 on ITLC-SG chromatography paper; R_f = 0.0. (B) HPLC chromatogram of [^{64}Cu]Cu-NODAGA-ATV:4D9; NODAGA-ATV:4D9 (R_t = 10.1 min, UV channel); [^{64}Cu]Cu-NODAGA-ATV:4D9 (R_t = 10.1 min, radio channel). (C) Radio-TLC of [^{64}Cu]Cu-NODAGA-4D9 on ITLC-SG chromatography paper; R_f = 0.0. (D) HPLC chromatogram of [^{64}Cu]Cu-NODAGA-4D9; NODAGA-4D9 (R_t = 10.3 min, UV channel); [^{64}Cu]Cu-NODAGA-4D9 (R_t = 10.3 min, radio channel). (E) Radio-TLC of [^{64}Cu]$CuCl_2$ on ITLC-SG chromatography paper; R_f = 1.0. (F) SDS-PAGE of ATV:4D9 (1), NODAGA-ATV:4D9 (2) and [^{64}Cu]Cu-NODAGA-ATV:4D9 (3) with autoradiography (4) of the SDS-PAGE gel. (G) SDS-PAGE of 4D9 (1), NODAGA-4D9 (2) and [^{64}Cu]Cu-NODAGA-4D9 (3) with autoradiography (4) of the SDS-PAGE gel.

FIGURE S3 - STABILITY OF [^{64}Cu]Cu-NODAGA-ATV:4D9

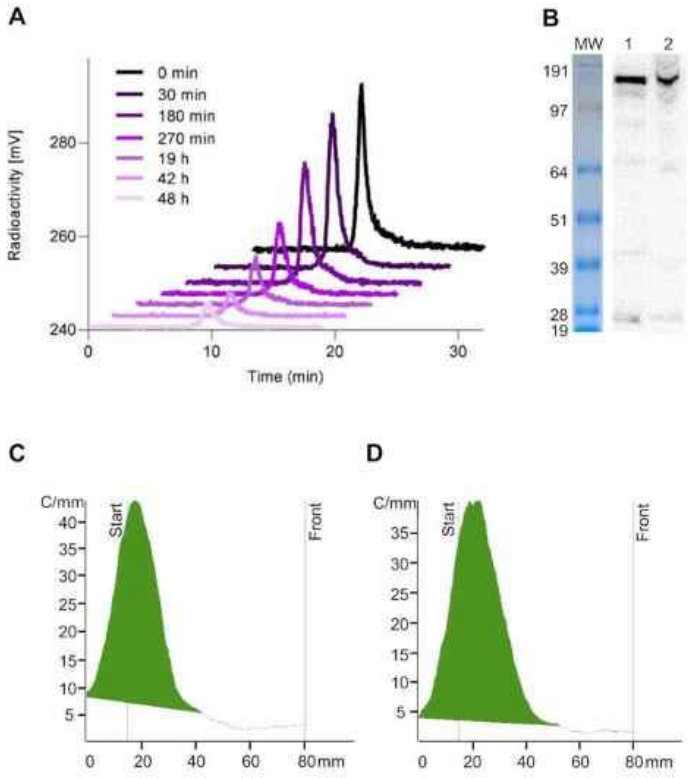

(A) *In vitro* stability of [^{64}Cu]Cu-NODAGA-ATV:4D9 in murine plasma over 48 h measured by SEC-HPLC (radioactivity channel). (B) Autoradiography of an SDS-PAGE gel loaded with plasma from a [^{64}Cu]Cu-NODAGA-4D9 (1) injected WT mouse and from a [^{64}Cu]Cu-NODAGA-ATV:4D9 (2) injected WT;TfR$^{mu/hu}$ mouse. (C) Radio-TLC of plasma from a [^{64}Cu]Cu-NODAGA-4D9 injected WT mouse on ITLC-SG chromatography paper, R_f (tracer) = 0.0-0.1. (D) Radio-TLC of plasma from a [^{64}Cu]Cu-NODAGA-ATV:4D9 injected WT;TfR$^{mu/hu}$ mouse on ITLC-SG chromatography paper, R_f (tracer) = 0.0-0.1.

FIGURE S4 - BRAIN BIODISTRIBUTION

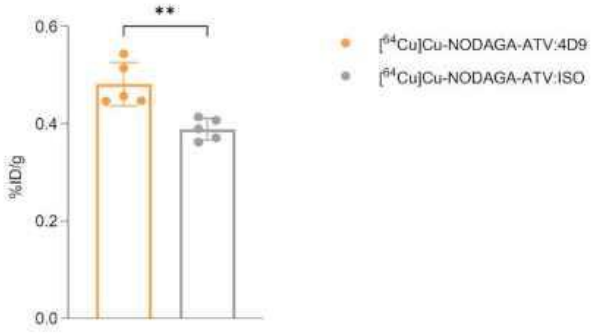

WT;TfR$^{mu/hu}$ mice were administered 14.9 ± 0.7 MBq (corresponding to 11.9 ± 0.6 µg per mouse) [^{64}Cu]Cu-NODAGA-ATV:ISO (n = 1, RCY = 85.6%, RCP = 100.0%, A_S = 1.3) in 150 µL phosphate buffer by intravenous injection through the tail vein. The relative brain uptake was determined after intracardial perfusion by biodistribution in WT;TfR$^{mu/hu}$ mice (n = 5 per group, female = 7, male = 3; 10-12 months) at 20 h p.i. Unpaired t-test, p = 0.0032 (**), mean ± SD.

FIGURE S5 - NON-DECAY-CORRECTED BRAIN BIODISTRIBUTION

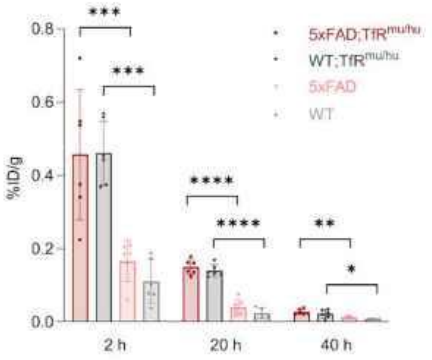

Non-decay-corrected brain uptake determined by biodistribution after intracardial perfusion in 5xFAD;TfR$^{mu/hu}$, 5xFAD, WT;TfR$^{mu/hu}$ and WT mice at 2 h, 20 h and 40 h p.i. One-way ANOVA/Tukey's multiple comparison test, $p \leq 0.05$ (*), $p \leq 0.01$ (**), $p \leq 0.001$ (***) and $p \leq 0.0001$ (****), mean ± SD.

FIGURE S6 - PET IMAGES 2 h AND 40 h p.i.

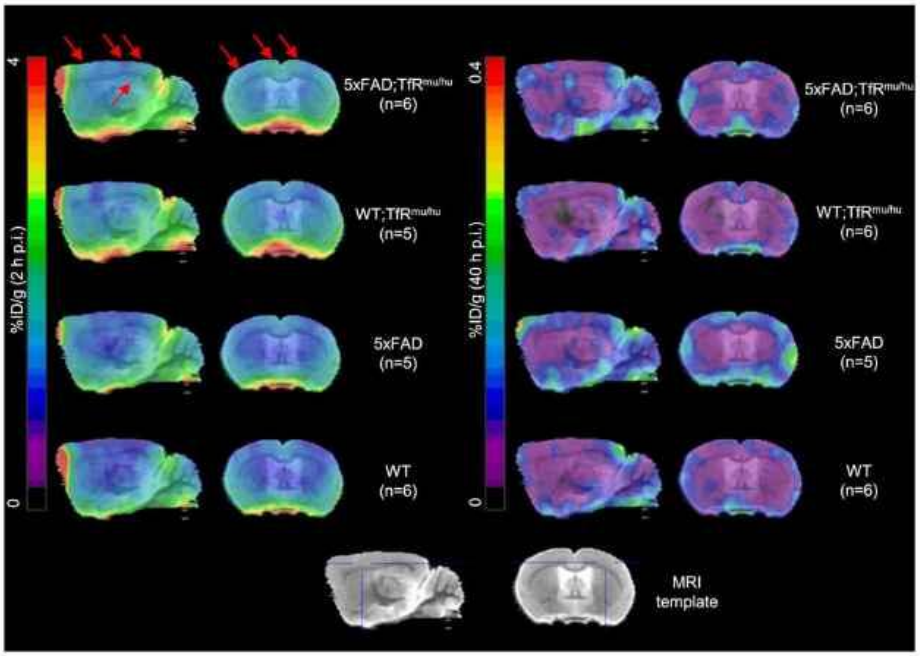

Tracer uptake in the brain of 5xFAD;TfR$^{mu/hu}$, WT;TfR$^{mu/hu}$, 5xFAD and WT mice at 2 h p.i. (left) and 40 h p.i. (right) in %ID/g.

FIGURE S7 - TREM2 PROTEIN LEVELS IN MOUSE BRAIN LYSATES

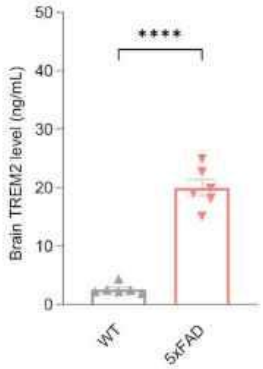

Brains were collected from 5xFAD and control animals around 6 months of age after cold PBS perfusion. Brain cortex was dissected out for homogenization using lysis buffer (Cell Signaling #9803) containing protease inhibitor cocktail (Roche #4693159001) and PhosSTOP (Roche #4906837001) as described previously [5]. After centrifugation, supernatants were transferred to new tubes for protein concentration and mouse TREM2 analysis. Mouse TREM2 levels were determined in diluted brain lysates (1:5) by an electrochemiluminescence-based assay using the Meso Scale Discovery Platform as described before [2, 5]. MSD values acquired on the MSD Sector Imager S600 reader were converted to absolute quantities of TREM2 by interpolating from a 4-parameter logistic curve fit to the mouse TREM2 standard using Graphpad Prism software and then normalized to the protein concentrations of each sample. Unpaired t-test, $p < 0.0001$ (****), mean ± SD.

FIGURE S8 - TRACER BENCHMARKING

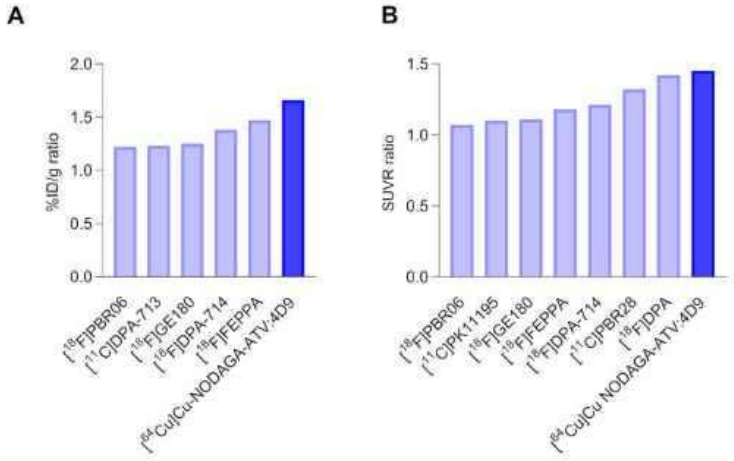

A benchmark comparison of multiple TSPO PET tracers vs [^{64}Cu]Cu-NODAGA-ATV:4D9. TSPO data derived from other PET studies (Tables S6 and S7) were used to calculate a ratio between target positive and reference tissue. Ratios are shown as (A) %ID/g and (B) SUVR.

FIGURE S9 - FLOW CYTOMETRY GATING STRATEGY

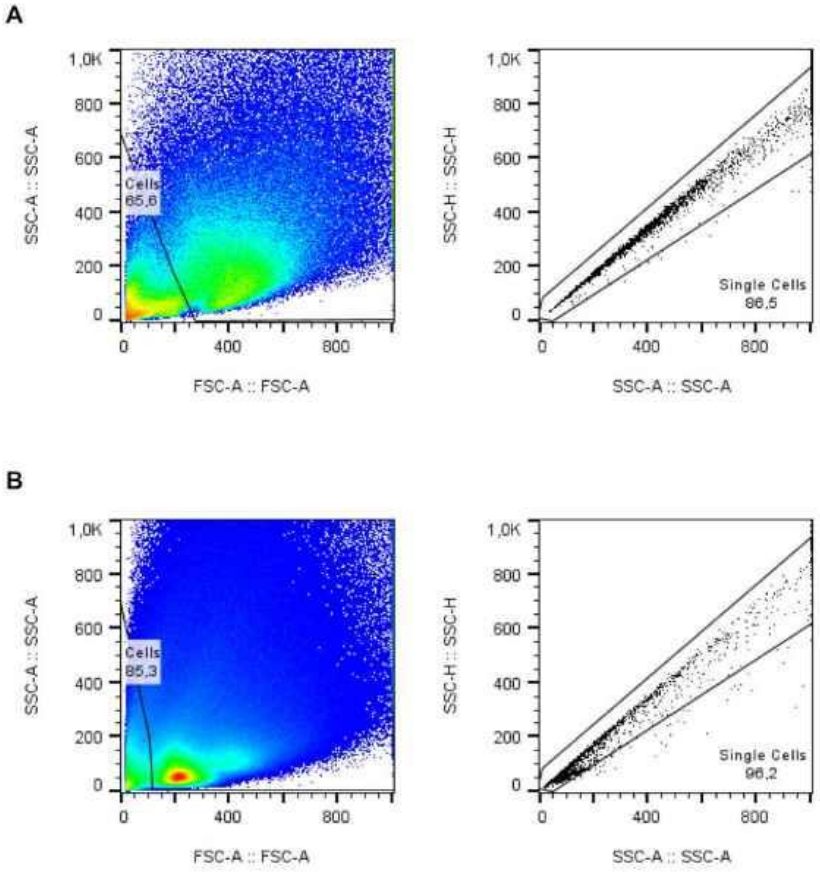

Flow cytometry gating strategy of the CD11b enriched fraction (A) and the CD11b depleted fraction (B). Left panels show pooled data from APPSAA;TfR$^{mu/hu}$ mice (n = 4) of total cells, right panels singlets considered for cell count and purity assessment.

FIGURE S10 - PET IMAGES OF $APP^{SAA};TfR^{mu/hu}$ vs $WTx;TfR^{mu/hu}$ 20 h p.i.

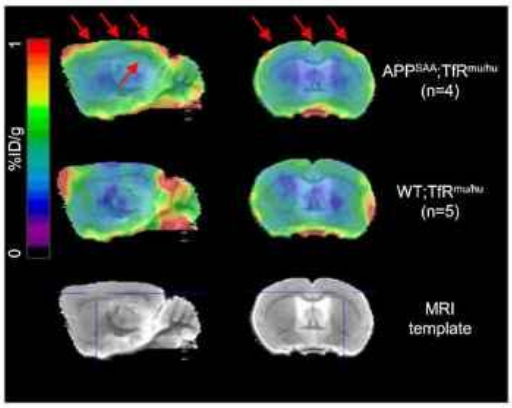

Tracer uptake in brains of $APP^{SAA};TfR^{mu/hu}$ 20 h p.i. in %ID/g. $WT;TfR^{mu/hu}$ images, derived from Fig. 3, are shown for comparison purposes.

FIGURE S11 - SPECIES SELECTIVITY OF 14D3 AND 4D9

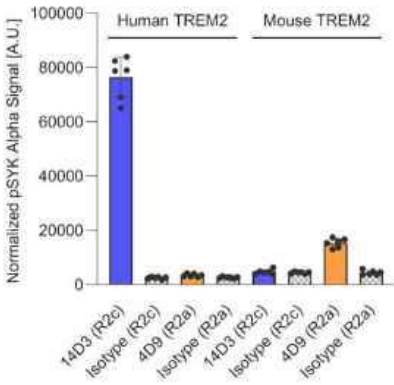

AlphaLISA mediated quantification of p-SYK levels (normalized to protein concentration) in HEK293 Flp-In cells stably overexpressing either human TREM2 and human DAP12, or mouse TREM2 and mouse DAP12 stimulated with 20 µg/µL hTREM2 14D3 (R2c), isotype control (R2c), mTREM2 4D9 (R2a) and isotype control (R2a). Data represent mean ± SD (n = 2 in triplicates).

FIGURE S12 - CO-LOCALIZATION OF IHC (Aβ AND TAU PROTEIN) AND ARG

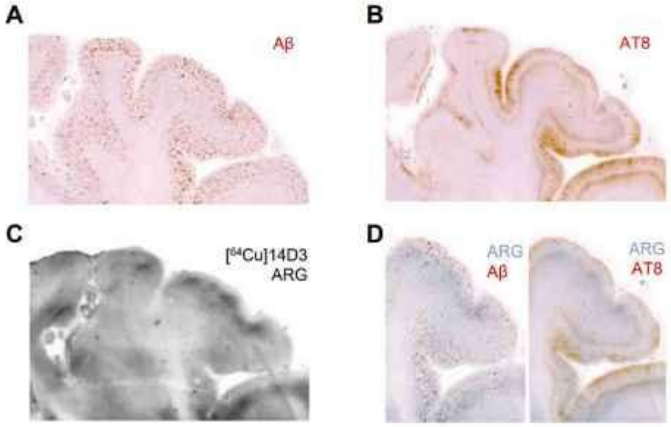

Immunohistochemistry of occipital brain sections derived from a patient with Alzheimer's disease (AD) revealed cortical binding of (A) β-amyloid and (B) pTau. (C) *In vitro* autoradiography (ARG) of [^{64}Cu]Cu-NODAGA-14D3. (D) Aβ and pTau pathology were co-localized with tracer binding.

SUPPLEMENTAL TABLES

TABLE S1 BRAIN UPTAKE FROM BIODISTRIBUTION EXPERIMENTS

Decay-corrected data:

%ID/g Mean ± SD	5xFAD;TfR$^{mu/hu}$	WT;TfR$^{mu/hu}$	5xFAD	WT	F statistics
2 h p.i.	0.57 ± 0.20	0.56 ± 0.09	0.21 ± 0.07	0.15 ± 0.07	F (3, 20) = 17.63, P<0.0001
20 h p.i.	0.52 ± 0.06	0.46 ± 0.04	0.13 ± 0.07	0.10 ± 0.05	F (3, 20) = 75.59, P<0.0001
40 h p.i.	0.30 ± 0.07	0.23 ± 0.12	0.14 ± 0.04	0.10 ± 0.03	F (3, 20) = 9.350, P=0.0005

Non-decay-corrected data:

%ID/g Mean ± SD	5xFAD;TfR$^{mu/hu}$	WT;TfR$^{mu/hu}$	5xFAD	WT	F statistics
2 h p.i.	0.46 ± 0.18	0.46 ± 0.09	0.17 ± 0.06	0.11 ± 0.06	F (3, 20) = 18.29, P<0.0001
20 h p.i.	0.15 ± 0.02	0.14 ± 0.02	0.04 ± 0.02	0.02 ± 0.01	F (3, 20) = 76.57, P<0.0001
40 h p.i.	0.03 ± 0.01	0.02 ± 0.01	0.01 ± 0.00	0.01 ± 0.00	F (3, 20) = 10.43, P=0.0002

TABLE S2 BIODISTRIBUTION DATA 40 h p.i.

%ID/g Mean ± SD	5xFAD;TfR$^{mu/hu}$	WT;TfR$^{mu/hu}$	5xFAD	WT
Brain	0.30 ± 0.07	0.23 ± 0.12	0.14 ± 0.04	0.10 ± 0.03
Heart	0.87 ± 0.15	0.81 ± 0.33	1.47 ± 0.55	1.26 ± 0.57
Kidney	1.88 ± 0.31	1.67 ± 0.75	3.03 ± 1.57	2.64 ± 1.10
Pancreas	0.61 ± 0.15	0.54 ± 0.26	0.98 ± 0.48	0.75 ± 0.35
Spleen	4.48 ± 0.91	3.28 ± 1.61	5.63 ± 3.57	3.44 ± 1.53
Muscle	0.31± 0.09	0.24 ± 0.09	0.53 ± 0.17	0.47 ± 0.16
Bone	7.99 ± 2.51	10.15 ± 8.49	8.87 ± 3.10	6.54 ± 1.62
Lung	1.48 ± 0.29	1.30 ± 0.56	1.59 ± 1.21	2.01 ± 0.99
Liver	3.56 ± 0.33	2.69 ± 1.36	3.69 ± 1.23	4.76 ± 1.92
Blood	2.02 ± 0.76	1.19 ± 0.67	5.99 ± 2.79	3.47 ± 1.66

TABLE S3 UPTAKE IN CORTEX FROM PET ANALYSIS

%ID/g Mean ± SD	5xFAD;TfR$^{mu/hu}$	WT;TfR$^{mu/hu}$	5xFAD	WT	F statistics
2 h p.i.	2.25 ± 0.10	1.68 ± 0.28	1.45 ± 0.11	1.37 ± 0.21	F (3, 18) = 26.32, P<0.0001

20 h p.i.	0.90 ± 0.18	0.55 ± 0.05	0.48 ± 0.08	0.29 ± 0.11	F (3, 18) = 26.68, P<0.0001
40 h p.i.	0.11 ± 0.02	0.06 ± 0.03	0.11 ± 0.02	0.06 ± 0.02	F (3, 19) = 6.207, P=0.0040

TABLE S4 - UPTAKE IN HIPPOCAMPUS FROM PET ANALYSIS

%ID/g Mean ± SD	**5xFAD;TfR$^{mu/hu}$**	**WT;TfR$^{mu/hu}$**	**5xFAD**	**WT**	**F statistics**
2 h p.i.	1.45 ± 0.26	1.40 ± 0.29	1.31 ± 0.12	1.19 ± 0.30	F (3, 18) = 1.140, P=0.3597
20 h p.i.	0.55 ± 0.09	0.34 ± 0.08	0.30 ± 0.07	0.18 ± 0.07	F (3, 18) = 22.17, P<0.0001
40 h p.i.	0.06 ± 0.02	0.06 ± 0.05	0.07 ± 0.02	0.06 ± 0.03	F (3, 19) = 0.2938, P=0.8294

TABLE S5 - EFFECT SIZES EXPRESSED AS COHEN'S D FROM PET ANALYSIS

Cohen´s d	**Cortex**			**Hippocampus**		
	2 h	**20 h**	**40 h**	**2 h**	**20 h**	**40 h**
5xFAD;TfR$^{mu/hu}$ vs WT;TfR$^{mu/hu}$	2.68	2.62	1.75	0.16	2.50	-0.19
5xFAD;TfR$^{mu/hu}$ vs 5xFAD	7.44	2.98	0.18	0.68	3.30	-1.03

TABLE S6 - BENCHMARK COMPARISON IN %ID/g

Tracer	**Host**	**Overview pos vs ref**	**Region**	**%ID/g pos/ref/ratio**	**Ref**
[^{18}F]PBR06	mouse	APP$^{L/S}$ vs WT	CTX	4.07/3.33/1.22	[6]
[^{11}C]DPA-713	mouse	Neuroinflammation in ischemic stroke model (ipsilateral vs contralateral)	CTX	3.11/2.53/1.23	[7]
[^{18}F]GE180	mouse	Neuroinflammation in ischemic stroke model (ipsilateral vs contralateral)	CTX	4.26/3.42/1.25	[7]
[^{18}F]DPA-714	mouse	3xTg-AD vs WT	whole brain	1.35/0.98/1.38	[8]
[^{18}F]FEPPA	mouse	WT; Neuroinflammation induced by LPS vs saline	CTX	1.35/0.98/1.38	[9]
[^{64}Cu]Cu-NODAGA-ATV:4D9	mouse	5xFAD;TfR$^{mu/hu}$ vs WT;TfR$^{mu/hu}$	CTX	0.90/0.55/1.64	

TABLE S7 - BENCHMARK COMPARISON IN SUVR

Tracer	Host	Overview pos vs ref	Region	SUVR ref region	SUVR pos/ref/ratio	Ref
[^{18}F]PBR06	human	PD vs healthy	putamen	global brain	1.07/1.00/1.07	[10]
[^{18}F]PBR06	human	AD vs healthy	hippocampus	cerebellar cortex	1.07/0.97/1.10	[11]
[^{18}F]GE180	mouse	PS2APP vs WT	forebrain	white matter	0.71/0.64/1.11	[12]
[^{18}F]FEPPA	rat	Neuroinflammation induced by exposition to fine particulate matter (PM2.5) vs sterile filter	retrosplenial cortex	cerebellum	0.98/0.83/1.18	[13]
[^{18}F]DPA-714	mouse	APP/PS1-21 vs WT	CTX	cerebellum	0.88/0.73/1.21	[14]
[^{11}C]PBR28	mouse	APP/PS1-21 vs WT	CTX	cerebellum	0.96/0.73/1.32	[14]
[^{18}F]DPA	mouse	APP/PS1-21 vs WT	CTX	cerebellum	1.05/0.74/1.42	[14]
[^{64}Cu]Cu-NODAGA-ATV:4D9	mouse	5xFAD;TfR$^{mu/hu}$ vs WT;TfR$^{mu/hu}$	CTX	cerebellum	1.53/1.06/1.45	

TABLE S8 - UPTAKE IN CORTEX FROM SPM ANALYSIS

%ID/g Mean ± SD	5xFAD;TfR$^{mu/hu}$	WT;TfR$^{mu/hu}$	5xFAD	WT	F statistics
2 h p.i.	2.26 ± 0.22	1.80 ± 0.36	1.47 ± 0.07	1.50 ± 0.26	F (3, 15) = 10.24, P=0.0006
20 h p.i.	0.77 ± 0.14	0.52 ± 0.06	0.42 ± 0.08	0.27 ± 0.11	F (3, 18) = 24.33, P<0.0001
40 h p.i.	0.09 ± 0.02	0.06 ± 0.03	0.09 ± 0.02	0.06 ± 0.02	F (3, 19) = 3.719, P=0.0294

TABLE S9 - EFFECT SIZES EXPRESSED AS COHEN'S D FROM SPM ANALYSIS

Cohen´s d	Cortex		
	2 h	20 h	40 h
5xFAD;TfR$^{mu/hu}$ vs WT;TfR$^{mu/hu}$	1.57	2.39	1.35
5xFAD;TfR$^{mu/hu}$ vs 5xFAD	4.89	3.14	-0.03

REFERENCES

1. Haass C, Kleinberger G, Schlepckow K. TREM2 cleavage modulators and uses thereof. WO2018015573A2; 2018.
2. Schlepckow K, Monroe KM, Kleinberger G, Cantuti-Castelvetri L, Parhizkar S, Xia D, et al. Enhancing protective microglial activities with a dual function TREM2 antibody to the stalk region. EMBO Mol Med. 2020; 12: e11227.
3. van Lengerich B, Zhan L, Xia D, Chan D, Joy D, Park JI, et al. A TREM2-activating antibody with a blood–brain barrier transport vehicle enhances microglial metabolism in Alzheimer's disease models. Nat Neurosci. 2023; 26: 416-29.
4. Shojaei M, Zhou Q, Palumbo G, Schaefer R, Kaskinoro J, Vehmaan-Kreula P, et al. Development and Preclinical Evaluation of a Copper-64-Labeled Antibody Targeting Glycine-Alanine Dipeptides for PET Imaging of C9orf72-Associated Amyotrophic Lateral Sclerosis/Frontotemporal Dementia. ACS Pharmacol Transl Sci. 2024; 7: 1404-14.
5. Xia D, Lianoglou S, Sandmann T, Calvert M, Suh JH, Thomsen E, et al. Novel App knock-in mouse model shows key features of amyloid pathology and reveals profound metabolic dysregulation of microglia. Mol Neurodegener. 2022; 17: 41.
6. James ML, Belichenko NP, Nguyen T-VV, Andrews LE, Ding Z, Liu H, et al. PET Imaging of Translocator Protein (18 kDa) in a Mouse Model of Alzheimer's Disease Using *N*-(2,5-Dimethoxybenzyl)-2-^{18}F-Fluoro-*N*-(2-Phenoxyphenyl)Acetamide. J Nucl Med. 2015; 56: 311-6.
7. Chaney A, Cropper HC, Johnson EM, Lechtenberg KJ, Peterson TC, Stevens MY, et al. ^{11}C-DPA-713 Versus ^{18}F-GE-180: A Preclinical Comparison of Translocator Protein 18 kDa PET Tracers to Visualize Acute and Chronic Neuroinflammation in a Mouse Model of Ischemic Stroke. J Nucl Med. 2019; 60: 122-8.
8. Liu Y, Xu Y, Li M, Pan D, Li Y, Wang Y, et al. Multi-target PET evaluation in APP/PS1/tau mouse model of Alzheimer's disease. Neurosci Lett. 2020; 728: 134938.
9. Vignal N, Cisternino S, Rizzo-Padoin N, San C, Hontonnou F, Gelé T, et al. [^{18}F]FEPPA a TSPO Radioligand: Optimized Radiosynthesis and Evaluation as a PET Radiotracer for Brain Inflammation in a Peripheral LPS-Injected Mouse Model. Molecules. 2018; 23: 1375.
10. Liu S-Y, Qiao H-W, Song T-B, Liu X-L, Yao Y-X, Zhao C-S, et al. Brain microglia activation and peripheral adaptive immunity in Parkinson's disease: a multimodal PET study. J Neuroinflammation. 2022; 19: 209.
11. Wang Q, Chen G, Schindler SE, Christensen J, McKay NS, Liu J, et al. Baseline Microglial Activation Correlates With Brain Amyloidosis and Longitudinal Cognitive Decline in Alzheimer Disease. Neurol Neuroimmunol Neuroinflamm. 2022; 9: e1152.
12. Brendel M, Kleinberger G, Probst F, Jaworska A, Overhoff F, Blume T, et al. Increase of TREM2 during Aging of an Alzheimer's Disease Mouse Model Is Paralleled by Microglial Activation and Amyloidosis. Front Aging Neurosci. 2017; 9: 1-13.
13. Cheng M-F, Cheng T-J, Guo YL, Chiu C-H, Wu H-M, Yen R-F, et al. Neuroinflammation in Low-Level PM2.5-Exposed Rats Illustrated by PET via an Improved Automated Produced [^{18}F]FEPPA: A Feasibility Study. Mol Imaging. 2022; 2022: 1076444.
14. López-Picón FR, Keller T, Bocancea D, Helin JS, Krzyczmonik A, Helin S, et al. Direct Comparison of [^{18}F]F-DPA with [^{18}F]DPA-714 and [^{11}C]PBR28 for Neuroinflammation Imaging in the same Alzheimer's Disease Model Mice and Healthy Controls. Mol Imaging Biol. 2022; 24: 157-66.

10. Acknowledgments

Supervisor

I want to express my gratitude to my supervisor, Priv.-Doz. Dr. rer. nat. Simon Lindner for his support, guidance, and encouragement throughout my PhD journey. His expertise and insights were invaluable in shaping my research and academic growth.

Colleagues and Collaborators

I extend my gratitude to Dr. Franz Josef Gildehaus and Prof. Dr. Matthias Brendel. Special thanks to all my colleagues for their camaraderie and collaborative spirit. Your support made both the challenges and successes more manageable.

Funding Organizations

I am deeply grateful to the following organizations for their generous financial support:
Deutsche Forschungsgemeinschaft (DFG, German Research Foundation)
Munich Cluster for Systems Neurology (as part of Germany's Excellence Strategy)
Koselleck Project
Horizon Europe Framework Programme (HORIZON)
Your funding and resources were crucial to the completion of this work.

Personal Thanks

I would like to thank my family for their unwavering support:
My parents and my sister
Special thanks to Iraj, Saeed, Mahdi, Milad, Ryan, Shawn, Charlotte, Mahmoud, Wolfgang, Christoph, Barbara, Ehsan, Heidemarie, Shahrzad, Rosita, Arvin and Mohsen. To all my friends, thank you for your support, love, and understanding during this demanding period.

Dedication

This work is dedicated to my parents and my sister, whose love and support have been the foundation of my academic journey.

به پایان آمد این دفتر حکایت همچنان باقیست